



저작자표시-비영리-변경금지 2.0 대한민국

이용자는 아래의 조건을 따르는 경우에 한하여 자유롭게

- 이 저작물을 복제, 배포, 전송, 전시, 공연 및 방송할 수 있습니다.

다음과 같은 조건을 따라야 합니다:



저작자표시. 귀하는 원저작자를 표시하여야 합니다.



비영리. 귀하는 이 저작물을 영리 목적으로 이용할 수 없습니다.



변경금지. 귀하는 이 저작물을 개작, 변형 또는 가공할 수 없습니다.

- 귀하는, 이 저작물의 재이용이나 배포의 경우, 이 저작물에 적용된 이용허락조건을 명확하게 나타내어야 합니다.
- 저작권자로부터 별도의 허가를 받으면 이러한 조건들은 적용되지 않습니다.

저작권법에 따른 이용자의 권리는 위의 내용에 의하여 영향을 받지 않습니다.

이것은 [이용허락규약\(Legal Code\)](#)을 이해하기 쉽게 요약한 것입니다.

[Disclaimer](#)

공학박사 학위논문

**Effect of Chain Mobility of Electrospun Polymer Nanofibers
on Molecular Diffusion and Crystallization Behavior**

전기방사를 통해 제조된 고분자 나노섬유의 분자운동성이
분자 확산 및 결정화 거동에 미치는 영향

2019년 8월

서울대학교 대학원

재료공학부

정준호

Effect of Chain Mobility of Electrospun Polymer Nanofibers
on Molecular Diffusion and Crystallization Behavior

전기방사를 통해 제조된 고분자 나노섬유의 분자운동성이
분자 확산 및 결정화 거동에 미치는 영향

지도교수 곽승엽

이 논문을 공학박사 학위논문으로 제출함
2019년 4월

서울대학교 대학원
재료공학부
정준호

정준호의 공학박사 학위논문을 인준함
2019년 7월

위원장 안철희 (인)
부위원장 곽승엽 (인)
위원 유용열 (인)
위원 김형성 (인)
위원 김주영 (인)

ABSTRACT

Polymers confined in nanoscale exhibit unusual physico-chemical properties which are not shown in bulk polymers. In this study, chain mobility of electrospun polymer nanofibers is investigated, and how the molecular mobility affects the molecular diffusion and crystallization of electrospun polymer nanofibers is discussed.

Crystal structure and molecular mobility of nylon 6 nanofibers (NFs) with different diameter and shape are investigated in chapter II. NFs with a large diameter (~370 nm) consist of metastable γ -phase. It is revealed that that crystalline phase of nylon 6 nanofibers changes into highly packed, stable α -phase when the diameter is smaller than 120 nm. In accordance with the changes in crystal structure, the melting temperature of NFs increases with decreasing diameter of NFs. In addition, the activation energy (E_a) for the molecular motion of the amorphous chains increases noticeably from 6.6 to 12.6 eV with a decrease in the diameter from 370 to 70 nm. This indicates that the molecular motion of the amorphous chains is severely suppressed with decrease in nanofiber diameter, suggesting that the amorphous chains are also closely packed, forming a rigid structure. Indeed, the change in chain morphology by confinement suppressed the release of rhodamine B from the ultrathin nanofibers. These findings provide new insights for the design and

development of advanced 1D polymer nanomaterials. Subsequently, the effect of the molecular mobility on drug release kinetics of cellulose acetate/Sulindac nanofibers (CNs) is studied. The Sulindac molecules are incorporated in cellulose acetate molecules without forming aggregated structure during electrospinning process. The CNs show amorphous chain structure. It is observed that the activation energy, E_a , for molecular motion of both the main chain and side chain tend to increase as the diameter of the CNs decreased from 850 to 350 nm. The increased E_a indicates that the chains confined in ultrathin CNs are closely packed, resulting in a low molecular mobility. With increasing E_a of the side chain motion of CNs, the drug release rate per specific surface area of CNs significantly decreased from 0.30 to 0.08 $\text{g}\cdot\text{min}^{-0.5}/\text{m}^2$. In addition, the diffusion coefficient of drug is significantly decreased from 85.3 to 20.4 nm^2/min with decreasing diameter from 620 to 350 nm. These results indicate that the confinement-induced suppression of the molecular motion could significantly affect the drug release properties of polymer nanofibers.

The effect of chain mobility on crystallization of polymer nanofibers is discussed. *Meta*-aramid exhibits excellent chemical stability and mechanical strength owing to its rigid crystal structure. However, the crystal structure is destroyed when *meta*-aramid nanofibers (*m*ANFs) are fabricated by electrospinning, which results in nanofibers with poor performance

characteristics. In chapter IV, effect of chain mobility on the solvent-assisted crystallization of *m*ANFs is studied. The optimal volume ratio of the co-solvent solution is determined to be 6:5:100 (DMAc:ethylene glycol:water), and the optimal crystallization temperature is 120 °C. The crystallinity of the *m*ANFs obtained under these optimized conditions (*m*ANF-6-120) is higher than the crystallinity of *m*ANFs heat-treated at 300 °C (*m*ANF-HT). As a result, *m*ANF-6-120 exhibits superior chemical stability and mechanical strength compared to *m*ANF-HT. After immersion in DMAc for 48 hours, the weight of *m*ANF-6-120 is reduced to 28% of its original weight, whereas the relative remaining weight of *m*ANF-HT is less than 8%. The XRD peak intensity of *m*ANFs crystallized at optimum condition decreases as diameter of *m*ANFs decreases, indicating that the suppression of the molecular motion of the amorphous chains results in low degree of crystallization. The crystallization process developed in this study requires less energy and is less expensive than the conventional high-temperature heat treatment process. Subsequently, effect of chain mobility on the vapor-induced crystallization of *m*ANFs is discussed. The optimum vapor-induced crystallization process is investigated by adjusting the composition of co-solvent (aniline/DMAc) and crystallization temperature. The optimal volume ratio of the co-solvent solution is determined to be 1:2.6 (aniline:DMAc), and the optimal crystallization temperature is 120 °C. The degree of crystallization of *m*ANFs crystallized at optimum condition decreases with decrease in diameters. As a

result, chemical stability for DMAc of *m*ANFs crystallized at optimum condition decreases with decreasing their diameter. The relative weight of *m*ANFs having average diameter of 160, 110 and 90 nm after immersing in DMAc for 48 h is 79, 62 and 32%, respectively. The results shown in this study indicate that changes in chain mobility could be closely related to the practical application of electrospun polymer nanofibers for various industrial fields.

Keywords: Cellulose acetate, chain packing, chain mobility, crystallization, crystal structure, drug release, *meta*-Aramid, molecular diffusion, nanofibers, nylon 6, size effect

Student Number: 2012-30219

CONTENTS

ABSTRACTi

CONTENTS.....v

LIST OF TABLESx

LIST OF FIGURESxi

CHAPTER I

INTRODUCTION1

I-1. Molecular mobility of polymer nanomaterials 1

I-1-1. Thinfilm 1

I-1-2. Nanoparticle 4

I-1-3. Nanofiber 5

I-2. Electrospun polymer nanofibers 8

I-2-1. Electrospinning process 8

I-2-2. Application of electrospun polymer nanofibers 12

I-3. Spin-lattice relaxation time measurement 14

I-4. Research Objectives.....	18
References and Notes	22

CHAPTER II

Investigation on Crystal Structure and Molecular Mobility of Nylon 6 Nanofibers.....	30
II-1. Introduction	30
II-2. Experimental Section.....	33
II-2-1. Materials.....	33
II-2-2. Fabrication of nylon 6 nanofibers.....	33
II-2-3. Fabrication of rhB-loaded Nanofibers	34
II-2-4. Characterization.....	35
II-3. Results and Discussion.....	38
II-3-1. Crystal structure of nylon 6 nanofibers.....	38
II-3-2. Molecular mobility of nylon 6 nanofibers.....	54
II-3-3. Molecular diffusion in nylon 6 nanofibers	64
II-4. Conclusion.....	67
References and Notes	69

CHAPTER III

Effect of Molecular Mobility on Drug Release Properties of Cellulose Acetate/Sulindac Nanofibers	73
III-1. Introduction	73
III-2. Experimental Section	76
III-2-1. Materials.....	76
III-2-2. Preparation of CA/Sulindac nanofibers	76
III-2-3. Characterization.....	77
III-2-4. Release of Sulindac from CA/Sulidac nanofibers	79
II-3. Results and Discussion.....	81
III-3-1. Characteristics of CA/Sulindac nanofibers	81
III-3-2. Molecular mobility of CA/Sulindac nanofibers	89
III-3-3. Drug release properties of CA/Sulindac nanofibers	97
III-4. Conclusion.....	106
References and Notes	108

CHAPTER IV

Solvent-Assisted Crystallization of <i>meta</i>-Aramid Nanofibers	115
IV-1. Introduction	115
IV-2. Experimental Section	119
IV-2-1. Materials.....	119
IV-2-2. Fabrication of <i>meta</i> -aramid nanofibers	119
IV-2-3. Crystallization of <i>meta</i> -aramid nanofibers	120
IV-2-4. Characterization of <i>meta</i> -aramid nanofibers	121
IV-3. Results and Discussion.....	123
IV-3-1. Morphology and crystal structure of <i>meta</i> -aramid nanofibers.....	123
IV-3-2. Effect of size on degree of crystallization of <i>meta</i> -aramid nanofibers.....	136
IV-3-1. Thermal properties and chemical stability of <i>meta</i> -aramid nanofibers.....	139
IV-4. Conclusion.....	142
References and Notes	144

CHAPTER V

Vapor-Assisted Crystallization of <i>meta</i>-Aramid Nanofibers	150
V-1. Introduction	150
V-2. Experimental Section	153
V-2-1. Materials.....	153
V-2-2. Fabrication of <i>meta</i> -aramid nanofibers	153
V-2-3. Crystallization of <i>meta</i> -aramid nanofibers	154
V-2-4. Characterization of <i>meta</i> -aramid nanofibers	155
V-3. Results and Discussion.....	156
V-3-1. Morphology of as-spun <i>meta</i> -aramid nanofibers.....	156
V-3-2. Effect of solvent composition on crystallization	161
V-3-3. Effect of temperature on crystallization.....	167
V-3-4. Effect of size on degree of crystallization	169
V-4. Conclusion.....	177
References and Notes	179
KOREAN ABSTRACT.....	182
LIST OF PAPERS, PATENTS, AND SYMPOSIUMS.....	186

ACKNOWLEDGEMENT189

LIST OF TABLES

- Table I-1.** Main variables affecting electrospinning process
- Table I-2.** Activation energy for typical motions observed in polymer materials
- Table II-1.** Concentration and viscosity of nylon6/formic acid solution at 298 K and electrostatic field applied to the nozzle tip for each samples
- Table II-2.** T_{\min} of the nylon 6 nanofibers
- Table II-3.** Activation energy of c-NF-70 and c-NF-370 obtained from correlation time, τ_c of the first, second heating process and first heating process after the annealing process.
- Table III-1.** Surface area, drug content, and thickness of cellulose acetate/Sulindac nanofibers and bulk films
- Table III-2.** Activation energy of CNs obtained from correlation time, τ_c
- Table IV-1.** Physical properties of the meta-aramid nanofiber solutions and average fiber diameter of the as-spun meta-aramid nanofibers
- Table V-1.** Physical properties of the meta-aramid nanofiber solutions and average fiber diameter of the as-spun meta-aramid nanofibers

LIST OF FIGURES

- Figure I-1.** Mechanism for size-dependent change in T_g of free-standing polymer thinfilm and nanoparticles.
- Figure I-2.** Hypothesis for the size-dependent behaviors of polymer nanofibers.
- Figure I-3.** A general laboratory setup for an electrospinning experiment using drum-type collector.
- Figure I-4.** Applications of electrospun polymer nanofibers in various fields.
- Figure I-5.** Types of the molecular motions of polymer materials.
- Figure I-6.** Research objectives: Investigation of size-dependent behaviors of electrospun polymer nanofibers.
- Figure II-1.** FE-SEM images of (a) c-NF-70, (b) c-NF-120, (c) c-NF-220, (d) c-NF-370, (e) r-NF-800-350, and (f) r-NF-1140-270. Scale bars are 100 nm in (a), (b), (c), and (d), and 1 μ m in (e) and (f).
- Figure II-2.** FE-SEM images of (a) c-NF-70, (b) c-NF-80, (c) c-NF-100, (d) c-NF-120, (e) c-NF-200, (f) c-NF-220, (g) c-NF-270, (h) c-NF-290, (i) c-NF-370, (j) r-NF-800-350, (k) r-NF-1140-270 at low magnification and cross-section of (l) r-NF-800-350 and (m) r-NF-1140-270 at high magnification.

- Figure II-3.** WXRD patterns of (a) nylon 6 nanofibers with different diameter from 70 to 370 nm and (b) nylon 6 nanofibers with different width and thickness, (c) O 1s XPS spectra of c-NF-70, c-NF-120, c-NF-370 and r-NF-1140-350, and (d) schematic illustration of crystal structure in nylon 6 nanofibers.
- Figure II-4.** (a) Viscosity of nylon 6 solution corresponding to the resulting diameter of nylon 6 nanofibers and (b) description of the effect of solution viscosity on chain topology of nylon 6 nanofibers.
- Figure II-5.** DSC curves of (a) nylon 6 nanofibers with different diameter from 70 to 370 nm and (b) nylon 6 nanofibers with different width and thickness.
- Figure II-6.** ^1H T_1 vs the inverse temperature ($1000/T$) of nylon 6 nanofibers with different size and shape.
- Figure II-7.** (a) ^1H T_1 vs the inverse temperature ($1000/T$) and (b) logarithmic plot of the correlation time, τ_c vs the inverse temperature ($1000/T$) of NF-70 and NF-370, the activation energy of nylon 6 nanofibers obtained at the temperature (c) lower than T_{\min} and (d) higher than T_{\min} , and (e) schematic illustration of chain topology in nylon 6 nanofibers
- Figure II-8.** FE-SEM images of (a) c-NF-70 and (b) c-NF-370 after the measurement of T_1 at a temperature range from 200 to 370 K.
- Figure II-9.** (a) ^1H T_1 vs the inverse temperature ($1000/T$) and (b)

logarithmic plot of the correlation time, τ_c vs the inverse temperature ($1000/T$) of c-NF-70 and c-NF-370 during the two heating cycles

Figure II-10. (a) FE-SEM images, (b) XRD patterns and (c) DSC curves and (d) average release profiles of rhodamine B-loaded nylon6 nanofibers.

Figure III-1. FE-SEM images of (a) CN-350, (b) CN-530, (c) CN-620, (d) CN-850, and (e) BF.

Figure III-2. DSC curves of (a) CA and Sulindac and (b) CA/Sulindac nanofibers and bulk CA/Sulindac film, (c) TGA curves of CA, Sulindac, CA/Sulindac nanofibers and bulk CA/Sulindac film, and (d) XRD.

Figure III-3. (a) FT-IR spectra of CA, Sulindac, CA/Sulindac nanofibers and bulk CA/Sulindac film and (b) the enlarge IR spectra, collected over the range from 1800 to 1700 cm^{-1} , corresponding to the COOH stretch.

Figure III-4. Schematic description of ^1H spin-lattice relaxation procedure of cellulose derivatives.

Figure III-5. Logarithmic plot of the correlation time, τ_c , vs the inverse temperature ($1000/T$) of (a) CN-350, (b) CN-530, (c) CN-620 and (d) CN-850.

Figure III-6. Cumulative release profiles of Sulindac from CA/Sulindac nanofibers and bulk CA/Sulindac film by total immersion technique during (a) 0–1200 min and (b) 0–240 min, (c) 0–150

min (root time scale) and (d) drug release rate constant of CA/Sulindac nanofibers and bulk CA/Sulindac film.

- Figure III-7.** Activation energy, E_a for side chain motion and main chain motion vs drug release rate constant per specific surface area of CA/Sulindac nanofibers.
- Figure III-8.** Diffusion coefficient of CA/Sulindac nanofibers.
- Figure III-9.** Proposed effect of confinement on molecular mobility and drug release properties of CA/Sulindac nanofibers.
- Figure IV-1.** FE-SEM images of the as-spun *meta*-aramid nanofibers with different diameters.
- Figure IV-2.** WXRD patterns of meta-aramid nanofibers.
- Figure IV-3.** Schematic illustration of the crystallization mechanism of meta-Aramid nanofibers during the optimized heat-assisted heat treatment.
- Figure IV-4.** ATR FT-IR spectra of *mANF*-As, *mANF*-HT, *mANF*-0-120, *mANF*-2-120, *mANF*-4-120, *mANF*-6-120 and *mANF*-8-120. The numbers at (b) are the peak intensity ratio of the C=O \cdots H stretching band (amide I, $\sim 1647\text{ cm}^{-1}$) and the vibration of the aromatic C-C or C=C bonding ($\sim 1604\text{ cm}^{-1}$).
- Figure IV-5.** FE-SEM images of (a) *mANF*-2-120, (b) *mANF*-4-120, (c) *mANF*-6-120 and (d) *mANF*-8-120.
- Figure IV-6.** (a) FE-SEM image, (b) XRD patterns and (c) FT-IR spectra of *mANF*-6-120 with average diameters of 120, 170 and 270 nm.

- Figure IV-7.** (a) DSC curves for the first and second (insert) heating of *mANF-As*, *mANF-HT* and *mANF-6-120* and (b) TGA curves of *mANF-As*, *mANF-HT* and *mANF-6-120*.
- Figure IV-8.** Observation of the chemical stability. (a) Macroscopic image of *mANF-As*, *mANF-HT* and *mANF-6-120* soaked in DMAc, and (b) relative weight of *mANF-As*, *mANF-HT* and *mANF-6-120* at a specific immersion time.
- Figure V-1.** FE-SEM images of the as-spun *meta*-aramid nanofibers with different diameters.
- Figure V-2.** XRD patterns of *mANFs* treated with DMAc/aniline mixture at 160 °C. The composition of the mixture is 1.0, 1.4, 1.8, 2.2 and 2.6 of DMAc/aniline volume ratio.
- Figure V-3.** FE-SEM images of the as-spun *meta*-aramid nanofibers with different diameters.
- Figure V-4.** XRD patterns of *mANFs* treated with DMAc/aniline mixture at 160 °C. The composition of the mixture is 1.0, 1.4, 1.8, 2.2 and 2.6 of DMAc/aniline volume ratio.
- Figure V-5.** FE-SEM images of the as-spun *meta*-aramid nanofibers with different diameters.
- Figure V-6.** Schematic illustration of the effect of temperature on vapor-assisted crystallization of *mANFs*

- Figure V-7.** XRD patterns of *m*ANFs with different diameters (90, 100 and 160 nm). *m*ANFs were treated with DMAc/aniline (2.6:1 volume ratio) at 120 °C.
- Figure V-8.** FE-SEM images of *m*ANFs having different diameters (90, 110 and 160 nm) after the optimized vapor-assisted crystallization process.
- Figure V-9.** TGA curves of as-spun *m*ANFs with 160 nm of average diameter and *m*ANFs with 90, 110 and 160 nm of average diameter treated under optimized vapor-assisted crystallization process.
- Figure V-10.** Observation of the chemical stability: relative weight at a specific immersion time of *m*ANFs with 90, 110 and 160 nm of average diameter treated under optimized vapor-assisted crystallization process.

CHAPTER I

INTRODUCTION

I-1. Molecular mobility of polymer nanomaterials

I-1-1. Thin film

Polymer nanomaterials have attracted a great deal of attention over the past decades because of their excellent functionality and unusual physicochemical properties, which are not observed in their bulk counterparts.¹⁻⁷ Polymer nanomaterials, owing to their unique properties, have led to significant advances in various fields and devices, such as biomedical technology, flexible electronic devices, optical sensors, and methods for treating environmental pollution.⁸⁻⁹ It has been highlighted that the physical and thermal properties of polymer nanomaterials change significantly with a decrease in their dimensions. This size-dependent behavior could limit further advances in polymer nanotechnology if the phenomenon is not fully investigated. As a result, significant efforts are being made to investigate the size effect of polymer nanomaterials.

The effect of the size of nanoscopically confined polymers on their properties is typically called the “confinement effect”. The confinement effect has primarily been investigated in the case of thin films, because the thickness of such films is readily controllable and the interfacial interactions between the film surface and the substrate are tunable.¹⁰⁻¹¹ Freestanding thin films exhibit a significantly reduced glass transition temperature, T_g , as compared to that of the bulk when their thickness is decreased to less than ~ 100 nm.¹²⁻¹⁴ Torkelson et al. investigated the T_g values of the surface and internal layers of polymer thin films using fluorescence spectroscopy.¹⁵⁻¹⁷ They reported that the free surface layer of thin films had a lower T_g than that of the corresponding bulk polymer, while the internal layer of the films at a sufficient distance away from the interfaces showed a T_g similar to that of the bulk. Furthermore, studies on the molecular dynamics of thin films have revealed that the polymer chains in the free surface layer have relatively high molecular mobility, in contrast to those in the bulk counterparts.¹⁸⁻¹⁹ Hence, it has been postulated that the reduction in T_g of polymer thin films is due to the relative increase in the fraction of thin film which is part of the surface layer having high chain mobility.²⁰⁻²⁴ Meanwhile, it has been observed that T_g increases with a decrease in the thickness in the cases where strong polymer substrate interactions persist.²⁵⁻²⁶ This result indicates that the interactions between thin films and substrates is another factor determining the T_g of thin films.

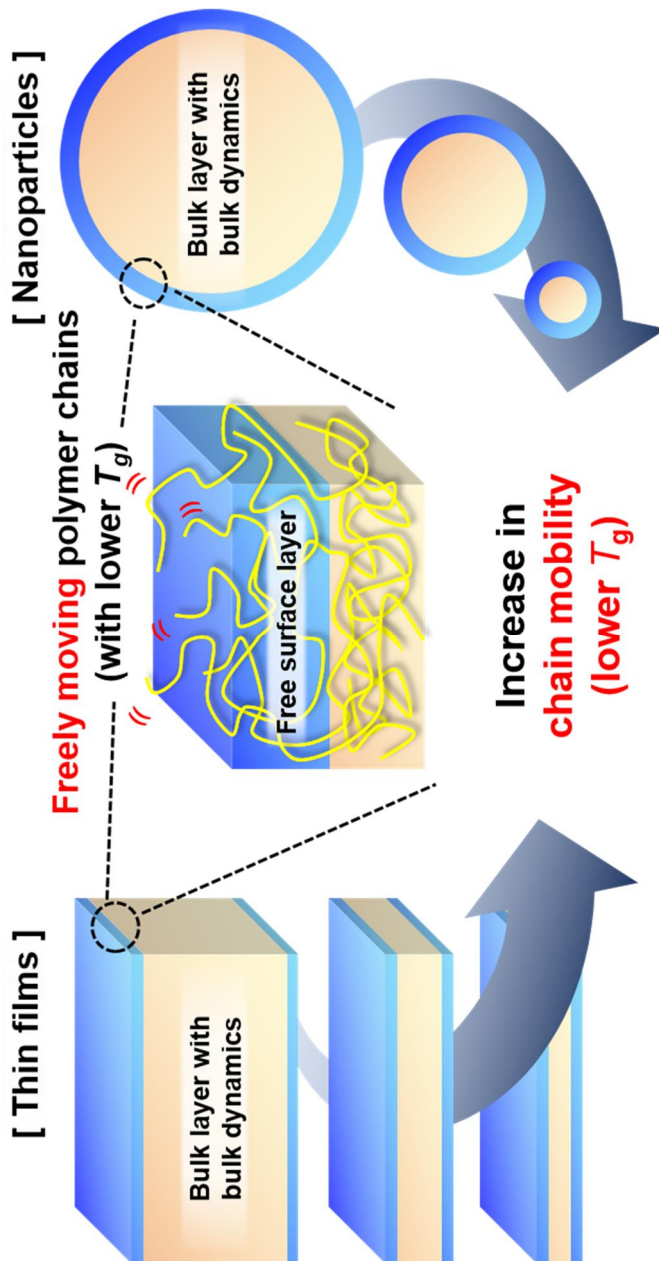


Figure I-1. Mechanism for size-dependent change in T_g of free-standing polymer thinfilm and nanoparticles

I-1-2. Nanoparticle

The discussion on the deviations in the T_g value of thin films was subsequently extended to polymer nanoparticles, which have a geometry different from that of thin films. Zhang et al. reported that polymer nanoparticles show size-dependent behavior similar to that of thin films.^{1,27-28} That is to say, the T_g of polymer nanoparticles decreased with a decrease in their diameter, owing to an increase in the fraction of a free surface layer composed of highly mobile chains. However, when the polymer nanoparticles were coated with silica, the T_g of the polymer nanoparticles did not decrease, because the free surface of the nanoparticles was removed.

There are several difficulties in analyzing the molecular mobility of polymer nanoparticles. In contrast with the thinfilm, nanoparticles easily lose their particle morphology and are agglomerated when they are exposed to heat or vapors. Theirfore, thermal analysis could not be conducted without dispersing the nanoparticles in their non-solvent. The accurate signal for nanoparticles could not be easily obtained because of the signals of the non-solvent and stabilizer used for the particle dispersion. Furthermore, the nanoparticles are not connected, thus the electrical properties such as conductivity could not be measured correctly.

I-1-3. Nanofiber

In addition to being of interest in the case of thin films and nanoparticles, the confinement effect is also attracting significant interest with respect to nanofibers because of their inherent anisotropies and potential for use in wearable devices, flexible displays, and information technology devices, among other areas.^{2, 29-30} Electrospinning is a facile technique for fabricating nanofibers (NFs) with diameters ranging from several tens of nanometers to several hundreds of nanometers.³¹⁻³³ Thus, electrospun polymer NFs are frequently used as model materials for elucidating the confinement effect. Interestingly, several researchers have reported that electrospun NFs show a sharp increase in their mechanical strength with a decrease in their diameter.³⁴⁻³⁷ This phenomenon is contradictory to the confinement effect observed in freestanding thin films, wherein T_g decreases with a decrease in size; a decrease in T_g implies enhanced molecular mobility or, in other words, lower mechanical strength. Several studies have postulated that a rigid structure is formed owing to the alignment of the chains confined with narrow NFs and that this is the reason for the distinctive confinement effect seen in electrospun NFs.^{35, 38} However, Arinstein et al. reported that the X-ray diffraction (XRD) patterns of electrospun NFs did not show a noticeable size-dependent change in their crystallinity and degree of orientation, even though their modulus increased sharply with a decrease in their diameter.^{2, 39} To

explain such result, they suggested that the chains confined in ultrathin fibers could form highly packed structures. The formation of supramolecular structures randomly directed in ultrathin fibers may not increase the degree of chain orientation. In addition, the results of small-angle neutron scattering analysis of electrospun polystyrene NFs did not indicate a change in the orientation parameter $\langle P2 \rangle$ with a change in the NF size.⁴⁰ Meanwhile, Lim et al. reported that atomic force microscopy images of polymer NFs showed that the NFs with a smaller diameter exhibited higher degrees of molecular orientation and crystallinity.⁴¹⁻⁴³ Nevertheless, the phenomenon of the degree of chain alignment of polymer NFs increasing with a decrease in their diameter is poorly understood. Hence, given that polymer NFs are of great practical use in various industrial fields, it has become necessary to investigate the molecular mobility of NFs.

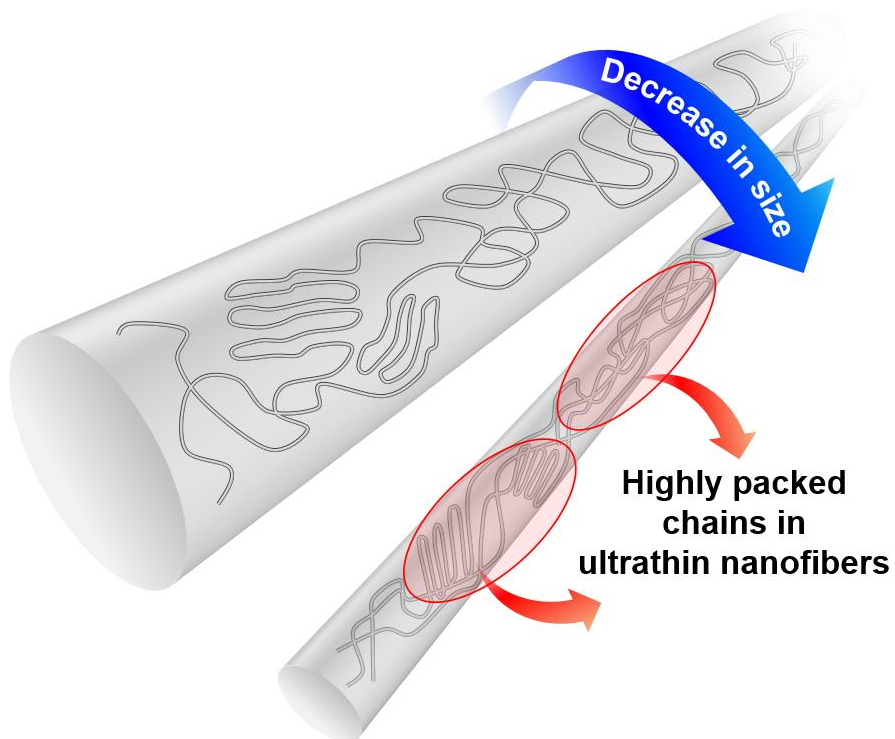


Figure I-2. Hypothesis for the size-dependent behaviors of polymer nanofibers

I-2. Electrospun polymer nanofibers

I-2-1. Electrospinning process

Among the various methods to fabricate the polymer nanofibers, electrospinning is the most popular and versatile process for creating continuous and uniform fibers having diameters ranging from a few micrometers to a few nanometers by using electrostatic repulsion of a charged droplet of polymer solution.⁴⁴⁻⁴⁶ Electrospinning process possesses characteristics of both conventional solution-dry spinning and electrospraying process.⁴⁷ In a typical electrospinning process in a laboratory, a polymer melt or solution is located in a syringe and pumped through a nozzle while being applied high voltage. Generally, high electric field of 100-500 kVm⁻¹ is applied and tip-to-collector distance is 10-25 cm in laboratory systems. When high voltage is applied to a liquid droplet, electrostatic repulsion counteracts the surface tension and the droplet is stretched. At a critical voltage, polymer solution erupts from the surface, resulting in a formation of Taylor cone. Then, a charged polymer solution jet is formed. The jet is dried during flying from nozzle to collector, elongated by a whipping process, and deposited on the collector. The two types of collector (flat electrode and rotating drum) are frequently used for lab-scale electrospinning process. Drum-type collector was used in this study.

There are three kinds of parameter groups for electrospinning: 1) materials variables, 2) processing variables, and 3) ambient variables. Materials variables such as concentration, viscosity and surface tension affect the physical properties of polymer solution. The solution viscosity dominantly affects to diameter of the polymer nanofibers while surface tension plays an important role in formation of defects such as beads and bead-like fibers. Processing variables affect the formation of Taylor cone and jet. One of the crucial parameters is applied voltage to the solution. Beads or bead-like fibers are formed when applied voltage is lower or higher than the appropriate voltage range. In addition, a higher voltage is needed to be applied as solution flow rate increases so that the Taylor cone is stable. Variables affecting electrospinning process is listed in table I-1.

Table I-1. Main variables affecting electrospinning process

Materials variables		
Chemical composition	Polymer molar mass	Polymer molar mass distribution
Solution viscosity	Surface tension	Solvent quality
Solution concentration	Charge density	Solution conductivity
Processing variables		
Electrode shape	Electrode materials	Electric field strength
Electrode-ground distance	Solution evaporation rate	Solution flow rate

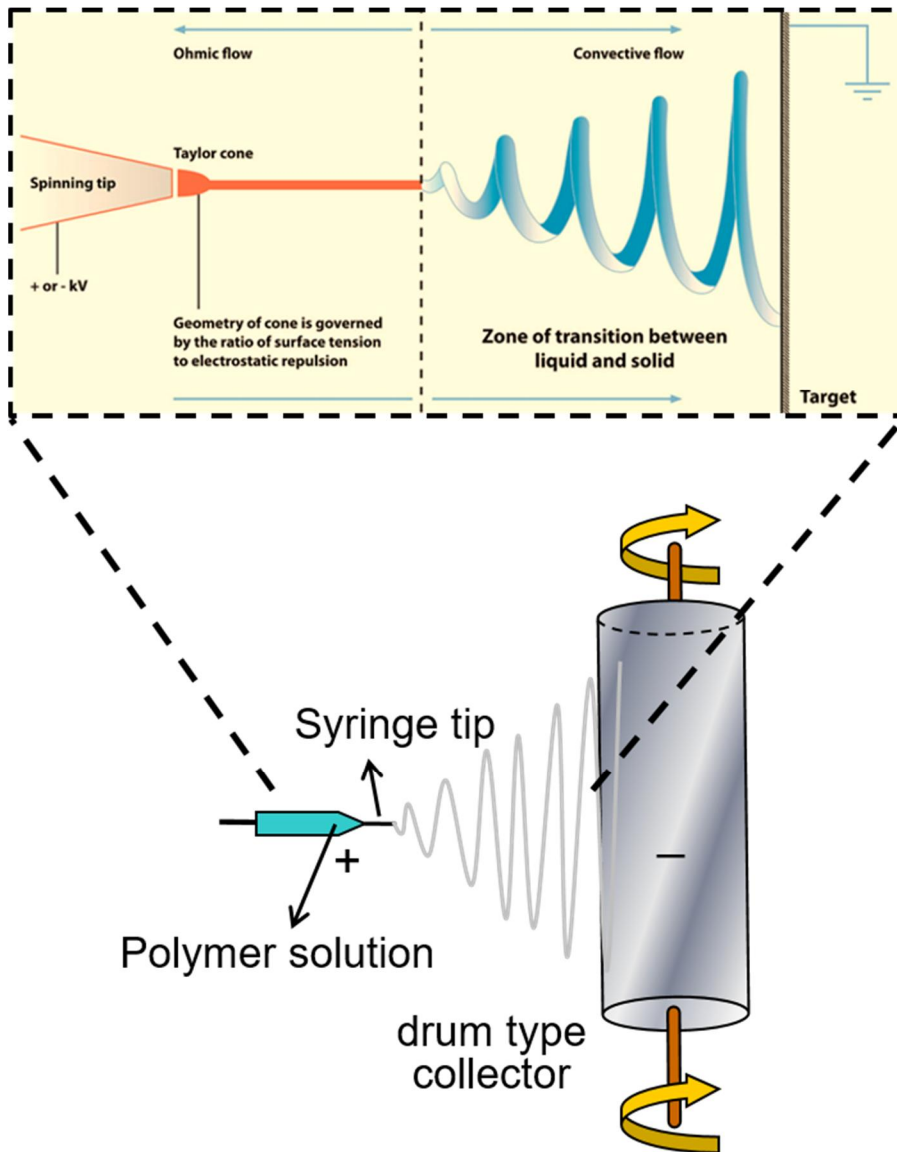


Figure I-3. A general laboratory setup for an electrospinning experiment using drum-type collector

I-2-2. Application of electrospun polymer nanofibers

Electrospun polymer nanofibers have been applied to diverse industrial fields such as life science, nano-sensing, filtration, tissue engineering due to their high specific surface area, high porosity, biocompatibility, and unique nanometer scale architecture. Among the various applications fields for polymer nanofibers, filtration market is expected to occupy the highest market share (approximately, 40%) in the global market for polymer nanofibers, followed by medicine and biotechnology. Filters based on polymer nanofibers have exhibited excellent performance in treatment of polluted water and removal of airborne particles. Polymer nanofibers made by biocompatible polymers have been used as drug delivery carrier, haemostatic devices, wound dressing and scaffolds for bone and cartilage regeneration. Metal/semiconductor nanoparticles embedded on the polymer nanofibers have been used as high-performance sensors. Polymer nanofibers containing nanocatalysts for removal of chemical warfare agent and hazardous gas have been developed. Applications of polymer nanofibers are shown in Fig. I-4.

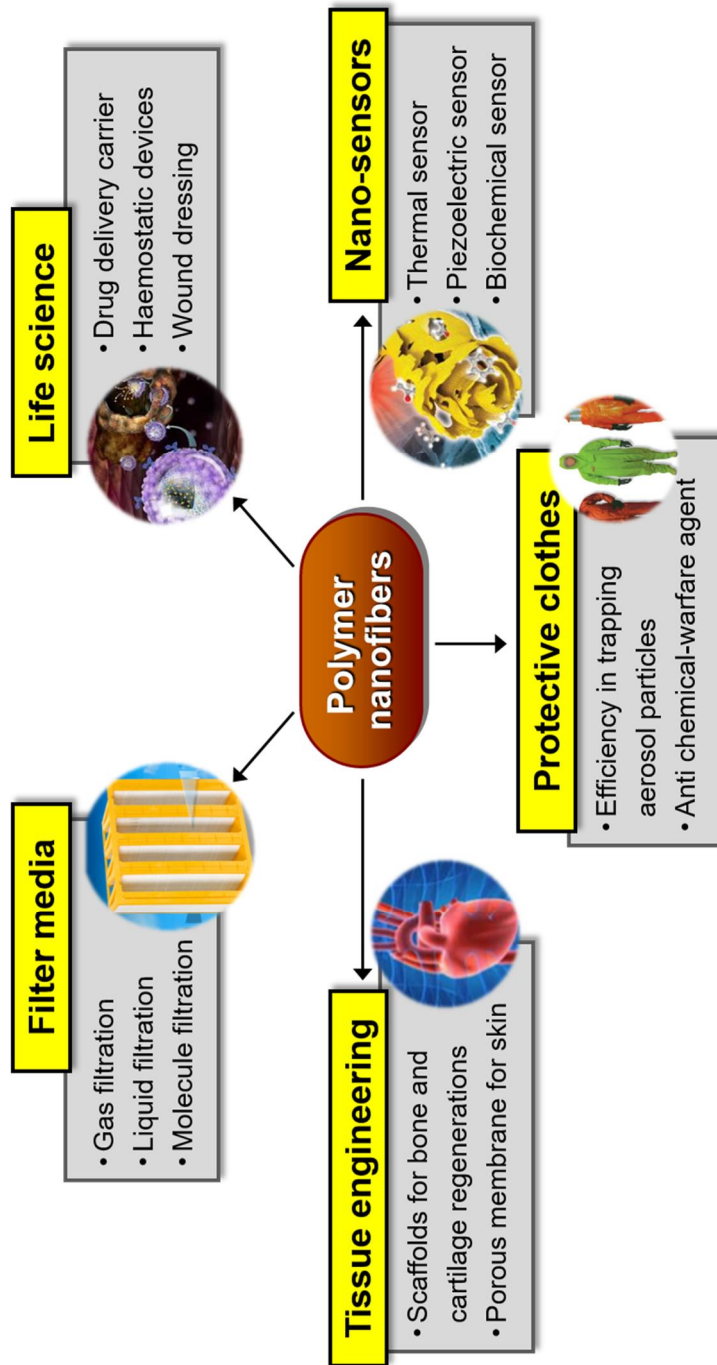


Figure I-4. Applications of electrospun polymer nanofibers in various fields

I-3. Spin-lattice relaxation time measurement

Molecular mobility is one of the key factors determining the thermal, mechanical and physical properties of bulk polymers. Therefore, numerous studies on the polymer dynamic behaviors have been reported to achieve desired material performance (such as strength, dimensional stability, permeability to gases and water, and so on).⁴⁷⁻⁵⁰ However, most of the common methods which are applied to analysis the chain dynamics of bulk polymer or polymer solution system could not be applied to study on size-dependent behaviors of polymer nanofibers. For instance, techniques that applying periodic mechanical force to materials such as dynamic mechanical analysis or rheological measurement are not appropriate to observe chain dynamics of polymer nanofibers because mechanical force cannot be uniformly delivered to nanofibrous mat. In the same manner, dielectric relaxation spectroscopy is not suitable because the dielectrical signals cannot be uniformly applied to polymer nanofibers. In contrast, spin-lattice relaxation time measurement enables to analysis the chain dynamics of polymer nanofibers because magnetic field could be uniformly applied to polymer nanofibers. In this study, spin-lattice relaxation time was measured by using ¹H solid-state nuclear magnetic resonance (NMR) spectroscopy to identify the chain dynamics of polymer nanofibers.

Nuclear spin state of hydrogen atom is divided into two states when magnetic field is applied. The energy difference of the two states is proportional to the intensity of magnetic field applied to samples. When pulse corresponding to the energy difference is applied, the nuclei at the lower energy level state are excited to the higher energy level state. When the pulse is removed after the spin excitation, the excited spins go through spin-lattice relaxation. Definition for lattice is that rest of the assembly of samples from spin (other types of nuclei, atoms, molecules, *etc.*). In the case of polymer materials, the molecular motion of chains is responsible for the spin-lattice relaxation. Therefore, measurement of the time required for the spin-lattice relaxation enables to analyze the chain dynamics of the polymer materials. The types of the molecular motions and activation energy for the motions are described in Fig. I-5 and table I-2.

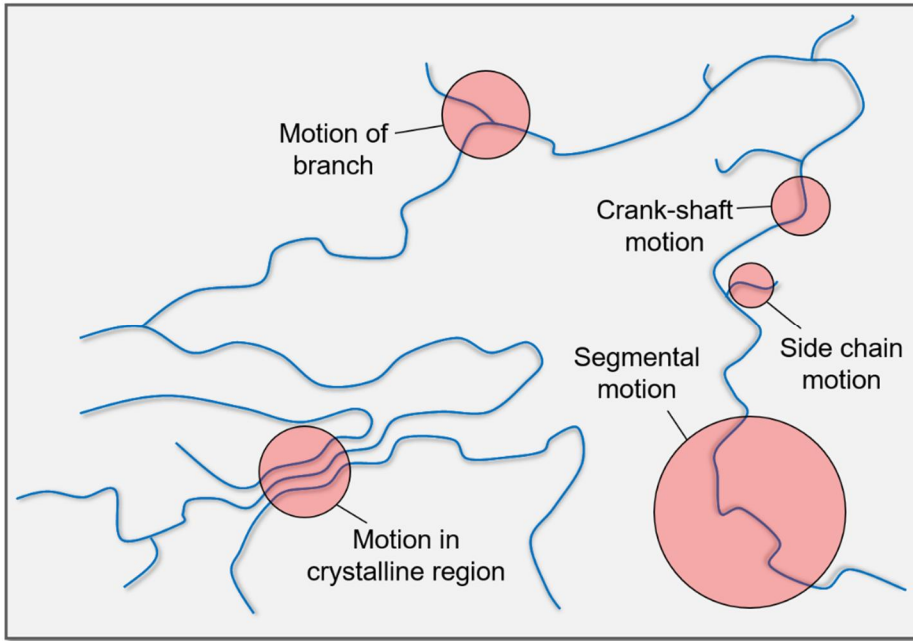


Figure I-5. Types of the molecular motions of polymer materials

Motion	Region	Nature	E_a (kJ/mol)	Remarks
---------------	---------------	---------------	----------------	----------------

Table I-2. Activation energy for typical motions observed in polymer materials

Primary main chain	Crystalline (C)	Hindered oscillations, rotations, or translations	> 125	May be activated by defects
Primary main chain	Amorphous (A)	Large-scale rotation and translation	< 400	Associated with glass transition and breakdown of long-range order
Secondary chain motion	C/A	Localized motion of interfacial materials: folds, tie molecules, chains of low molecular weight	40-60	Characteristic of linear polymers: some or all chains may be involved
Side group	C/A	Highly localized motion of specific moiety	8-80	Usually in the low-temperatures below T_g
Impurity motions	C/A	Motions induced by trace solvents or plasticizers	-	Dominates relaxation at low temperature

I-4. Research Objectives

In this study, effect of chain mobility on the various properties of the electrospun polymer nanofibers was investigated. First, crystal structure and chain mobility of polymer nanofibers was discussed. Based on the results for the above discussion, effect of the changes in molecular mobility on drug release and crystallization properties of polymer nanofibers was studied.

Chapter II: Crystal structure and chain mobility of nylon 6 nanofibers (NFs) with different shape and diameter were studied.⁵¹ NFs were successfully fabricated by electrospinning. Topology of crystalline chains was observed by observing crystal structure and melting behaviors. It was revealed that crystalline chains became highly packed as diameter of NFs decreases. In addition, melting temperature of NFs increased with decreasing diameter, suggesting that crystalline chains are highly packed with decreasing diameter of NFs. To investigate the chain topology of amorphous region, molecular mobility was observed by spin-lattice relaxation time in laboratory frame (T_1) measurement. It was shown that activation energy for reptation-like displacement of amorphous chains increased with a decrease in diameter. Therefore, it was concluded that both crystalline chains and amorphous chains are highly packed in ultrathin polymer nanofibers.

Chapter III: The effect of change in chain mobility on drug release property of polymer nanofibers was investigated.⁵² Cellulose acetate/Sulindac nanofibers (CNs) with different diameters were fabricated. Analysis on crystal structure, chemical structure and thermal properties of CNs were conducted. It was observed that cellulose acetate and Sulindac were well mixed and formed homogeneous structure, without forming aggregation or their own crystal structure. The topology of amorphous chains was studied by T_1 measurement. The molecular mobility of CNs decreased with decreasing diameter, indicating that chains are highly packed as diameter decreases. Drug release property of CNs was investigated under conditions simulating the physiological conditions of the transdermal drug delivery system. test was conducted. Drug release kinetics of CNs were analyzed based on Fick's laws of diffusion. It was concluded that drug release from CNs gets slower when diameter of CNs gets smaller.

Chapter IV: Effect of chain mobility solvent-assisted crystallization process for meta-Aramid nanofibers (*mANFs*) was studied.⁵³ First, the optimum solvent composition (ethylene glycol (EG):DMAc ratio) was investigated. The optimum volume ratio of the solvent was found to be 5:6 (EG:DMAc). In addition, the degree of crystallization of *mANFs* at 120 °C was high compared to that of *mANFs* treated at 90 and 150 °C. *mANFs* crystallized at optimum condition exhibited superior chemical stability and mechanical strength

compared to the as-synthesized *m*ANF. The crystallinity of *m*ANFs with an average diameter of 120, 170 and 270 nm treated at the optimum crystallization condition was observed. It was concluded that crystallinity was decreased as diameter of *m*ANFs decreased, suggesting that highly packed chains in thin nanofibers are less likely to be crystallized.

Chapter V: Vapor-induced crystallization process for *m*ANFs was developed and effect of size on the crystallization of *m*ANFs was investigated. The optimum solvent composition for the crystallization process was determined to be 1:2.6 (aniline:DMAc, volume ratio). The crystallization efficiency of *m*ANFs was most high at 120 °C. The degree of crystallization decreased with decreasing diameter when *m*ANFs were treated in the optimum crystallization condition. The results suggested in chapter IV and V indicated that nanofibers having larger diameter could be preferred when highly crystallized nanofibers is needed.

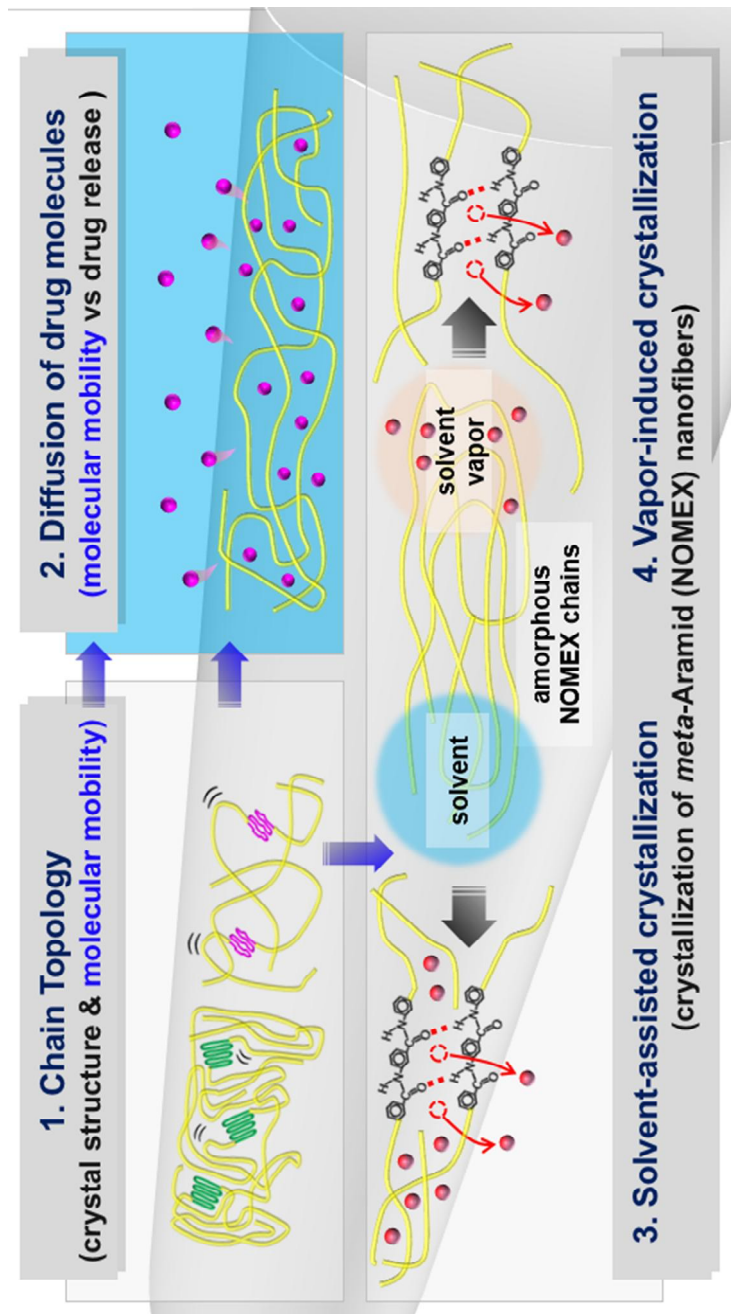


Figure I-6. Research objectives: Investigation of size-dependent behaviors of electrospun polymer nanofibers.

References and Notes

1. Zhang, C.; Guo, Y.; Priestley, R. D., Glass Transition Temperature of Polymer Nanoparticles under Soft and Hard Confinement. *Macromolecules* **2011**, *44* (10), 4001-4006.
2. Arinstein, A.; Burman, M.; Gendelman, O.; Zussman, E., Effect of supramolecular structure on polymer nanofibre elasticity. *Nature nanotechnology* **2007**, *2* (1), 59-62.
3. Chandran, S.; Begam, N.; Padmanabhan, V.; Basu, J. K., Confinement enhances dispersion in nanoparticle–polymer blend films. *Nature Communications* **2014**, *5*.
4. Di Benedetto, F.; Camposeo, A.; Pagliara, S.; Mele, E.; Persano, L.; Stabile, R.; Cingolani, R.; Pisignano, D., Patterning of light-emitting conjugated polymer nanofibres. *Nat Nanotechnol* **2008**, *3* (10), 614-9.
5. Rharbi, Y., Reduction of the glass transition temperature of confined polystyrene nanoparticles in nanoblends. *Phys Rev E Stat Nonlin Soft Matter Phys* **2008**, *77* (3 Pt 1), 031806.
6. Rittigstein, P.; Priestley, R. D.; Broadbelt, L. J.; Torkelson, J. M., Model polymer nanocomposites provide an understanding of confinement effects in real nanocomposites. *Nat Mater* **2007**, *6* (4), 278-82.

7. Shin, K.; Obukhov, S.; Chen, J. T.; Huh, J.; Hwang, Y.; Mok, S.; Dobriyal, P.; Thiagarajan, P.; Russell, T. P., Enhanced mobility of confined polymers. *Nat Mater* **2007**, *6* (12), 961-5.
8. Yao, J.; Bastiaansen, C.; Peijs, T., High Strength and High Modulus Electrospun Nanofibers. *Fibers* **2014**, *2* (2), 158-186.
9. Xu, C., Aligned biodegradable nanofibrous structure: a potential scaffold for blood vessel engineering. *Biomaterials* **2004**, *25* (5), 877-886.
10. Rotella, C.; Wübbenhorst, M.; Napolitano, S., Probing interfacial mobility profiles via the impact of nanoscopic confinement on the strength of the dynamic glass transition. *Soft Matter* **2011**, *7* (11), 5260-5266.
11. Martínez-Tong, D. E.; Vanroy, B.; Wübbenhorst, M.; Nogales, A.; Napolitano, S., Crystallization of Poly(l-lactide) Confined in Ultrathin Films: Competition between Finite Size Effects and Irreversible Chain Adsorption. *Macromolecules* **2014**, *47* (7), 2354-2360.
12. Forrest, J. A.; Dalnoki-Veress, K.; Stevens, J. R.; Dutcher, J. R., Effect of free surfaces on the glass transition temperature of thin polymer films. *Physical review letters* **1996**, *77* (10), 2002-2005.
13. Forrest, J. A.; Dalnoki-Veress, K.; Dutcher, J. R., Interface and chain confinement effects on the glass transition temperature of thin polymer

- films. *Physical Review E - Statistical Physics, Plasmas, Fluids, and Related Interdisciplinary Topics* **1997**, *56* (5 SUPPL. B), 5705-5716.
14. Mattsson, J.; Forrest, J. A.; Börjesson, L., Quantifying glass transition behavior in ultrathin free-standing polymer films. *Physical Review E - Statistical Physics, Plasmas, Fluids, and Related Interdisciplinary Topics* **2000**, *62* (4 B), 5187-5200.
 15. Kim, S.; Roth, C. B.; Torkelson, J. M., Effect of nanoscale confinement on the glass transition temperature of free-standing polymer films: Novel, self-referencing fluorescence method. *Journal of Polymer Science, Part B: Polymer Physics* **2008**, *46* (24), 2754-2764.
 16. Ellison, C. J.; Torkelson, J. M., The distribution of glass-transition temperatures in nanoscopically confined glass formers. *Nature materials* **2003**, *2* (10), 695-700.
 17. Ellison, C. J.; Torkelson, J. M., Sensing the glass transition in thin and ultrathin polymer films via fluorescence probes and labels. *Journal of Polymer Science Part B: Polymer Physics* **2002**, *40* (24), 2745-2758.
 18. Napolitano, S.; Wübberhorst, M., Structural relaxation and dynamic fragility of freely standing polymer films. *Polymer* **2010**, *51* (23), 5309-5312.
 19. Rotella, C.; Napolitano, S.; Wübberhorst, M., Segmental mobility and glass transition temperature of freely suspended ultrathin polymer membranes. *Macromolecules* **2009**, *42* (5), 1415-1417.

20. Fakhraai, Z.; Forrest, J. A., Probing slow dynamics in supported thin polymer films. *Phys Rev Lett* **2005**, *95* (2), 025701.
21. McKenzie, I.; Daley, C. R.; Kiefl, R. F.; Levy, C. D.; MacFarlane, W. A.; Morris, G. D.; Pearson, M. R.; Wang, D.; Forrest, J. A., Enhanced high-frequency molecular dynamics in the near-surface region of polystyrene thin films observed with beta-NMR. *Soft Matter* **2015**, *11* (9), 1755-61.
22. Paeng, K.; Swallen, S. F.; Ediger, M. D., Direct measurement of molecular motion in freestanding polystyrene thin films. *J Am Chem Soc* **2011**, *133* (22), 8444-7.
23. Alcoutlabi, M.; McKenna, G. B., Effects of confinement on material behaviour at the nanometre size scale. *Journal of Physics: Condensed Matter* **2005**, *17* (15), R461-R524.
24. McKenna, G. B., Confit III. Summary and perspectives on dynamics in confinement. *The European Physical Journal Special Topics* **2007**, *141* (1), 291-301.
25. Keddie, J. L.; Jones, R. A. L.; Cory, R. A., Interface and surface effects on the glass-transition temperature in thin polymer films. *Faraday Discussions* **1994**, *98*, 219-230.
26. Rittigstein, P.; Priestley, R. D.; Broadbelt, L. J.; Torkelson, J. M., Model polymer nanocomposites provide an understanding of

- confinement effects in real nanocomposites. *Nature materials* **2007**, *6* (4), 278-282.
27. Zhang, C.; Guo, Y.; Priestley, R. D., Confined glassy properties of polymer nanoparticles. *Journal of Polymer Science Part B: Polymer Physics* **2013**, *51* (7), 574-586.
28. Zhang, C.; Guo, Y.; Shepard, K. B.; Priestley, R. D., Fragility of an Isochorically Confined Polymer Glass. *The journal of physical chemistry letters* **2013**, *4* (3), 431-6.
29. Huang, Z. M.; Zhang, Y. Z.; Kotaki, M.; Ramakrishna, S., A review on polymer nanofibers by electrospinning and their applications in nanocomposites. *Composites Science and Technology* **2003**, *63* (15), 2223-2253.
30. Greiner, A.; Wendorff, J. H., Functional self-assembled nanofibers by electrospinning. In *Advances in Polymer Science*, 2008; Vol. 219, pp 107-171.
31. Dzenis, Y., Spinning continuous fibers for nanotechnology. *Science* **2004**, *304* (5679), 1917-1919.
32. Charernsriwilaiwat, N.; Opanasopit, P.; Rojanarata, T.; Ngawhirunpat, T.; Supaphol, P., Preparation and characterization of chitosan-hydroxybenzotriazole/polyvinyl alcohol blend nanofibers by the electrospinning technique. *Carbohydrate Polymers* **2010**, *81* (3), 675-680.

33. Kang, Y.; Choi, Y. K.; Kim, H. J.; Song, Y.; Kim, H., Preparation of anti-bacterial cellulose fiber via electrospinning and crosslinking with β -cyclodextrin. *Fashion and Textiles* **2015**, *2* (1), 11.
34. Chen, H.; Liu, Z.; Cebe, P., Chain confinement in electrospun nanofibers of PET with carbon nanotubes. *Polymer* **2009**, *50* (3), 872-880.
35. Ji, Y.; Li, C.; Wang, G.; Koo, J.; Ge, S.; Li, B.; Jiang, J.; Herzberg, B.; Klein, T.; Chen, S.; Sokolov, J. C.; Rafailovich, M. H., Confinement-induced super strong PS/MWNT composite nanofibers. *EPL (Europhysics Letters)* **2008**, *84* (5), 56002.
36. Wong, S.-C.; Baji, A.; Leng, S., Effect of fiber diameter on tensile properties of electrospun poly(ϵ -caprolactone). *Polymer* **2008**, *49* (21), 4713-4722.
37. Burman, M.; Arinstein, A.; Zussman, E., Do surface effects explain the unique elasticity of polymer nanofibers? *EPL (Europhysics Letters)* **2011**, *96* (1), 16006.
38. Arinstein, A., Confinement mechanism of electrospun polymer nanofiber reinforcement. *Journal of Polymer Science, Part B: Polymer Physics* **2013**, *51* (9), 756-763.
39. Arinstein, A.; Zussman, E., Electrospun polymer nanofibers: Mechanical and thermodynamic perspectives. *Journal of Polymer Science Part B: Polymer Physics* **2011**, *49* (10), 691-707.

40. Mohan, S. D.; Mitchell, G. R.; Davis, F. J., Chain extension in electrospun polystyrene fibres: a SANS study. *Soft Matter* **2011**, *7* (9), 4397.
41. Tan, E. P.; Lim, C. T., Effects of annealing on the structural and mechanical properties of electrospun polymeric nanofibres. *Nanotechnology* **2006**, *17* (10), 2649-54.
42. Lim, C. T.; Tan, E. P. S.; Ng, S. Y., Effects of crystalline morphology on the tensile properties of electrospun polymer nanofibers. *Applied Physics Letters* **2008**, *92* (14), 141908.
43. Tan, E. P. S.; Lim, C. T., Physical properties of a single polymeric nanofiber. *Applied Physics Letters* **2004**, *84* (9), 1603-1605.
44. Dzenis, Y., Spinning Continuous Fibers for Nanotechnology. *Science* **2004**, *304* (5679), 1917.
45. Teo, W. E.; Ramakrishna, S., A review on electrospinning design and nanofibre assemblies. *Nanotechnology* **2006**, *17* (14), R89-R106.
46. Greiner, A.; Wendorff, J. H., Electrospinning: a fascinating method for the preparation of ultrathin fibers. *Angew Chem Int Ed Engl* **2007**, *46* (30), 5670-703.
47. Zhang, Q.; Liu, W.; Dai, P., Study of glass transition of Gd³⁺ doped poly(methyl methacrylate) by the internal friction method. *Polymer* **1998**, *39* (16), 3787-3792.

48. Priya, L.; Jog, J. P., Poly(vinylidene fluoride)/clay nanocomposites prepared by melt intercalation: Crystallization and dynamic mechanical behavior studies. *Journal of Polymer Science Part B: Polymer Physics* **2002**, *40* (15), 1682-1689.
49. Lee, J.; Grein-Iankovski, A.; Narayanan, S.; Leheny, R. L., Nanorod Mobility within Entangled Wormlike Micelle Solutions. *Macromolecules* **2017**, *50* (1), 406-415.
50. Holt, A. P.; Griffin, P. J.; Bocharova, V.; Agapov, A. L.; Imel, A. E.; Dadmun, M. D.; Sangoro, J. R.; Sokolov, A. P., Dynamics at the Polymer/Nanoparticle Interface in Poly(2-vinylpyridine)/Silica Nanocomposites. *Macromolecules* **2014**, *47* (5), 1837-1843.
51. Chung, J.; Chung, J. W.; Priestley, R. D.; Kwak, S.-Y., Confinement-Induced Change in Chain Topology of Ultrathin Polymer Fibers. *Macromolecules* **2018**, *51* (11), 4229-4237.
52. Chung, J.; Kwak, S. Y., Effect of nanoscale confinement on molecular mobility and drug release properties of cellulose acetate/sulindac nanofibers. *Journal of Applied Polymer Science* **2019**, *136* (33), 47863.
53. Chung, J.; Kwak, S.-Y., Solvent-assisted heat treatment for enhanced chemical stability and mechanical strength of meta-aramid nanofibers. *European Polymer Journal* **2018**, *107*, 46-53.

CHAPTER II

Investigation on crystal structure and molecular mobility of nylon 6 nanofibers

II-1. Introduction

To investigate the chain structure of polymer nanofibers, polyamides have been frequently selected as model polymer because polyamide nanofibers with uniform morphology could be easily fabricated by electrospinning.¹⁻³ Arkadii *et al.* revealed that nylon 6,6 nanofibers with diameter less than 500 nm show an increased Young's modulus.³ The nylon 6,6 nanofibers lost their enhanced physical strength at high temperature above T_g . In addition, nylon 6 nanofibers could also be an appropriate candidate to discuss about size effect because nylon 6 nanofibers are well-electrospun without adding extra salts. The absence of salt molecules means that the size effect could be studied without considering the effect of salts molecules. Furthermore, nylon 6 is beneficial to analyze the molecular conformation of both crystalline region and amorphous region. Nylon 6 has two common crystalline phases, α - and γ -phases.⁴⁻⁸ The α -phase possesses highly extended chain conformation while γ -

phase consists of pleated chains. The higher molecular rigidity of α -phase leads to the higher mechanical strength and thermal stability of α -phase than those of γ -phase. Hence, observation of phase structure and thermal properties of nylon 6 crystals enables the analysis on topology of crystalline chains. Moreover, molecular mobility of nylon 6 amorphous chains has been successfully investigated by solid-state NMR spectroscopy.⁹⁻¹² This signifies that the solid-state NMR spectroscopy is an attractive approach to reveal the size effect on the molecular conformation of amorphous chains in nylon 6 nanofibers.

In this study, the confinement effect of electrospun NFs was investigated by observing the changes in the crystalline and amorphous chain morphologies of nylon 6 NFs with variations in their thickness and shape. It was found that the chains in the crystalline region were more rigidly packed when the diameter of the cylindrical NFs was smaller than 120 nm. In addition, the molecular motion of the amorphous chains was suppressed with a decrease in the NF diameter, indicating that the amorphous chains were also closely packed, forming a rigid structure. These results suggest that as the size of NF decreases, the chain topology of NF is mainly affected by the confinement effect rather than the increase of the free surface ratio, whereas chain topology of polymer nanoparticles and thin films are largely affected by free surface. It is likely that the confinement effect of NF such as the formation of densely

packed chain topology is induced by their stretching during the spinning process. To the best of our knowledge, this is the first report to show the correlation between chain confinement and chain packing in nanofibers. The elucidation of this relationship will help in understanding the fundamental properties of NFs when used in various fields.

II-2. Experimental Section

II-2-1. Materials

Formic acid (CH₂O₂), rhodamine B (rhB), and polycaprolactam (nylon 6) were purchased from Sigma-Aldrich and were used as received without further purification. The viscosity-averaged molecular weight (M_v) of nylon 6 was determined using the Mark-Houwink equation ($K = 22.6 \times 10^{-5}$ dL/g and $a = 0.82$)¹³; the value of M_v was calculated to be 236 kDa.

II-2-2. Fabrication of cylindrical and ribbon-like nylon 6 nanofibers

The electrospinning solution was prepared by dissolving granules of nylon 6 in formic acid at 50°C for 6 h. The concentration of the nylon 6 solution was varied from 13 to 34 wt%. The solutions with the higher nylon 6 concentration above 34 wt% could not be electrospun properly because of their high viscosity. The nylon 6 NFs were fabricated using an electrospinning system (NanoNC, Korea) composed of a high-DC-voltage supply, and a rotating drum collector and a syringe pump. The nylon 6 solution was placed in a 10-mL syringe attached to a steel needle with an internal diameter of 0.33 mm. The collector was covered with aluminum foil and placed 10 cm from the tip of the needle. A positive voltage of 20–25 kV was applied to the

syringe needle tip while a negative voltage of -5 kV was applied to the collector. The relative humidity and temperature were maintained at 40–50% and 20–25°C, respectively, during the electrospinning process. The rotating speed of the roller was 100 rpm with 62.8 cm/s of tangential velocity, and the flow rate was kept at 0.2 mL/h. The fabricated nylon 6 NFs with a cylindrical morphology are hereafter denoted as c-NF-x (where x indicates the diameter) while the fabricated ribbon-like nylon 6 NFs are denoted as r-NF-x-y (where x and y indicate the width and thickness, respectively). Thermal treatment was conducted at 370 K for 24 h.

II-2-3. Fabrication of rhB-loaded nylon 6 nanofibers

To prepare the rhB-loaded NFs, an rhB/nylon 6 solution was prepared by dissolving rhB and nylon 6 in formic acid at 50°C for 6 h. The rhB/nylon 6 mass ratio in the solution was fixed at 1/100. The rhB-loaded nylon 6 NFs were electrospun under the same conditions as those used to fabricate the nylon 6 NFs mentioned above. The fabricated rhB-loaded nylon 6 NFs are hereafter denoted as Rh-NF-x (where x indicates the diameter).

II-2-4. Characterization

The viscosity of solution was measured by observing the solution rheology (DHR-2). The morphologies and sizes of the nylon 6 NFs were determined using field-emission scanning electron microscopy (FE-SEM, JSM-6700F), which was performed at an accelerating voltage of 10 kV. The diameter, width, and height of the NFs were measured from the FE-SEM images using an image analysis software (EyeViewAnalyzer, Digiplus Inc.). The average fiber diameter, width, and height were determined by evaluating 100 fibers at random from the FE-SEM images. The crystal structures of the fibers were evaluated using XRD analysis (New D8 Advance), which was performed for 2θ values of 10–40° using Cu K_{α} radiation ($\lambda = 0.154$ nm). The thermal behaviors of the NFs were investigated by differential scanning calorimetry (DSC, DSC-Q1000), which was performed under a nitrogen atmosphere over the temperature range of 25–250°C at a heating rate of 10°C/min. The chemical states of the NFs were studied by X-ray photoelectron spectroscopy (XPS, AXIS-His) using monochromatic Mg K_{α} radiation. All the binding energies were calibrated with respect to the C 1s peak at 284.5 eV.

The ^1H spin-lattice relaxation time in the laboratory frame (T_1) was measured through solid-state nuclear magnetic resonance (NMR) analysis (solid-state NMR, Minispec mq20), which was performed at 0.47 Tesla using a

permanent magnet. The applied proton resonance frequency was 19.95 MHz. The samples were placed in 10-mm-diameter NMR tubes. The T_1 measurements were conducted at temperatures of 200–370 K using a Bruker BVT-3000 temperature control unit. During the measurements, the temperature was maintained within ± 0.1 K of the target temperature. To prevent the deformation of the chain conformations, the measurements were performed by increasing the temperature from 200 K at intervals of 10 K. Further, the temperature was held at each level for 20 min prior to data collection. At each temperature, the ^1H NMR free induction decay was determined using a 90° pulse with a length of 2.04 μs , a 180° pulse with a length of 4.26 μs , a recycle delay, T , greater than $5 T_1$, and a receiver gain of 61–107 dB. The T_1 measurements were performed by analyzing the magnetization decay after the inversion-recovery pulse sequence (180° - τ - 90°). Finally, T_1 was determined by exponentially plotting the magnetization intensity versus τ .

A solvent mixture of formic acid and deionized water was used to measure the actual amount of rhB in the Rh-NFs. The Rh-NFs were dissolved in formic acid, and the solution was diluted with distilled water. The formic acid/water ratio was 1:9 by mass. The absorbance of this solution was measured using an ultraviolet-visible (UV-Vis) spectrometer (Lambda 25) at a wavelength of 558 nm. The amount of rhB in the NFs was calculated by comparing the

absorbance of the diluted solution and that of the calibration solution. The release test was performed by immersing 25–35 mg of the Rh-NFs in 40 mL of deionized water at room temperature. Samples of the solution were collected at specified periods, which ranged from 0 to 24 h after immersion. The rhB concentration of the solution was measured with a UV-Vis spectrometer.

II-3. Results and Discussion

II-3-1. Crystal structure of Nylon 6 nanofibers

The shape and sizes of the nylon 6 NFs were determined by FE-SEM. The FE-SEM images showed that the fabricated NFs had a uniform and bead-free shape (see Fig. II-1 and Fig. II-2). NFs with a cylindrical shape (i.e., c-NFs) were obtained when the polymer concentration in the electrospinning solution was 13–29 wt%, with the diameter of the c-NFs increasing from 70 to 370 nm with an increase in the polymer concentration. Ribbon-shaped nanofibers (i.e., r-NFs) were obtained for a polymer concentration of 30–33 wt%, with the width of the r-NFs increasing and their thickness decreasing with an increase in the polymer concentration. The viscosity of the solution and other variables for electrospinning process were listed in Table II-1. It is well known that nylon 6 exhibits two typical crystalline phases, namely, the α -phase and the γ -phase. The α -phase consists of highly extended planar zigzag chains. These chains are antiparallel to the adjacent ones and highly densely packed, resulting in high thermal stability and good mechanical strength. On the other hand, the chains in the γ -phase crystals are less densely packed than those in the α -phase crystals^{2, 14}. As a result, the γ -phase crystals exhibit relatively lower thermal stability and mechanical strength as compared to those of the α -phase crystals.

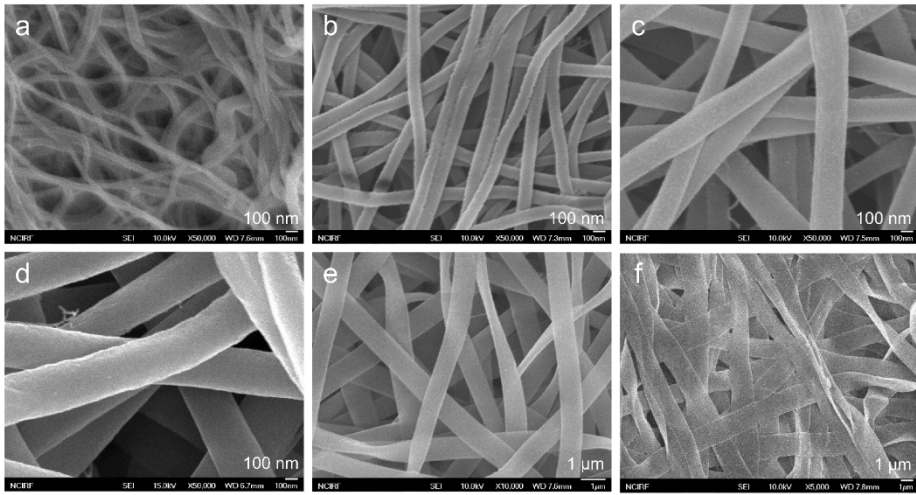


Figure II-1. FE-SEM images of (a) c-NF-70, (b) c-NF-120, (c) c-NF-220, (d) c-NF-370, (e) r-NF-800-350, and (f) r-NF-1140-270. Scale bars are 100 nm in (a), (b), (c), and (d), and 1 μ m in (e) and (f).

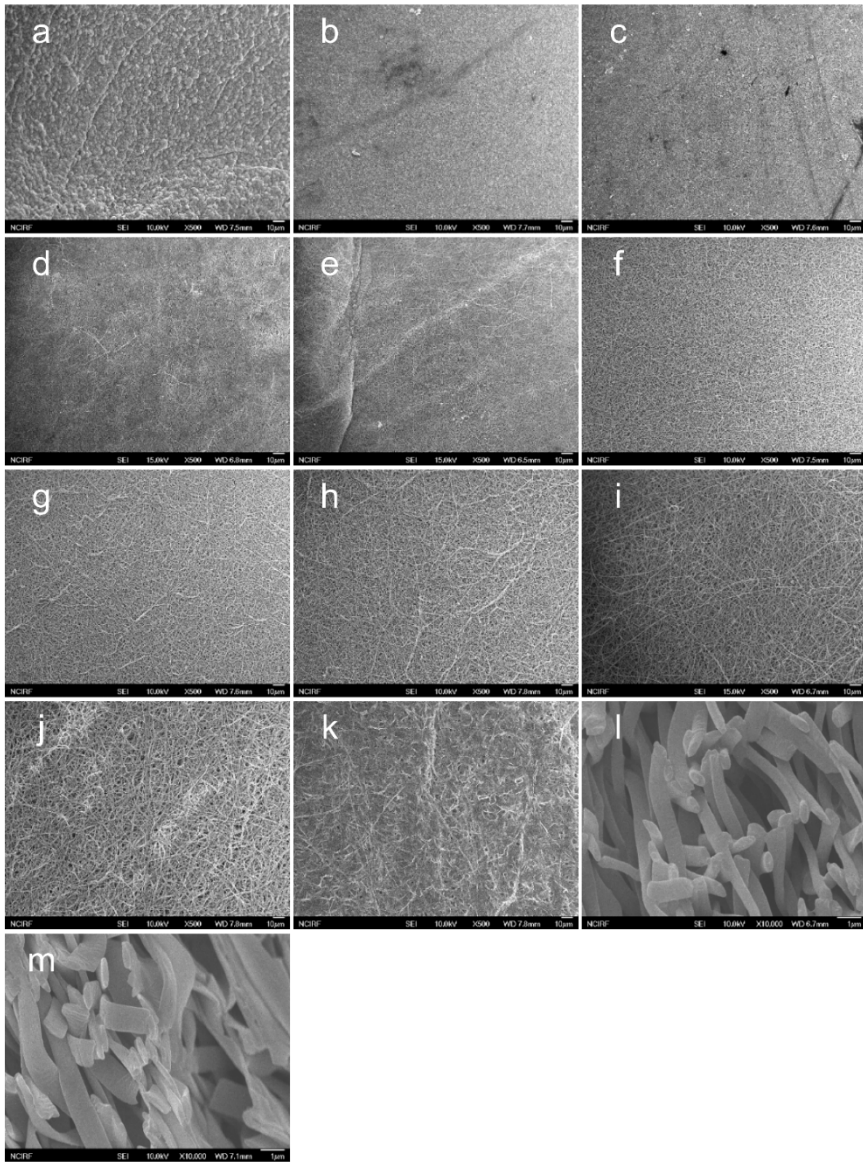


Figure II-2. FE-SEM images of (a) c-NF-70, (b) c-NF-80, (c) c-NF-100, (d) c-NF-120, (e) c-NF-200, (f) c-NF-220, (g) c-NF-270, (h) c-NF-290, (i) c-NF-370, (j) r-NF-800-350, (k) r-NF-1140-270 at low magnification and cross-section of (l) r-NF-800-350 and (m) r-NF-1140-270 at high magnification.

Table II-1. Concentration and viscosity of nylon 6/formic acid solution at 298 K and electrostatic field applied to the nozzle tip for each samples

Sample	c-NF-70	c-NF-80	c-NF-100	c-NF-120	c-NF-200	c-NF-220
Concentration (wt%)	13	16	18	20	22	24
Viscosity (Pa·s)	0.60	1.04	2.29	4.59	5.22	5.34
Voltage (kV)	20	20	20	20	20	20
Sample	c-NF-270	c-NF-290	c-NF-370	r-NF-800-350	r-NF-1140-270	
Concentration (wt%)	26	28	30	32	34	
Viscosity (Pa·s)	7.24	9.19	12.77	18.01	30.26	
Voltage (kV)	20	25	25	25	25	

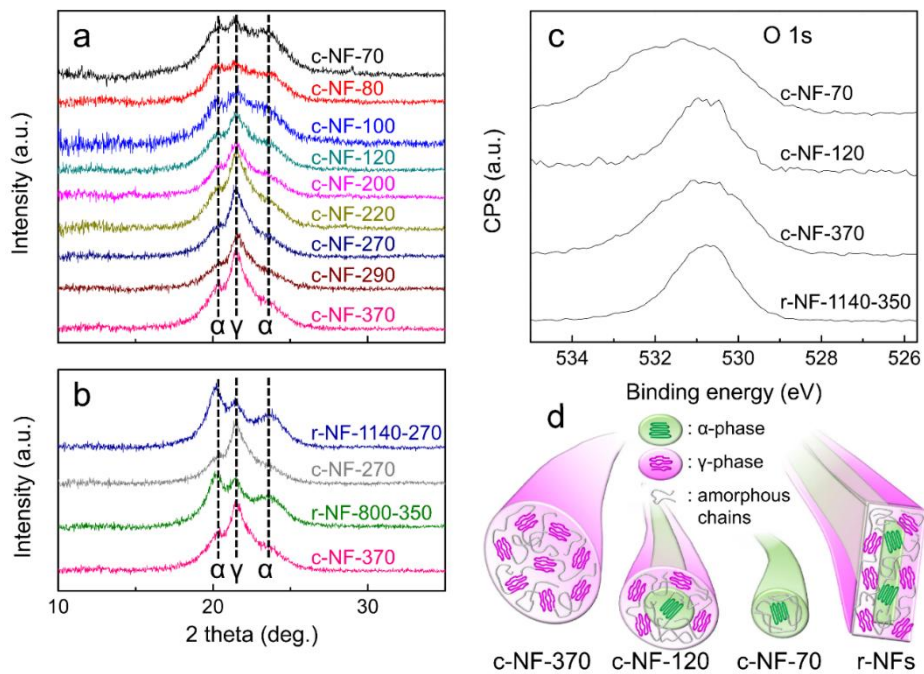


Figure II-3. WXR patterns of (a) nylon 6 nanofibers with different diameter from 70 to 370 nm and (b) nylon 6 nanofibers with different width and thickness, (c) O 1s XPS spectra of c-NF-70, c-NF-120, c-NF-370 and r-NF-1140-350, and (d) schematic illustration of crystal structure in nylon 6 nanofibers

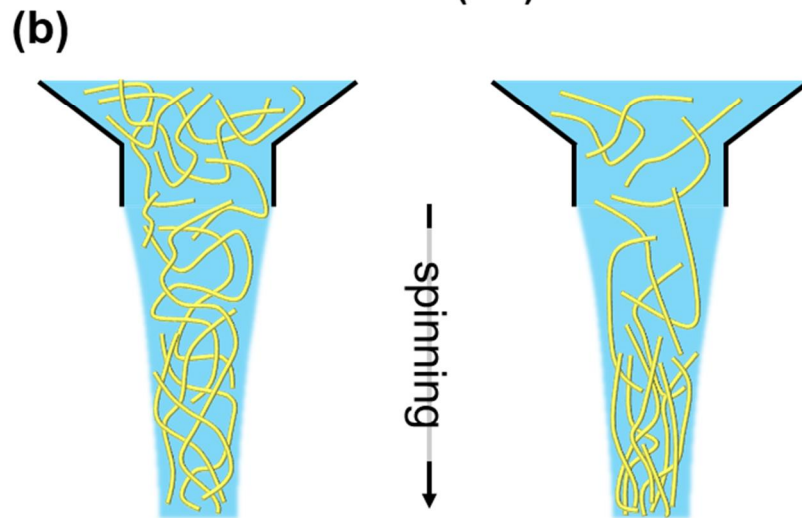
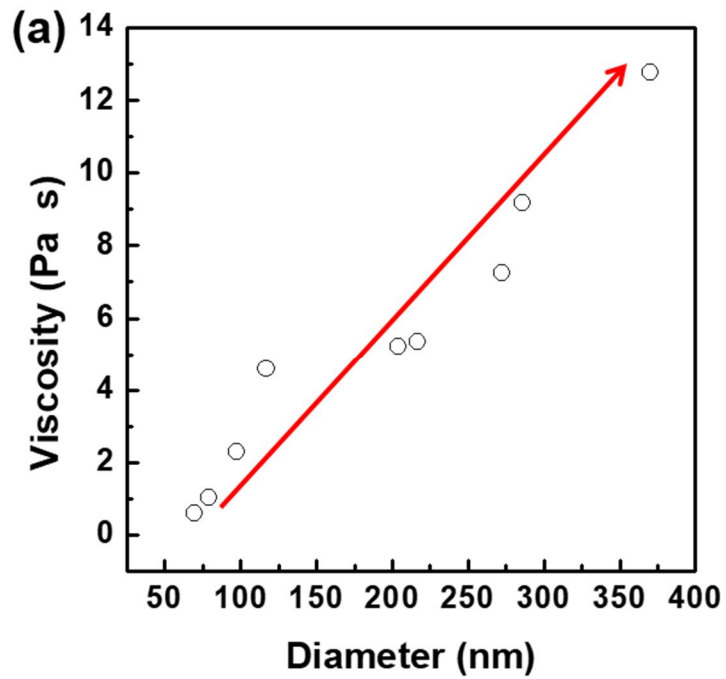


Figure II-4. (a) Viscosity of nylon 6 solution corresponding to the resulting diameter of nylon 6 nanofibers and (b) description

of the effect of solution viscosity on chain topology of nylon 6 nanofibers.

As shown in Fig. II-3 (a) and (b), all the NFs exhibit three diffraction peaks. These include peaks at $2\theta = 20.3^\circ$ and 23.3° , which correspond to the α -phase, and peak at $2\theta = 21.3^\circ$, which corresponds to the γ -phase. In the case of c-NF-370, the NFs with the largest thickness, the diffraction peak at 21.3° is dominant, indicating that the γ -phase was the primary crystal phase. On the other hand, the diffraction peaks at 20.3° and 23.3° increased in intensity with a decrease in the diameter from 370 to 120 nm while that at 21.3° decreased. In particular, as the diameter was decreased further from 120 to 70 nm, the fraction of the α -phase increased sharply. These results clearly indicate that the chains in the crystalline region of the NFs became more densely packed as the diameter of the c-NFs was decreased. Meanwhile, despite the thickness of the r-NFs being similar to that of the c-NFs, the r-NFs with a larger width than that of the c-NFs exhibited a more prominent α -phase (Fig. II-3 (b)). These results suggest that the chains in the crystalline region of the r-NFs were more densely packed as compared to those in the c-NFs.

Typically, the α -phase is formed when the nylon 6 chains are slowly crystallized. Therefore, the slow evaporation of the nylon 6 solution or the slow cooling of molten nylon 6 results in the formation of the α -phase. In contrast, the γ -phase is formed by the rapid evaporation of the solvent or the fast cooling of the melt during the fiber-spinning process. Because the nylon 6 solution evaporates rapidly during the electrospinning process, γ -phased nylon

6 NFs are as common^{4, 8, 15}. On the other hand, a highly concentrated electrospinning solution readily reaches the solidification line, resulting in the formation of a solid skin layer during the initial step of the electrospinning process. Because this solid skin layer prevents the evaporation of the solvent, the chains in the inside of the jet solution have enough time to form stable crystals, that is, the α -phase. Thus, the ribbon-shaped NFs or r-NFs primarily consisted of α -phase crystals, owing to the slow evaporation of the solvent because of the high concentration of the spinning solution used, as shown in Fig. II-3 (b)¹⁶⁻¹⁷. However, the increase in the α -phase portion of the cylindrical NFs with a decrease in the NF diameter cannot be explained by this solvent evaporation process, because, contrary to expectations, the lower the concentration of the electrospinning solution was, the higher was the amount of α -phase crystals formed in c-NFs. Hence, the surface structure of the NFs was analyzed using XPS in order to observe the changes in their crystal phase with a decrease in their diameter.

As shown in Fig. II-3 (c), c-NF-370 exhibits a typical O 1s peak at 530.8 eV corresponding to the γ -phase⁶. When considering that XRD results indicated that c-NF-370 had the γ -phase as the primary crystal phase, the XPS spectrum revealed that both the surface layer and the inner layer of c-NF-370 primarily consisted of γ -phase crystals, owing to the high evaporation rate during the electrospinning of c-NF-370. The XPS spectrum of c-NF-120 also contained

an O 1s peak at 530.8 eV attributable to the γ -phase. However, it can be seen from the XRD results that the α -phase fraction gradually increased with a decrease in the diameter from 370 to 120 nm. Thus, it can be surmised that the portion of the α -phase in the inner layer of the c-NFs increased with the decrease in the diameter from 370 to 120 nm, while the surfaces of the c-NFs continued to consist of the γ -phase. In contrast to the XPS spectra of c-NF-370 and c-NF-120, that of c-NF-70 exhibited a broad O 1s peak at approximately 532.5 eV corresponding to a relatively compact α -phase, indicating that surface layer of c-NF-70 consisted of α -phase crystals. This observation was interesting because the surface layer of these NFs should have consisted of γ -phase crystals, given the rapid evaporation of the solvent at the surface of the NFs during the electrospinning process. This phenomenon can probably be attributed to an increase in the degree of chain stretching and packing by a decrease in the extent of chain entanglement with a decrease in the concentration of the nylon 6 electrospinning solution. As listed in Fig. II-4 (a) and Table II-2, the viscosity of the solution for NF-370 was 20 times higher than that of solution for NF-70. The severely entangled chains could not be easily stretched and might form an unstable crystalline phase. On the contrary to this, relatively less entangled chains could easily be unfolded to create a rigid crystal structure. Thus, the results of the XPS and XRD measurements confirmed that the electrospun NFs had a highly packed crystalline morphology as the primary crystal phase, when the polymeric

chain in NFs was confined with diameters smaller than a certain threshold, regardless of the characteristics of their surface and inner layers. The description of the correlation between solution viscosity and chain topology of nanofibers is shown in Fig. II-4. As a consequence, it was presumable that such confinement effect on crystal structure of ultra thin polymer fibers would lead to the physical hardening of the NFs. The crystalline morphology of NFs with various size and shape is described in Fig. II-3 (d).

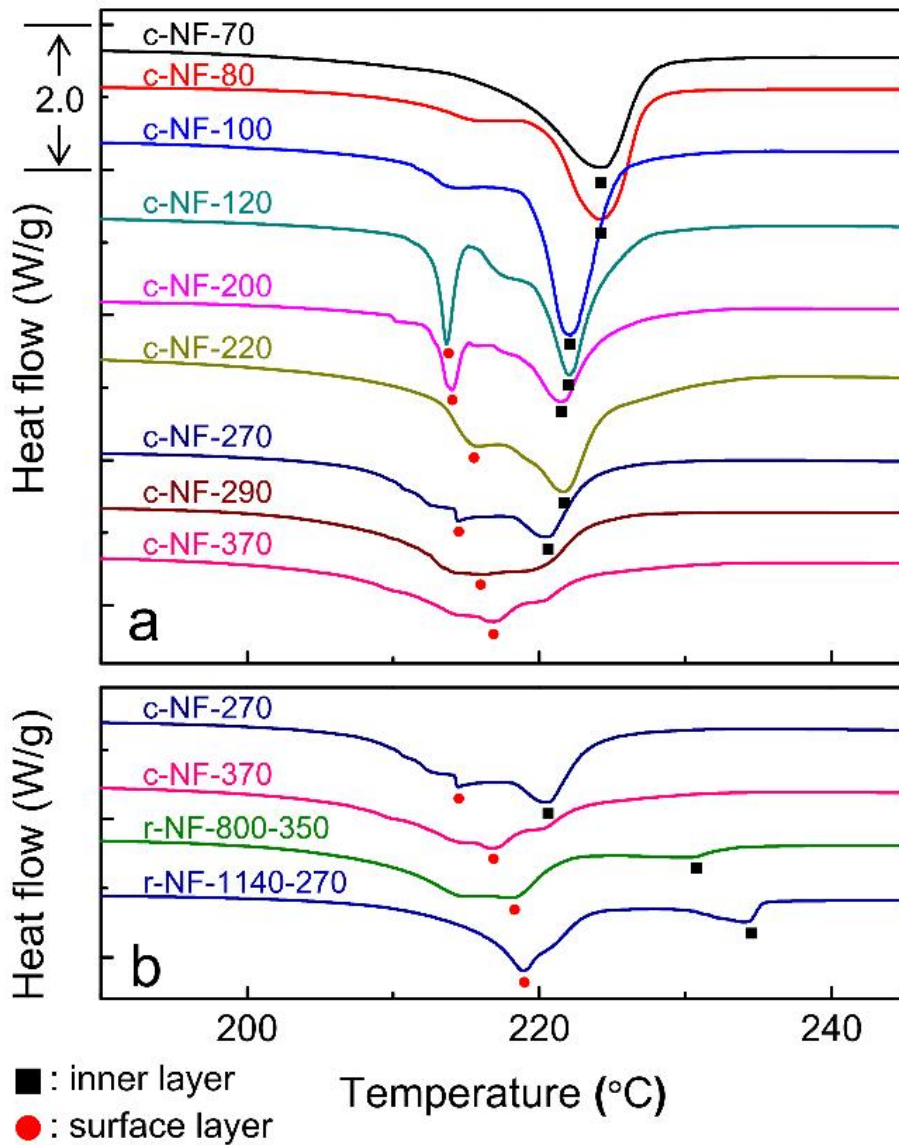


Figure II-5. DSC curves of (a) nylon 6 nanofibers with different diameter from 70 to 370 nm and (b) nylon 6 nanofibers with different width and thickness.

The confinement effect in the NFs was further verified by observing the melting behaviors of the NFs by DSC analysis. As shown in Fig. II-5 (a), the DSC curve of c-NF-370 exhibits a broad melting peak at 216.0°C, which corresponds to the γ -phase¹⁸. However, with a decrease in the NF diameter from 370 to 120 nm, two melting peaks corresponding to the α -phase (high T_m) and γ -phase (low T_m) were observed, with the intensity of the α -phase peak being significantly higher. In addition, the peak corresponding to the γ -phase at the surface of the NFs shifted to a lower temperature and the peak related to the α -phase crystals in the inner layer of the c-NFs shifted to a higher temperature with a decrease in the NF diameter. In particular, a single melting peak related to the α -phase was observed when the diameter was decreased from 120 to 70 nm. These results clearly indicate that the proportion of the highly packed α -phase crystals in the NFs was significantly higher than that of the γ -phase crystals; this was in good agreement with the XRD and XPS results, which had suggested that the extent of chain packing in the NFs increases owing to the nanoconfinement effect.

Meanwhile, the T_m of the α -phase of all the r-NFs was abnormally higher than the T_m of the α -phase of the c-NFs while the T_m of the γ -phase of the r-NFs was similar to that of the γ -phase of the c-NFs (see Fig. II-5 (b)). In addition, the T_m of the α -phase of r-NF-1140-270 was higher than that of the α -phase of r-NF-800-350. These results indicated that the r-NFs had a structure

consisting of more densely packed chains than did the c-NFs and that the degree of chain packing of the r-NFs increased with an increase in their width, owing to the high concentration of the spinning solution used. Thus, it can be concluded that the formation of crystals in r-NFs is strongly dependent on the conventional evaporation process.

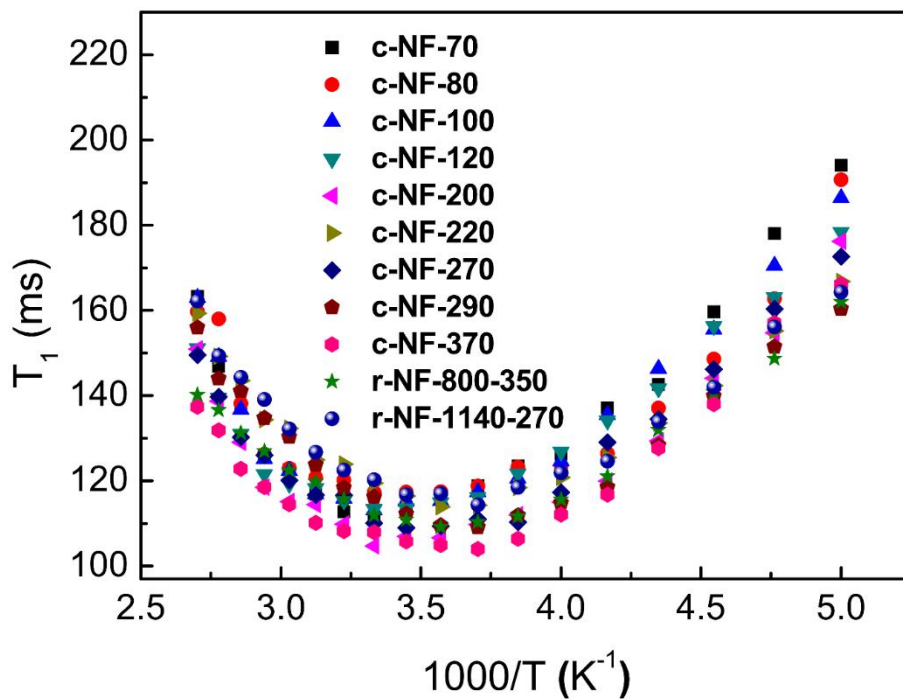


Figure II-6. ^1H T_1 vs the inverse temperature ($1000/T$) of nylon 6 nanofibers with different size and shape

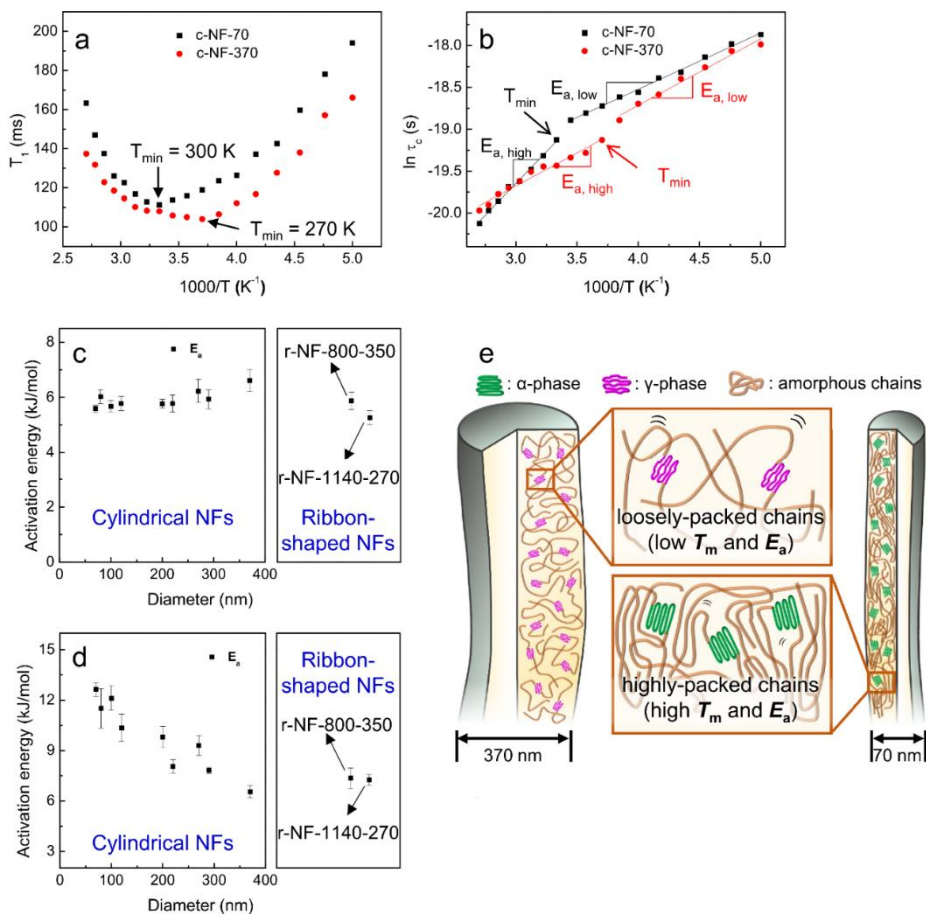


Figure II-7. (a) 1H T_1 vs the inverse temperature ($1000/T$) and (b) logarithmic plot of the correlation time, τ_c vs the inverse temperature ($1000/T$) of NF-70 and NF-370, the activation energy of nylon 6 nanofibers obtained at the temperature (c) lower than T_{min} and (d) higher than T_{min} , and (e) schematic illustration of chain topology in nylon 6 nanofibers

Table II-2. T_{\min} of the nylon 6 nanofibers

Sample	c-NF-70	c-NF-80	c-NF-100	c-NF-120	c-NF-200	c-NF-220
T_{\min} (K)	300	300	300	300	300	280
Sample	c-NF-270	c-NF-290	c-NF-370	r-NF-800-350	r-NF-1140-270	
T_{\min} (K)	290	270	270	280	270	

II-3-2. Molecular mobility of nylon 6 nanofibers

In order to investigate the nanoconfinement effect in the amorphous region of the NFs, the molecular mobility of the NFs was evaluated through measurements of the spin-lattice relaxation time in the laboratory frame, T_1 , using ^1H solid-state NMR. The spin-lattice relaxation is induced by the reptation-like displacement of the nylon 6 amorphous chains, thus the amorphous structure can be analyzed through T_1 measurements^{9, 19}. The spin-lattice relaxation behaviors of the NFs were fitted using a double-exponential decay model, and the T_1 value for the double-exponential decay process was obtained using the following equation:

$$M_\tau = M_{e,A} \left[1 - 2 \exp\left(\frac{-\tau}{T_{1,A}}\right) \right] + M_{e,B} \left[1 - 2 \exp\left(\frac{-\tau}{T_{1,B}}\right) \right] \quad (1)$$

where M_e is the intensity of the excited spin at equilibrium ($\tau \geq 5 T_1$) and M_τ is the intensity of the excited spin at the delay time (τ). Component A, which exhibited rapid decay initially, was related to spin diffusion, while component B originated from the spin-lattice relaxation induced by the molecular motion of the chains²⁰⁻²¹. Therefore, the $T_{1,B}$ value was suitable for evaluating the molecular mobility of the amorphous chains in the NFs.

The T_1 values of c-NF-70 and c-NF-370 are compared in Fig. II-7 (a). It can be seen that the T_1 values of c-NF-70 and c-NF-370 decreased with an increase in the temperature from 200 K onwards, eventually reaching a minimum at T_{\min} . In most cases, the molecular motion of the amorphous chains is too slow to induce spin-lattice relaxation at low temperatures, leading to a relatively long T_1 value. With an increase in the temperature, however, the frequency of the molecular motion of the NFs increases progressively, eventually becoming equal to the resonance frequency at T_{\min} , such that spin-lattice relaxation is induced. Hence, the T_1 values of the c-NF-70 and c-NF-370 decreased with an increase in the temperature when the temperature was lower than T_{\min} ($T < T_{\min}$), as shown in Fig. II-7 (a). On the other hand, at temperatures greater than T_{\min} ($T > T_{\min}$), the T_1 values of c-NF-70 and c-NF-370 increased with the increase in the temperature because the molecular motion at the higher temperatures was too rapid to induce spin-lattice relaxation. As a result, the T_1 values of the NFs exhibited U-shaped curves, with the minimum T_1 value at T_{\min} . As can be seen from Fig. II-7 (a), the T_{\min} value for c-NF-70 (300 K) was almost 30°C higher than that for c-NF-370 (270 K). This result indicated that a greater amount of thermal energy was required to induce resonance with respect to the reptation motion of c-NF-70 as compared to that for c-NF-370. In other words, the molecular motion of the amorphous chains in c-NF-70 was suppressed to a greater

degree by the adjacent chains than was the case in c-NF-370. As listed in Table II-2, the T_{\min} value of the c-NFs increased with a decrease in the diameter from 370 to 200 nm. This suggested that the smaller the diameter of the NFs, the higher the degree of constraint, owing to which the amorphous chains of the NFs became closely packed in the nanoconfining surroundings. The T_{\min} did not increase with decreasing diameter of c-NFs from 200 to 70 nm, implying that the closely-packed chain structure might not significantly affect the local segmental motion at a relatively high temperature, 300 K. Meanwhile, the r-NFs showed T_{\min} values similar to that of c-NF-370, indicating that the amorphous chains in the r-NFs were not highly constrained.

The activation energy for the reptation-like displacements, E_a , was determined, in order to quantitatively evaluate the molecular mobility of the NFs. For this, the T_1 values of the NFs were analyzed based on the Bloembergen-Purcell-Pound (BPP) theory. As per this theory, the spin-lattice relaxation behavior can be described using the following equation:

$$\frac{1}{T_1} = \frac{3}{10} \left(\frac{\mu_0}{4\pi} \right)^2 \frac{\gamma^4 \hbar^2}{\langle r \rangle^6} \left[\frac{\tau_c}{1 + \omega_0^2 \tau_c^2} + \frac{4\tau_c}{1 + 4\omega_0^2 \tau_c^2} \right] \quad (2)$$

where γ is the magnetogyric ratio of the observed species, \hbar is the reduced Planck's constant or Dirac constant ($\hbar = h/2\pi$), $\langle r \rangle$ is the average intramolecular interdipole distance, and ω_0 is the angular frequency. τ_c is the correlation time, which can be considered the average time required for the motional events. Thus, the τ_c value obtained from the T_1 value of NFs represents the time required for a single amorphous chain to sense topological constraints at the tube surface. The E_a value was determined from the Arrhenius equation and the correlation time as determined by the BPP equation:

$$\tau_c = \tau_0 \exp\left(\frac{E_a}{RT}\right) \quad (3)$$

where τ_0 is the correlation time at infinite temperature. As shown in Fig. II-6 (b), the activation energy for c-NF-70 in the high-temperature region, that is, for temperatures higher than T_{\min} , $E_{a, \text{high}}$, (12.6 eV) was considerably higher than that in the low-temperature region, that is, for temperatures lower than T_{\min} , $E_{a, \text{low}}$, (5.60 eV) while the $E_{a, \text{low}}$ of c-NF-370 was similar its $E_{a, \text{high}}$. In the low-temperature region, T_1 is mainly determined by the molecular motion on the small scale rather than by large-scale molecular motion because the

latter is too slow to induce spin-lattice relaxation. However, the T_1 value is suitable for evaluating large-scale molecular motion at high temperatures because such motion become fast enough in this case to induce spin-lattice relaxation. That is to say, the scale of the molecular motion changes with an increase in the temperature²². Typically, the activation energy as determined from T_1 for high temperatures is higher than that obtained from T_1 at low temperatures, because large-scale molecular motion is restricted by chain entanglement and intermolecular interactions, in contrast to local motion, which occurs freely. Accordingly, considering that c-NF-70 exhibited an $E_{a, \text{high}}$ value twice as large as its $E_{a, \text{low}}$ value, large-scale reptation motion in c-NF-70 was severely constrained by the strong enthalpic structure. On the other hand, in the case of c-NF-370, which exhibited similar $E_{a, \text{high}}$ and $E_{a, \text{low}}$ values, the amorphous chains exhibited similar temperature dependence both at the small scale and the large scale, indicating that the suppression of the large scale molecular motions by the enthalpic restriction was less formed than c-NF-70. Therefore, the amorphous chains of c-NF-70 were probably more packed than those of c-NF-370, resulting in a highly enhanced enthalpic structure. Indeed, as shown in Fig. II-7 (c), the $E_{a, \text{low}}$ values of all the c-NFs were 5–7 kJ/mol, with there being no noticeable dependence on size. In contrast, the $E_{a, \text{high}}$ value of the c-NFs increased dramatically with a decrease in the diameter from 370 to 70 nm (Fig. II-7 (d)). As above mentioned, this increase in $E_{a, \text{high}}$ indicated that the amorphous chains of the c-NFs became

more closely packed with a decrease in the NF diameter, probably owing to the nanoconfinement of ultra thin polymer fibers via the spinning-induced stretching of the chains at the nanoscale. Meanwhile, the r-NFs also exhibited $E_{a, \text{high}}$ values similar to their $E_{a, \text{low}}$ values, suggesting that the amorphous chains in the r-NFs were not highly packed.

It was suggested that polymer NFs lose their enhanced mechanical strength at temperatures higher than T_g due to the structural relaxation of amorphous chains. To investigate the changes in the amorphous chain structure of the NFs at high temperatures, the T_1 values of c-NF-70 and c-NF-370 during the first and second heating processes were compared. It was shown in Fig. II-7 that microstructure of c-NF-70 and c-NF-370 was not disrupted by the heating process. The T_1 values of c-NF-370 as measured during the second heating process were similar to the T_1 values measured during the first heating process (Table II-3). This suggests that the amorphous chains of c-NF-370 did not undergo structural relaxation during the heating process. On the other hand, the T_1 value of c-NF-70 as measured during the second heating process was different from that measured in the first heating process. In the second heating process, the T_{min} of c-NF-70 shifted from 300 to 280 K. In addition, as shown in Table II-3, the $E_{a, \text{high}}$ for c-NF-70 during the second heating process was much lower than that during the first heating process. These decrease in the T_{min} and the $E_{a, \text{high}}$ values of c-NF-70 suggested that the hard confinement of

the chains was relieved because of the thermal energy, resulting in the breakup of the highly packed structure. This result is in keeping with that of a previous study, which reported that NFs lose their enhanced physical strength at temperatures higher than T_g . When the thermal treatment was applied to c-NF-70 at 370 K for 24 h, the $E_{a, \text{high}}$ value of c-NF-70 decreased to 6.55 eV. This implies that the highly-packed chain structure could be completely relieved by the thermal treatment for sufficient time. Based on the results of the analyses of the crystal phase and molecular mobility of the amorphous chains of the NFs, the size-dependent nanoconfinement effect observed in the NFs is illustrated in Fig. II-7 (e).

Table II-3. Activation energy of c-NF-70 and c-NF-370 obtained from correlation time, τ_c of the first, second heating process and first heating process after the annealing process.

Sample	$E_{a, \text{high}}$ (eV)	$E_{a, \text{high}}$ (eV)
c-NF-70 (1 st)	5.58	12.64
c-NF-70 (2 nd)	6.42	7.99
c-NF-70 (after annealing)	5.81	6.55
c-NF-370 (1 st)	6.61	6.55
c-NF-370 (2 nd)	6.70	6.94
c-NF-370 (after annealing)	6.11	6.57

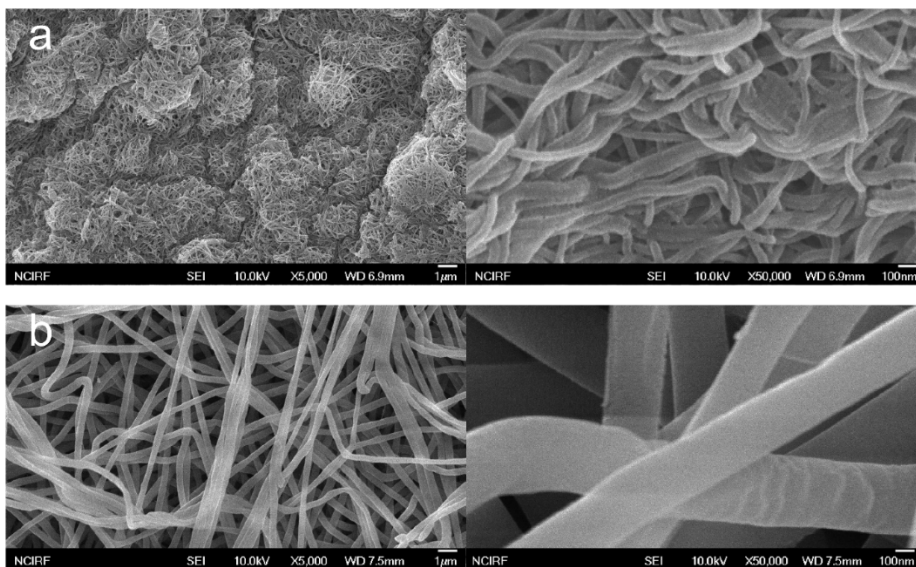


Figure II-8. FE-SEM images of (a) c-NF-70 and (b) c-NF-370 after the measurement of T_1 at a temperature range from 200 to 370 K.

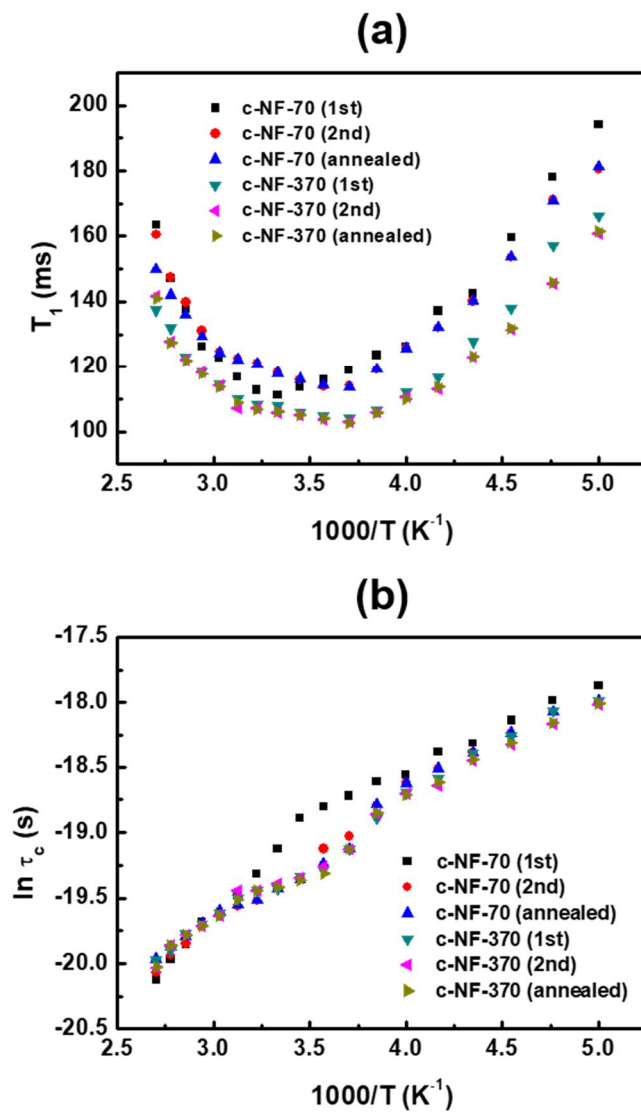


Figure II-9. (a) ^1H T_1 vs the inverse temperature ($1000/T$) and (b) logarithmic plot of the correlation time, τ_c vs the inverse temperature ($1000/T$) of c-NF-70 and c-NF-370 during the two heating cycles

II-3-3. Molecular diffusion in nylon 6 nanofibers

The confinement effect on the chain topology of ultra thin polymer fibers was investigated further by observing the release of rhB from rhB-loaded nylon 6 NFs (Rh-NFs). As shown in Fig. II-10 (a), Rh-NFs with average diameters of 60, 140, and 250 nm were well fabricated. The XRD pattern of Rh-NF-250 contained a clear diffraction peak related to the γ -phase (Fig. II-10 (b)). However, with a decrease in the NF diameter, the proportion of the α -phase increased. In addition, the DSC melting peak of the Rh-NFs shifted to a higher temperature with a decrease in the diameter of the Rh-NFs (Fig. II-10 (c)). These results were in good agreement with those in the case of the c-NFs and suggested that the chain packing topology with decreasing the diameter also occurred in the organic-dye-loaded NFs. As shown in Fig. II-10 (d), the rhB in the NFs was released rapidly in a short period, with the amount of the dye released plateauing at less than 100%. It was suggested that organic dyes embedded within the inner layer of NFs are not released readily whereas those on the outer layer are easily released.²³ Typically, the surface-to-volume ratio of the NFs increases with a decrease in the diameter, and thereby the increase in the amount of rhB should be released with a decrease in the diameter. As expected, the cumulative amount of dye released slightly increased from 50.8 to 56.9% due to the increase in the surface-to-volume ratio when the diameter was decreased from 250 to 140 nm. However, the

cumulative amount of dye released decreased sharply to 42.0% when the diameter of the Rh-NF was 60 nm, indicating that the polymer chains in Rh-NF-60 had a highly rigid topology, thus preventing the release of rhB. These results clearly show that the confinement significantly affects the physical properties of polymer fibers as well as their chain topology. Therefore, when designing and developing systems based on polymer NFs, the confinement effect in these NFs should be considered carefully.

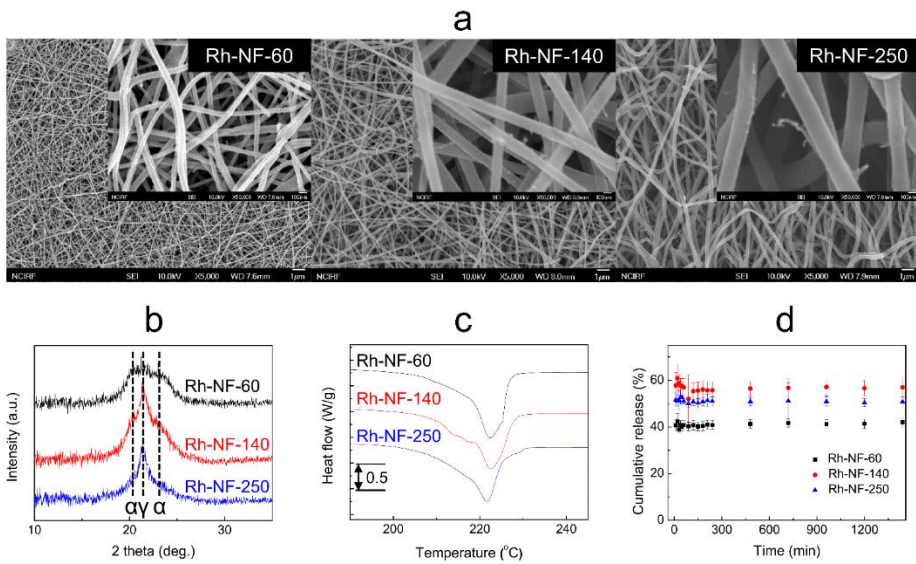


Figure II-10. (a) FE-SEM images, (b) XRD patterns and (c) DSC curves and (d) average release profiles of rhodamine B-loaded nylon6 nanofibers.

II-4. Conclusion

In this study, the effect of chain morphologies of nylon 6 NFs was investigated by observing the changes in crystalline phase and amorphous chain mobilities of the NFs with decreasing diameter. In the case of c-NF-370—the NFs with the largest diameter—it was confirmed that the crystalline chains in both surface and inner layers of NFs primarily had loosely packed γ -phase. However, with decrease in NF diameter from 370 to 120 nm, the crystalline chains started to become highly packed from the inner layer of the NFs. With further decrease in diameter from 120 to 70 nm, α -phase crystals with densely packed chains were observed even on the surfaces of the NFs. DSC results also showed that the proportion of the highly packed α -phase crystals increased with decreasing NF diameter. In addition, ^1H NMR spin-lattice relaxation time measurements revealed that the molecular mobility of the amorphous chains in the NFs became considerably slow with decrease in diameter, indicating that the amorphous chains were also closely packed. These features clearly revealed that study on the the molecular mobility of NFs could enable to observe the confinement-induced changes in chain structure which has not been observed by the conventional analysis of chain orientation and crystallinity. These features clearly revealed that the confinement endows the ultrathin polymeric fiber with a rigid chain structure. Indeed, such confined structures of ultrathin NFs significantly influenced the

release properties of the NFs; it was observed that the release of rhodamine B dye was severely retarded for the NFs with 60-nm diameter due to chain packing by confinement. In addition to release property, the mechanical and thermal properties, chemical stability, conductivity, and piezoelectricity of the NFs would also be affected by the changes in chain mobility. Thus, the confinement effect in ultrathin polymeric fibers should be necessarily taken into account for the design and development of advanced 1D polymer nanomaterials.

References and Notes

1. Arinstein, A.; Zussman, E., Electrospun polymer nanofibers: Mechanical and thermodynamic perspectives. *Journal of Polymer Science Part B: Polymer Physics* **2011**, *49* (10), 691-707.
2. Liu, Y.; Cui, L.; Guan, F.; Gao, Y.; Hedin, N. E.; Zhu, L.; Fong, H., Crystalline Morphology and Polymorphic Phase Transitions in Electrospun Nylon-6 Nanofibers. *Macromolecules* **2007**, *40* (17), 6283-6290.
3. Arinstein, A.; Burman, M.; Gendelman, O.; Zussman, E., Effect of supramolecular structure on polymer nanofibre elasticity. *Nat Nanotechnol* **2007**, *2* (1), 59-62.
4. Carrizales, C.; Pelfrey, S.; Rincon, R.; Eubanks, T. M.; Kuang, A.; McClure, M. J.; Bowlin, G. L.; Macossay, J., Thermal and mechanical properties of electrospun PMMA, PVC, Nylon 6, and Nylon 6,6. *Polymers for Advanced Technologies* **2008**, *19* (2), 124-130.
5. Kim, G.-M.; Michler, G. H.; Ania, F.; Calleja, F. J. B., Temperature dependence of polymorphism in electrospun nanofibres of PA6 and PA6/clay nanocomposite. *Polymer* **2007**, *48* (16), 4814-4823.
6. Čapková, P.; Čajka, A.; Kolská, Z.; Kormunda, M.; Pavlík, J.; Munzarová, M.; Dopita, M.; Rafaja, D., Phase composition and surface

- properties of nylon-6 nanofibers prepared by nanospider technology at various electrode distances. *Journal of Polymer Research* **2015**, 22 (6).
7. Kimura, N.; Kim, H.-K.; Kim, B.-S.; Lee, K.-H.; Kim, I.-S., Molecular Orientation and Crystalline Structure of Aligned Electrospun Nylon-6 Nanofibers: Effect of Gap Size. *Macromolecular Materials and Engineering* **2010**, 295 (12), 1090-1096.
 8. Giller, C. B.; Chase, D. B.; Rabolt, J. F.; Snively, C. M., Effect of solvent evaporation rate on the crystalline state of electrospun Nylon 6. *Polymer* **2010**, 51 (18), 4225-4230.
 9. Blinc, R.; Apih, T.; Jeglič, P.; Emri, I.; Prodan, T., Proton NMR study of molecular motion in bulk and in highly drawn fiber polyamide-6. *Applied Magnetic Resonance* **2005**, 29 (4), 577-588.
 10. Kwak, S. Y.; Kim, J. H.; Kim, S. Y.; Jeong, H. G.; Kwon, I. H., Microstructural investigation of high-speed melt-spun nylon 6 fibers produced with variable spinning speeds. *Journal of Polymer Science Part B: Polymer Physics* **2000**, 38 (10), 1285-1293.
 11. Buda, A.; Demco, D. E.; Bertmer, M.; Blümich, B.; Litvinov, V. M.; Penning, J. P., General Analytical Description of Spin-Diffusion for a Three-Domain Morphology. Application to Melt-Spun Nylon 6 Fibers. *The Journal of Physical Chemistry B* **2003**, 107 (22), 5357-5370.
 12. Kwak, S.-Y.; Kim, J. H.; Lee, J.-C., Correlation between local mobility and mechanical properties of high-speed melt-spun nylon-6 fibers.

- Journal of Polymer Science Part B: Polymer Physics* **2001**, 39 (10), 993-1000.
13. Ojha, S. S.; Afshari, M.; Kotek, R.; Gorga, R. E., Morphology of electrospun nylon-6 nanofibers as a function of molecular weight and processing parameters. *Journal of Applied Polymer Science* **2008**, 108 (1), 308-319.
 14. Li, Y.; Goddard Iii, W. A., Nylon 6 crystal structures, folds, and lamellae from theory. *Macromolecules* **2002**, 35 (22), 8440-8455.
 15. Stephens, J. S.; Chase, D. B.; Rabolt, J. F., Effect of the electrospinning process on polymer crystallization chain conformation in nylon-6 and nylon-12. *Macromolecules* **2004**, 37 (3), 877-881.
 16. Bazbouz, M. B.; Stylios, G. K., Alignment and optimization of nylon 6 nanofibers by electrospinning. *Journal of Applied Polymer Science* **2008**, 107 (5), 3023-3032.
 17. Tsou, S.-Y.; Lin, H.-S.; Wang, C., Studies on the electrospun Nylon 6 nanofibers from polyelectrolyte solutions: 1. Effects of solution concentration and temperature. *Polymer* **2011**, 52 (14), 3127-3136.
 18. Saeed, K.; Park, S. Y., Effect of nanoclay on the thermal, mechanical, and crystallization behavior of nanofiber webs of nylon-6. *Polymer Composites* **2012**, 33 (2), 192-195.
 19. Rachocki, A.; Kowalczyk, J.; Tritt-Goc, J., How we can interpret the T1 dispersion of MC, HPMC and HPC polymers above glass

- temperature? *Solid state nuclear magnetic resonance* **2006**, *30* (3-4), 192-7.
20. Bray, T.; Brown, G. C.; Kiel, A., Paramagnetic Relaxation of Fe³⁺ in Potassium Cobalticyanide. *Physical Review* **1962**, *127* (3), 730-737.
 21. Bourbigot, S.; VanderHart, D. L.; Gilman, J. W.; Awad, W. H.; Davis, R. D.; Morgan, A. B.; Wilkie, C. A., Investigation of nanodispersion in polystyrene–montmorillonite nanocomposites by solid-state NMR. *Journal of Polymer Science Part B: Polymer Physics* **2003**, *41* (24), 3188-3213.
 22. Ryu, S. Y.; Chung, J. W.; Kwak, S. Y., Probing the Role of Side-Chain Interconnecting Groups in the Structural Hydrophobicity of Comblike Fluorinated Polystyrene by Solid-State NMR Spectroscopy. *Langmuir : the ACS journal of surfaces and colloids* **2015**, *31* (34), 9473-82.
 23. Khansari, S.; Duzyer, S.; Sinha-Ray, S.; Hockenberger, A.; Yarin, A. L.; Pourdeyhimi, B., Two-stage desorption-controlled release of fluorescent dye and vitamin from solution-blown and electrospun nanofiber mats containing porogens. *Molecular Pharmaceutics* **2013**, *10* (12), 4509-4526.

CHAPTER III

Effect of Molecular Mobility on Drug Release Properties of Cellulose Acetate/Sulindac Nanofibers

III-1. Introduction

Oral delivery of drugs is commonly considered the most preferable and convenient drug delivery route because it allows easy administration and it is painless.¹⁻⁴ However, conventional oral drug delivery systems have shown limited bioavailability because of issues such as fast gastric emptying time and first-pass metabolism.⁵⁻⁸ To overcome such limitations of oral administration, various drug delivery systems (DDS) have been proposed. Among the various DDS, textile-based DDS through transdermal and in-vivo routes have been extensively studied because they are relatively free from gastrointestinal absorption, liver metabolism, and degradation of pharmaceutical compounds.⁹⁻¹⁴ Such advantages make textile-based DDS a promising alternative to oral delivery of drugs, and thus, the global medical textile market has grown to US \$14 billion.¹⁵

As a novel medical textile for drug delivery, electrospun polymer nanofiber

mats have attracted considerable interest owing to their high surface area, high porosity, biocompatibility, high loading capacity, and ease of operation.¹⁶⁻²⁴ For the successful application of polymer nanofibers to drug delivery system, the drug release mechanisms and kinetics of polymer nanofibers have been widely investigated.²⁵⁻²⁷ For instance, drug-related parameters such as molecular weight, drug loading procedure, drug-polymer interaction, and physical state of drug are known to affect the drug release from nanofibers.²⁸⁻²⁹ In addition, polymer parameters affecting drug release from nanofibers have been discussed. As a result, it has been revealed that the drug release properties of polymer nanofibers are considerably affected by polymer parameters including molecular weight, crystallinity, molecular structure, and composition of polymer nanofibers.³⁰⁻³¹

To investigate the size-dependent changes of polymer nanofibers, the correlation between molecular mobility and diameter of nylon 6 nanofibers was discussed in chapter II.³² It was observed that molecular motion of chains was significantly suppressed when the diameter of nylon 6 nanofibers decreased, implying that chains confined in a thin polymer nanofiber tend to form a rigid structure. In addition, the release of rhodamine B molecules from nylon 6 nanofibers was severely retarded when the diameter of the nanofibers decreased. These results imply that changes in the molecular mobility of chains could largely affect the drug release property of polymer nanofibers.

Hence, given that polymer nanofibers have great potential in the field of drug delivery, it has become important to investigate the effect of confinement on the drug release properties of polymer nanofibers.

Herein, the effect of nanoscale confinement on the drug release properties of polymer nanofibers was investigated by analyzing the molecular mobility and drug release kinetics of cellulose acetate/Sulindac nanofibers (CNs). The cellulose acetate chains in CNs had an amorphous structure. It was found that the activation energy (E_a) for both the main chain motion and the side chain motion of CNs tended to increase with decreasing diameter of CNs. These results indicated that the chains confined in ultrathin CNs formed a closely packed structure. In addition, drug release from CNs was significantly retarded with increasing E_a for both the main chain motion and the side chain motion of CNs, suggesting that the confinement-induced chain packing could lead to a slowing of drug release. To the best of our knowledge, this is the first report elucidating the correlation between the molecular mobility and drug release kinetics of polymer nanofibers. This elucidation will help in the proper designation and application of polymer nanofiber-based DDS.

III-2. Experimental Section

III-2-1. Materials

N, N-dimethylacetamide (DMAc, 99.8 %), cellulose acetate (CA, $M_n = 30,000$ Da; acetyl content = 39.8 wt%), Sulindac ($C_{20}H_{17}FO_3S$), and dimethyl sulfoxide (DMSO, $\geq 99.9\%$), were purchased from Sigma-Aldrich. Dimethyl ketone (Acetone, 99.5%) was purchased from SAMCHUN Chemical. All reagents were used as received without further purification. Highly deionized water with a resistivity of 18.0 M Ω cm was used throughout the experiments.

III-2-2. Preparation of CA/Sulindac nanofibers and bulk CA/Sulindac film

CA/Sulindac solution was prepared by dissolving CA and Sulindac powders in 2:1 v/v acetone/DMAc. The concentration of CA ranged from 17 to 21 w/v%, and the ratio between CA and Sulindac was fixed at 20 wt%. CA nanofibers (CNs) were fabricated by using electrospinning apparatus (NanoNC, Korea). The equipment was composed of a high DC-voltage supply, a rotating drum-type collector, and a syringe pump. The CA solution was placed in a 10 mL syringe, and a steel needle with an internal diameter of 0.33 mm was attached to the syringe tip. A collector was covered with aluminum

foil and placed 10 cm from the tip of the needle. 10 kV of positive voltage was applied to the syringe needle tip, and -5 kV of negative voltage was applied to the collector. The relative humidity and temperature were maintained in a range from 40% to 50% and 20 to 25 °C, respectively, during the electrospinning process. The rotating speed of the roller was 100 rpm and the flow rate was kept at 1 mL/h. The CA nanofibers were named as CN-x (where x indicates the diameter). The bulk CA/Sulindac film (BF) was prepared by drying CA/Sulindac in 2:1 v/v acetone/DMAc solution, which contains 20 w/v% of CA and 4 w/v% of Sulindac powders in air at room temperature for 48 h. The BF was then dried in a vacuum oven at 50 °C for 24 h.

III-2-3. Characterization

The morphology and size of the CNs and BF were observed using a field emission scanning electron microscope (FE-SEM, JSM-6700F) at an accelerating voltage of 10 kV. The diameters of the CNs were obtained from the FE-SEM images using image analysis software (EyeViewAnalyzer, Digiplus Inc.). The average fiber diameter was determined by observing 100 fibers from the FE-SEM images at random. The chemical integrity of Sulindac molecules in CNs and BFs was analyzed by attenuated total reflection Fourier-transform infrared (ATR FT-IR, Thermo Scientific Nicolet

iS5) spectroscopy with a spectral resolution of 0.5 cm^{-1} in the range $600\text{--}3000\text{ cm}^{-1}$. The thermal properties of the CNs and BF were investigated by differential scanning calorimetry (DSC, DSC-Q1000) measurements and a thermogravimetric analyzer (TGA, Q-5000 IR). DSC analysis was conducted under a nitrogen atmosphere over the temperature range of $25\text{ to }250\text{ }^{\circ}\text{C}$ at a heating rate of $10\text{ }^{\circ}\text{C min}^{-1}$. TGA was carried out in the temperature range of $40\text{ to }700\text{ }^{\circ}\text{C}$ at a heating rate of $10\text{ }^{\circ}\text{C min}^{-1}$ under a nitrogen atmosphere. The crystal structure of CNs and BF was defined by X-ray diffraction methods (XRD, New D8 Advance) over the 2θ range of $10\text{--}50^{\circ}$ using $\text{Cu K}\alpha$ radiation as the X-ray source ($\lambda = 0.154\text{ nm}$). The surface area was obtained from nitrogen adsorption–desorption isotherms collected at 77 K on a micromeritics apparatus (ASAP 2010).

The ^1H spin-lattice relaxation time in the rotating frame ($T_{1\rho}$) was measured using solid-state nuclear magnetic resonance analysis (solid-state NMR, Minispec mq20) at 0.47 Tesla using a permanent magnet. The frequency of the applied pulse for proton resonance was 19.95 MHz , and the spin-locking pulse frequency was 51 KHz . The samples were placed into 10-mm-diameter NMR tubes. The $T_{1\rho}$ measurements were conducted at temperatures ranging from $180\text{ to }360\text{ K}$ using a Bruker BVT-3000 temperature control unit. The temperature was maintained within $\pm 0.1\text{ K}$ of the target temperature during the $T_{1\rho}$ measurements. To avoid the deformation of chain conformation, the

$T_{1\rho}$ values were measured with increasing temperature from 180 K with an interval of 10 K. The temperature was held for 20 min prior to collecting data. The $T_{1\rho}$ measurements were performed by analyzing the magnetization decay after the spin-lock delay τ (i.e., 90° - τ) pulse sequence. Finally, the $T_{1\rho}$ values were obtained by exponentially plotting the magnetization intensity versus τ .

III-2-4. Release of Sulindac from CA/Sulindac nanofibers and bulk CA/Sulindac film

Drug release experiments were carried out under conditions simulating the physiological conditions of the transdermal drug delivery system. Acetate buffer aqueous solution with a pH of 5.5 was prepared by dissolving acetic acid and sodium acetate in deionized water. The actual drug content in CNs was measured by dissolving CNs in DMSO. Then, 0.5 mL of the CN/DMSO solution was mixed with 8 mL of the buffer solution. The absorbance of the diluted solution was measured using a UV-Vis spectrometer (Lambda 25) at a wavelength of 327 nm. Calibration solutions were prepared by dissolving Sulindac in mixture of 0.5 mL of DMSO and 8 mL of buffer solution. The absorbance at 327 nm of the calibration solution was measured using a UV-Vis spectrometer. The drug content in CNs was calculated by considering the mass of the dissolved sample and the observed absorbance.

The drug-release assay was performed by the total immersion method. To obtain the amount of Sulindac released from CNs, calibration solutions were prepared by dissolving Sulindac in buffer solution. The absorbance at 327 nm of the calibration solution was measured by UV-Vis spectrometer. The disk-shaped CNs with a diameter of 2.8 cm were immersed in 40 mL of the buffer solution and placed in a rotating bath at 37 °C. The weight and thickness of the disk-shaped CNs were 55–85 mg and 20–28 μm, respectively. The rotation rate of the bath was 150 rpm. 0.5 mL of the buffer solution was collected at a specified immersion period ranging from 0 to 20 h. The amount of released drug was measured by using a UV-Vis spectrometer. It was confirmed by the calibration experiment that the amount of Sulindac in the disk-shaped CNs is small enough to be dissolved in the buffer solution.

III-3. Results and Discussion

III-3-1. Characteristics of CA/Sulindac nanofibers and bulk CA/Sulindac Film

The morphology and size of CA/Sulindac nanofibers (CNs) and bulk CA/Sulindac film (BF) were observed by FE-SEM. In Fig. III-1, the FE-SEM images showed that CNs had a fibrous structure with a smooth surface. The BF exhibited a uniform surface without showing large holes or scratches. The diameter of CNs increased as the concentration of CA solution increased. The measured diameters of CNs were 350, 530, 620, and 850 nm. It was observed that CN-350, CN-530, CN-620, and CN-850 had a bead-free fiber shape. As a result, in the case of CNs with a bead-free fiber shape, the surface area increased with decreasing diameter from 850 to 350 nm (Table III-1). Because a high electrical potential is applied to the polymer solution to fabricate the nanofibers, it could be questionable whether the Sulindac molecules preserve their chemical integrity after the electrospinning process. To verify the chemical integrity of Sulindac, the actual amount of Sulindac incorporated in the CNs and BF was measured using UV-Vis spectroscopy. It was confirmed from Table III-1 that the relative drug contents of the samples were in a range from 19 to 20 wt% (Sulindac/CA), which was similar to the drug content of the initial polymer solution (20 wt%). This result indicates that most of the

Sulindac molecules could be incorporated in the nanofibers while retaining their characteristics in the electrospinning process.³³⁻³⁴ It was presumable that Sulindac exhibited high stability when a high voltage was applied to the polymer solution. In addition, it was observed that the thicknesses of the CN and BF mats were between 24 and 35 μm (Table III-1).

The thermal properties of the CNs and BF were observed using DSC and TGA analyses. In Fig. III-2 (a), the DSC curve for Sulindac exhibited a sharp endothermic peak at 185 $^{\circ}\text{C}$, which corresponded to the melt transition. Meanwhile, the DSC curve of CA powder exhibited a broad melting peak at 240 $^{\circ}\text{C}$. However, the DSC curves of CNs and BF exhibited a broad and a small endothermal peak below 210 $^{\circ}\text{C}$, without showing melting peaks for both Sulindac and CA (Fig. III-2 (b)). Since the chemical integrity of the Sulindac in the CNs and BF was intact, the absence of the melting peak for Sulindac implies that Sulindac is dispersed in the CA matrix without forming aggregates or crystals. In addition, the absence of the melting peak for CA suggested that CNs and BF had an amorphous structure. The TGA thermograms for the Sulindac, CA CNs, and BF are shown in Fig. III-2 (c). Sulindac exhibited two major weight losses over the temperature ranges of 220–290 $^{\circ}\text{C}$ and 320–400 $^{\circ}\text{C}$. The relative remaining weight of Sulindac at 700 $^{\circ}\text{C}$ was approximately 39% of its original weight, indicating that Sulindac had carbonized and formed char during heating.³⁴ CA had a major weight loss

at 270–380 °C corresponding to the thermal decomposition of chains. Meanwhile, the TGA curves for CNs and BF showed a continuous weight loss from 220 to 400 °C because the weight loss of Sulindac and CA occurred simultaneously. After the weight loss from 220 to 400 °C, the CNs and BF exhibited a higher relative weight above 400 °C than pure CA due to the high relative remaining weight of Sulindac in the CNs and BF at high temperature.

To investigate the crystal structure of the CNs and BF, XRD analysis was performed. As shown in Fig. III-2 (d), bulk Sulindac exhibited sharp XRD peaks, including the main peaks at 15.1° and 21.3°. In addition, the CA powder exhibited XRD peaks at 10.6°, 13.4°, 17.5°, 18.7°, 21.3°, 23.0°, 25.7°, and 27.2° corresponding to the CA crystals. In contrary, the CNs and BF did not exhibit any specific XRD peaks for Sulindac and CA crystals, suggesting that CNs and BF mainly had an amorphous structure. The XRD spectra of the CNs and BF agrees with the DSC results.

The interaction of CA with Sulindac was investigated by ATR FT-IR analysis. In Fig. III-3 (a), bulk Sulindac powder exhibited peaks such as COOH stretching at 1703 cm⁻¹, C-F stretching at 1157 cm⁻¹, and S=O stretching at 1007 cm⁻¹. CA powder showed characteristic peaks at 1750, 1380, and 1236 cm⁻¹ corresponding to C=O, C-CH₃, and C-O-C stretching, respectively. Meanwhile, ATR FT-IR spectra for CNs and BF exhibited the same peaks

shown in the spectra of Sulindac and CA powder. However, as shown in Fig. III-3 (b), the adsorption frequency of the C=O stretching peak for CNs and BF was lower than that for CA powder. The lower adsorption frequency indicates strong interactions between -COOH groups of Sulindac and C=O groups of CA by hydrogen bonding.³⁵⁻³⁶ Considering the XRD and DSC results showing that Sulindac was well dispersed in the CA matrix, it is likely that a large number of hydrogen bonds were formed between CA and Sulindac.

Table III-1. Surface area, drug content, and thickness of cellulose acetate/Sulindac nanofibers and bulk films.

Sample	Surface area (m ² /g)	Drug content (Sulindac/CA, wt%)	Thickness (μm)
CN-350	6.96	19.53	33.6 ± 3.1
CN-530	4.78	19.89	31.0 ± 2.2
CN-620	3.01	19.42	31.0 ± 4.5
CN-850	1.45	19.21	35.0 ± 5.2
BF	0.02	19.98	24.8 ± 8.9

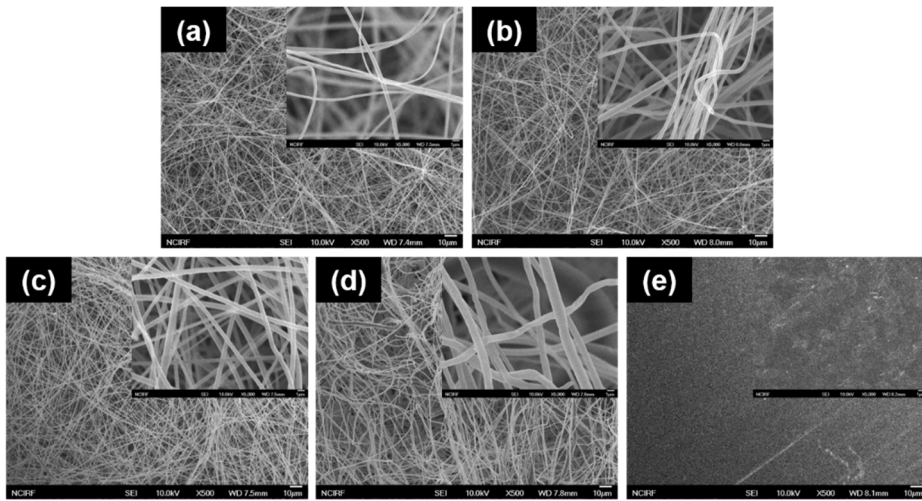


Figure III-1. FE-SEM images of (a) CN-350, (b) CN-530, (c) CN-620, (d) CN-850, and (e) BF.

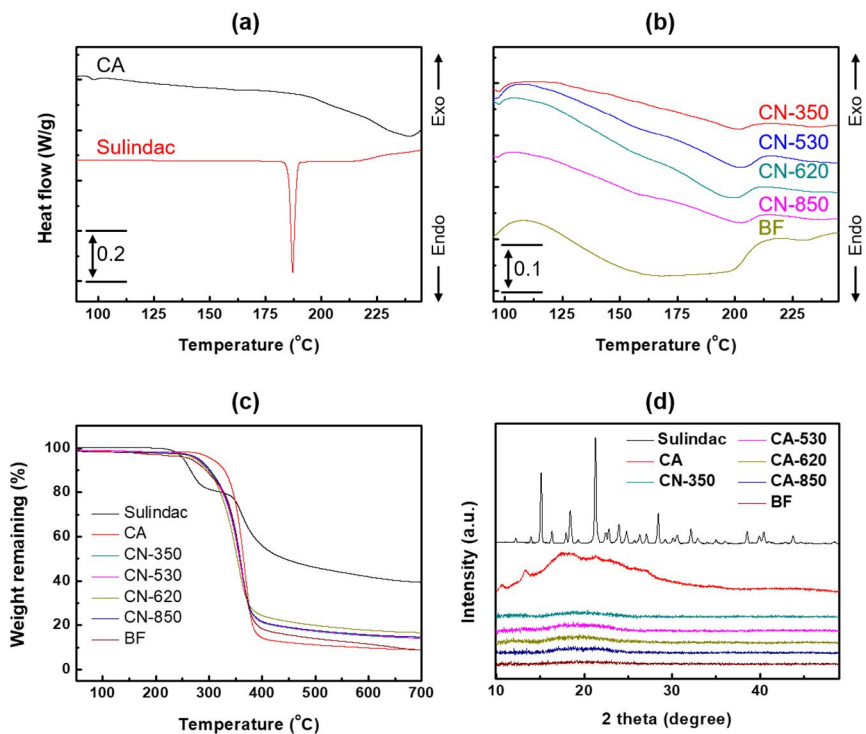


Figure III-2. DSC curves of (a) CA and Sulindac and (b) CA/Sulindac nanofibers and bulk CA/Sulindac film, (c) TGA curves of CA, Sulindac, CA/Sulindac nanofibers and bulk CA/Sulindac film, and (d) XRD.

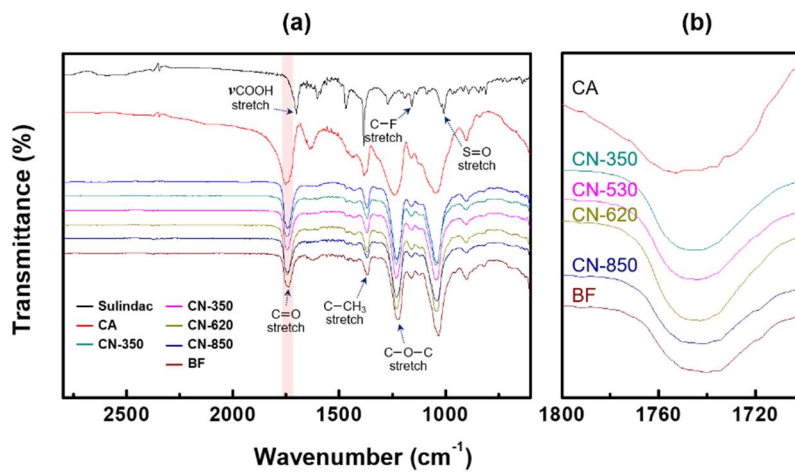


Figure III-3. (a) FT-IR spectra of CA, Sulindac, CA/Sulindac nanofibers and bulk CA/Sulindac film and (b) the enlarge IR spectra, collected over the range from 1800 to 1700 cm^{-1} , corresponding to the COOH stretch.

III-3-2. Molecular mobility of CA/Sulindac nanofibers

In order to investigate the nano-confinement effect on the molecular mobility of CNs, the spin-lattice relaxation time in the rotating frame, $T_{1\rho}$, of CNs was measured using ^1H solid-state NMR. The mechanism for the spin-lattice relaxation of CA is described in Fig. 4. When the magnetic field is applied to ^1H proton, a spin state of the proton is divided into two spin states. The protons in the lower energy state are excited to the upper energy state by applying a pulse corresponding to the energy difference between two spin states. After that, the excited protons are gradually relaxed to the low energy state while transferring the energy from the excited spins to the lattice, which is a rest of assembly of samples from spin. In polymer materials, the molecular motion of chains provides the link for the energy transfer. It was reported that spin-lattice relaxation of cellulose derivatives is induced by the reorientation of the methyl groups at low temperature (approximately below 250 K) and by reptation-like displacement of main chains at high temperatures above 250 K.³⁷⁻³⁸ Therefore, the measurement of $T_{1\rho}$ enables analysis of the molecular mobility of CNs.

The spin-lattice relaxation behaviors of the CNs were fitted to a single-exponential decay model, and the $T_{1\rho}$ value for the single-exponential decay process was obtained using the following equation:

$$M_{\tau} = M_0 \exp\left(\frac{-\tau}{T_{1\rho}}\right) \quad (1)$$

where M_{τ} is the magnetization intensity at the delay time (τ). The M_{τ} decayed exponentially from the initial intensity (M_0) with a time constant of $T_{1\rho}$. As shown in Fig. III-5 (a), the $T_{1\rho}$ values of the CNs exhibited U-shaped curves. To quantitatively evaluate the molecular mobility of CNs, the activation energy for the molecular motion, E_a , was determined. For this, the $T_{1\rho}$ values of the CNs were analyzed based on the Bloembergen–Purcell–Pound (BPP) theory. As per this theory, the spin-lattice relaxation behaviors of CNs can be explained by using the following equation:

$$\frac{1}{T_{1\rho}} = \frac{3}{10} \frac{\gamma^4 \hbar^2}{\langle r \rangle^6} \left[\frac{2.5\tau_c}{1 + \omega_0^2 \tau_c^2} + \frac{\tau_c}{1 + 4\omega_0^2 \tau_c^2} + \frac{1.5\tau_c}{1 + 4\omega_1^2 \tau_c^2} \right] \quad (2)$$

where γ is the magnetogyric ratio of the observed species, \hbar is the reduced Planck's constant, $\langle r \rangle$ is the average intramolecular interdipole distance, ω_0 is the angular frequency, and ω_1 is the spin-lock field frequency. τ_c is the

correlation time, which can be considered the average time required for the motional events. E_a was determined from τ_c by the following equation:

$$\tau_c = \tau_0 \exp\left(\frac{E_a}{RT}\right) \quad (3)$$

where τ_0 is the correlation time at infinite temperature. Rachocki *et al.* reported that the spin-lattice relaxation of cellulose derivatives was influenced by two kinds of molecular motions, which are reorientation of small side groups and reptation-like displacement of main chains, respectively.³⁷⁻³⁸ The motions for small side groups are generally much faster than the main chain motions. At low temperatures below 250 K, the molecular motion of main chains is too slow to induce the spin-lattice relaxation. Thus, the reorientation of small side groups predominantly affects the spin-lattice relaxation, exhibiting E_a of about 3 to 6 eV. When the temperature is higher than 250 K, the molecular motions of side group becomes too fast to induce spin-lattice relaxation. As a result, reptation-like displacement of the main chains could mainly induce the spin-lattice relaxation at above 250 K, exhibiting higher E_a than the side group motion.

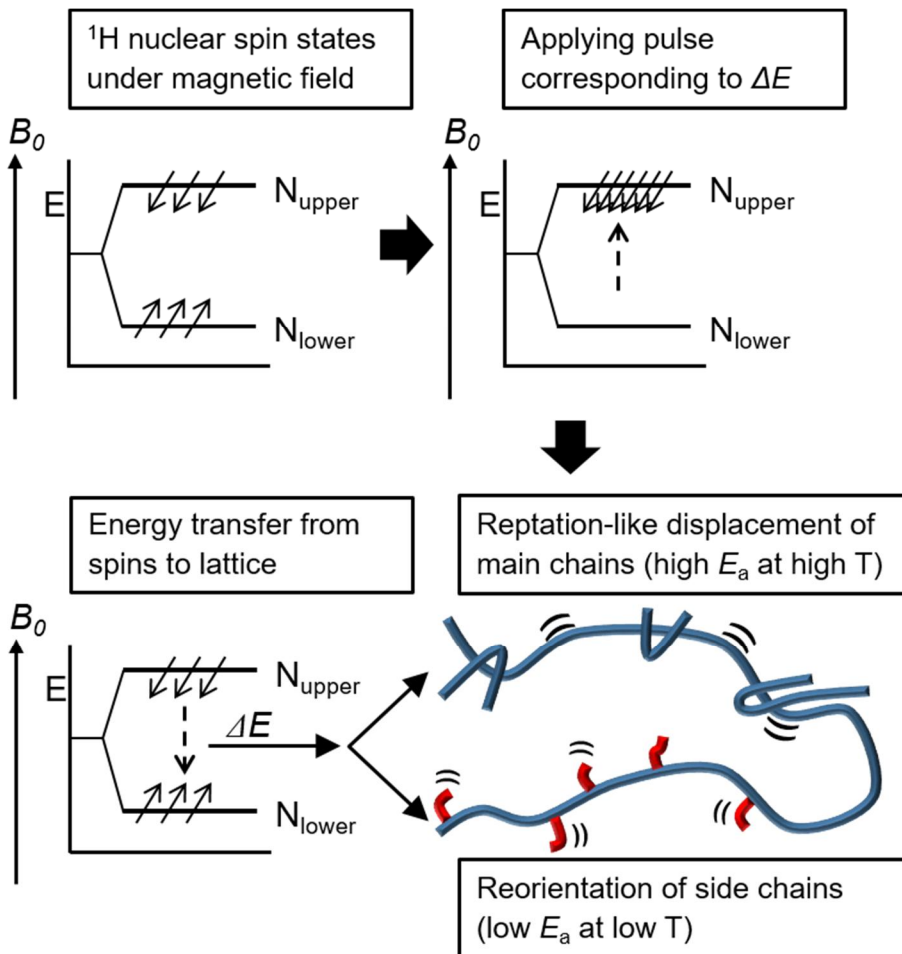


Figure III-4. Schematic description of ^1H spin-lattice relaxation procedure of cellulose derivatives.

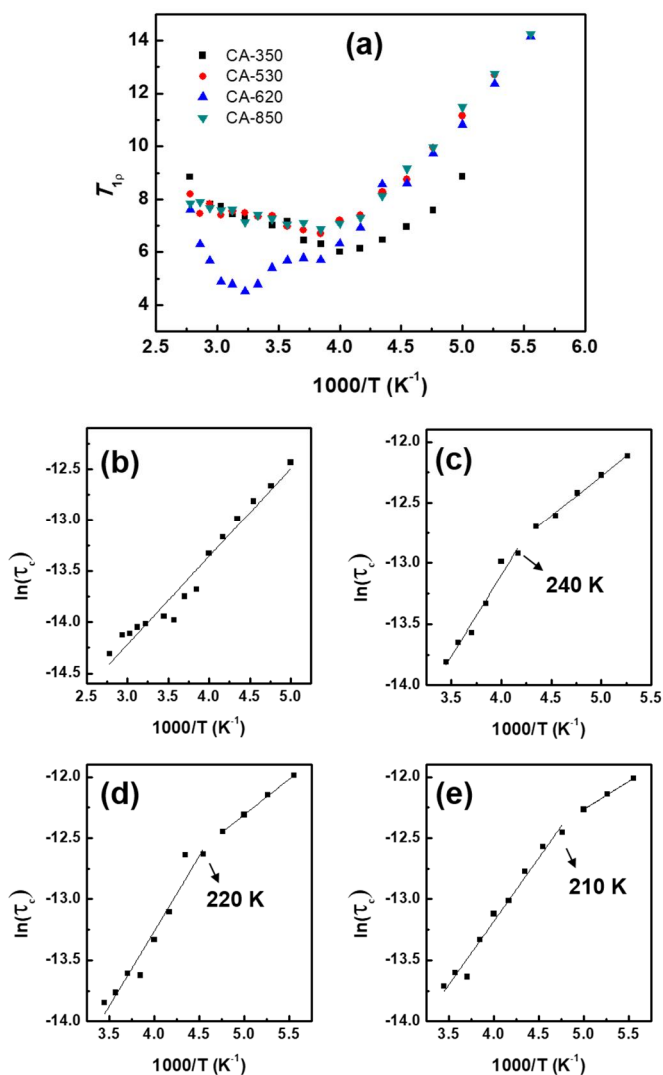


Figure III-5. (a) ^1H $T_{1\rho}$ vs the inverse temperature ($1000/T$) of cellulose acetate/Sulindac nanofibers and logarithmic plot of the correlation time, τ_c , vs the inverse temperature ($1000/T$) of (b) CN-350, (c) CN-530, (d) CN-620 and (e) CN-850.

Table III-2. Activation energy of CNs obtained from correlation time, τ_c .

Sample	$E_{a, \text{side}}$ (kJ/mol)	$E_{a, \text{main}}$ (kJ/mol)
CN-350	7.16	-
CN-530	5.44	11.09
CN-620	4.85	10.21
CN-850	3.83	8.64

Figure III-5 shows the logarithmic plots of τ_c of the CNs as a function of the inverse temperature ($1/T$). CN-350 exhibited a linear plot with no slope change. The E_a of CN-350 was 7.16 eV, corresponding to the E_a for the side chain motion ($E_{a, \text{side}}$). In contrast, the plot for τ_c of CN-530 showed a noticeable change in its slope. The E_a for CN-530 at low temperature (180–230 K) and high temperature (240–320 K) was 5.44 and 11.09 eV, respectively (shown in Fig. III-5 (c) and Table 2). Given that cellulose derivatives commonly exhibit E_a values for side chain motion at low temperature and main chain motion at high temperature, it was presumable that the E_a of 5.44 eV stood for $E_{a, \text{side}}$ and the E_a of 11.09 eV indicated the E_a for main chain motion ($E_{a, \text{main}}$). In addition, the slope of the plots for τ_c of CN-620 and CN-850 also changed, exhibiting both $E_{a, \text{side}}$ and $E_{a, \text{main}}$. Interestingly, the minimum temperature at which main chain motion was observed, T_{min} , increased from 210 to 240 K with decreasing diameter of CNs from 850 to 530 nm. The increased T_{min} implied that the molecular motion of the main chain required more energy to induce spin-lattice relaxation. In other words, the topological constraint between the main chains increased with decreasing diameter of CNs from 850 to 530 nm. In addition, the results that main chain motion was not observed in CN-350 proposed that the main chain motions in CN-350 were more severely confined to each other than the main chains in CN-530, CN-620, and CN-850.

As can be seen from Table III-2, $E_{a, \text{main}}$ increased from 8.64 to 11.09 eV with decreasing diameter of CNs from 850 to 530 nm. The increased $E_{a, \text{main}}$ implied that the molecular mobility for the reptation-like displacement of main chains decreased with a decrease in the diameter of CNs from 850 to 530 nm. Furthermore, the $E_{a, \text{side}}$ increased from 3.83 to 7.16 eV with decreasing diameter of CNs from 850 to 350 nm, suggesting that the motion of the side chains was suppressed with decreasing diameter. The decrease in molecular mobility with decreasing diameter of CNs suggests that the chains confined in thinner nanofibers tend to form a more closely packed structure.

III-3-3. Drug release properties of CA/Sulindac nanofibers and bulk CA/Sulindac film

To investigate the drug release characteristics of CNs and BF, the amount of cumulative release of drug from CNs and BF was measured by the total immersion method. The measurements were carried out in the acetate buffer solution with a pH of 5.5 at 37 °C, simulating the physiological conditions for transdermal drug delivery system. In Fig. III-6 (a), most of the Sulindac in CNs was released within 20 h. In contrast, the Sulindac in BF was slowly released and the cumulative release of Sulindac was 7.5% for 20 h. The much slower release rate of BF might be because the specific surface area of BF is much lower than CNs. It is shown in Fig. III-6 (b) that Sulindac was gradually released from CNs for 4 h. Sulindac was selected as a model drug molecule because release of Sulindac from cellulose acetate could be analyzed based on the simple diffusion model.³⁹ The release kinetics of Sulindac was analyzed using the following equation³⁹⁻⁴¹

$$\frac{M_t}{M_\infty} = kt^n \text{ for } \frac{M_t}{M_\infty} < 0.6 \quad (4)$$

where M_t is the cumulative amount of drugs released at a specific release time

and M_{∞} is the cumulative amount of drugs released at an infinite time, k is the drug release rate, and n is a release exponent. The n characterizes the drug release mechanism for cylindrical shaped matrices. When $n = 0.5$, the drug release mechanism corresponds to a Fickian diffusion mechanism. As shown in Fig. III-6 (c), the amount of cumulative release of Sulindac from CNs increased linearly with $t^{0.5}$, suggesting that the Sulindac release mechanism is fitted to the Fickian diffusion. In the Fickian diffusion model, the total mass flux is proportional to the specific surface area.⁴² However, it is shown in Fig. III-6 (d) that the drug release rate constant, k , of the CNs and the specific area of CNs were not directly correlated with each other. For instance, the CN-350 having the highest specific surface area among the CNs exhibited the smaller k than that of CN-530 and CN-620. These results implied that in addition to the specific surface area, other factors could affect the drug release kinetics.

As can be seen in Fig. III-2 and Fig. III-3, the Sulindac molecules were well dispersed in the amorphous CA matrix while retaining their chemical integrity. In addition, the ^1H solid-state NMR analysis proved that the amorphous chains formed a highly packed structure when the diameter of CNs decreased (see Fig. III-5). These results suggested that the differences in the amorphous chain topology of CNs could cause mismatches between the specific surface area and release rate constant of the CNs. Therefore, the effects of changes in the chain topology on the drug release properties of CNs were analyzed. To

separate the effect of specific surface area on drug release, the drug release rate per unit specific surface area and the E_a for the molecular motions of chains of CNs were compared. In Fig. III-7, the k per specific surface area (K/S) noticeably decreased with an increase in E_a of both the side chain motion and the main chain motion. These results indicate that the depression of the molecular motion of the chains in CNs results in the suppression of drug release.

In addition to the conventional analysis on drug release kinetics based on Fick's second law of diffusion, there have been several attempts to specify the formula on drug release kinetics of polymer nanofibers. Therefore, the drug release kinetics of the CNs was studied by using the specified formula on polymer nanofibers and shown in Fig. III-8. The diffusion coefficient of the drug homogeneously distributed in the fibers is obtained using the following equation⁴³⁻⁴⁴

$$\frac{M_t}{M_\infty} = 4 \left(\frac{Dt}{\pi R^2} \right)^{\frac{1}{2}} - \frac{Dt}{R^2} \quad \text{for} \quad \frac{M_t}{M_\infty} \leq 0.4 \quad (5)$$

where M_t is the cumulative amount of drugs released at a specific release time

and M_{∞} is the cumulative amount of drugs released at an infinite time, D is the diffusion coefficient of the drug, and R is a diameter of the nanofibers. The D values for CN-850 and CN-620 were 80.0 and 85.3 nm^2/min , respectively. The similar D values indicated that the rate of drug release in CA matrix was similar. However, with decreasing diameter from 620 to 350, the D was noticeably decreased. The D values for CN-530 and CN-350 were 47.5, and 20.4 nm^2/min , respectively. These results suggested that drug tended to be slowly diffused with decreasing diameter of CNs from 620 to 350 nm. As can be seen in Figure III-2 and Figure III-3, the Sulindac molecules were well dispersed in the amorphous CA matrix while retaining their chemical integrity. In addition, the ^1H solid-state NMR analysis proved that the amorphous chains formed a highly packed structure when the diameter of CNs decreased (see Figure III-5). Therefore, it could be inferred from the Solid-state NMR results and diffusion coefficients for CNs that the depression of the molecular motion of the chains in CNs results in the slowing of drug release.

The effect of nanoscale confinement on the drug release properties of polymer nanofibers is shown in Fig. III-9. The molecular mobility of amorphous chains decreases with a decrease in the diameter of polymer nanofibers, indicating that the amorphous chains were closely packed. With decreasing molecular mobility of the amorphous chains, the release of drug was severely retarded. These results clearly show that the drug release rate could be

changed significantly with changes in the molecular mobility. Therefore, when designing and developing drug delivery systems based on polymer nanofibers, the confinement effect on the drug release properties should be considered carefully.

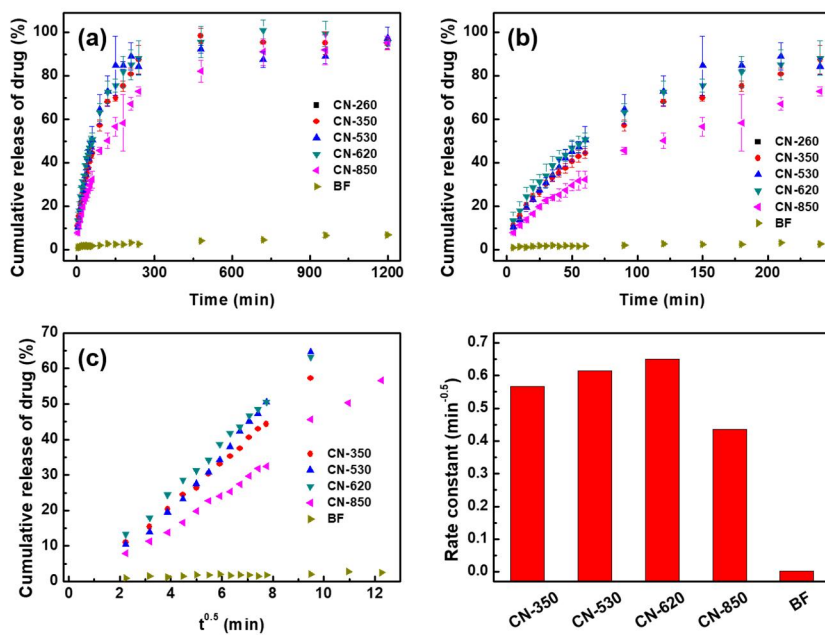


Figure III-6. Cumulative release profiles of Sulindac from CA/Sulindac nanofibers and bulk CA/Sulindac film by total immersion technique during (a) 0–1200 min and (b) 0–240 min, (c) 0–150 min (root time scale) and (d) drug release rate constant of CA/Sulindac nanofibers and bulk CA/Sulindac film.

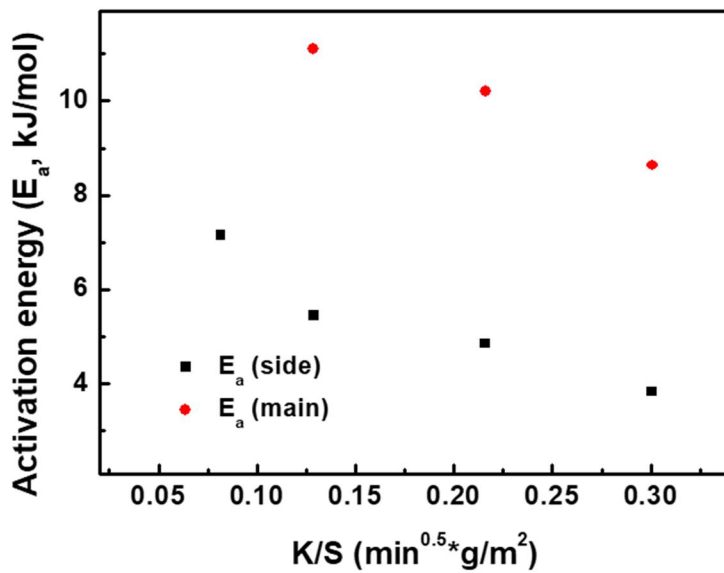


Figure III-7. Activation energy, E_a for side chain motion and main chain motion vs drug release rate constant per specific surface area of CA/Sulindac nanofibers.

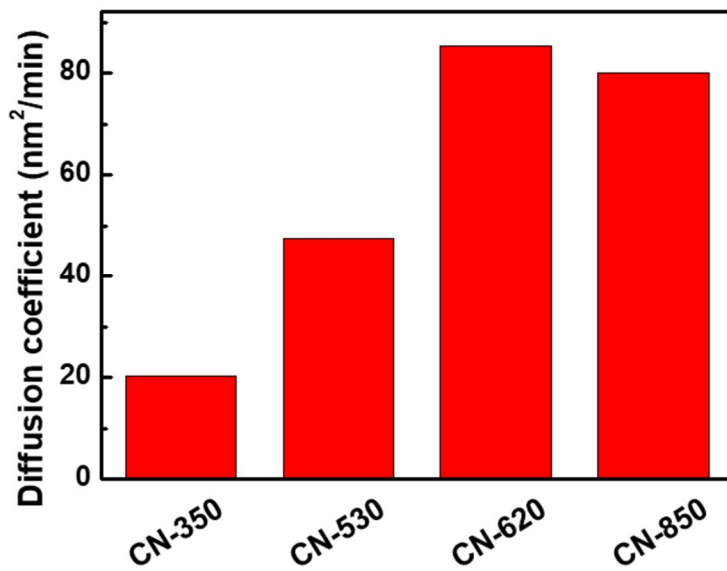


Figure III-8. Diffusion coefficient of CA/Sulindac nanofibers

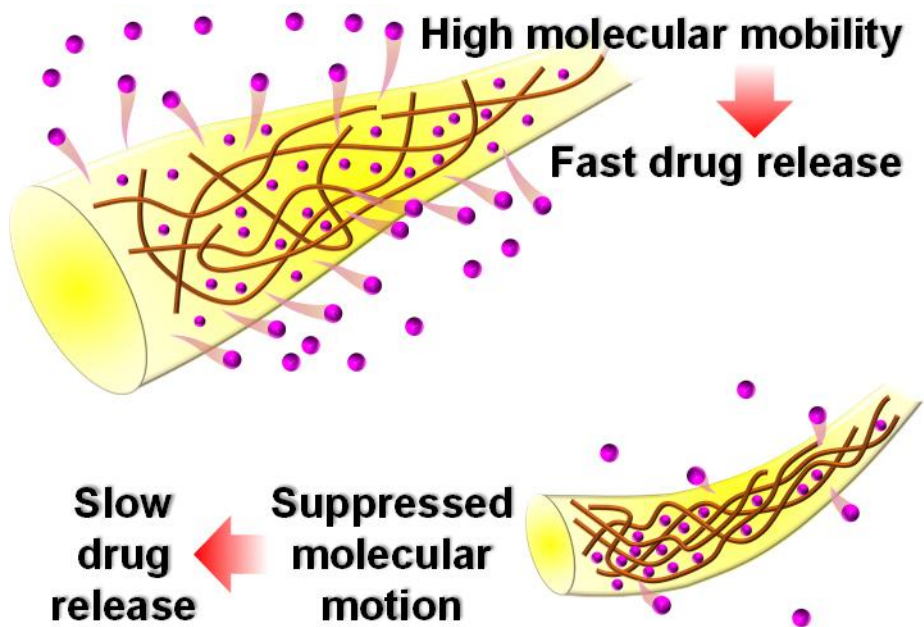


Figure III-9. Proposed effect of confinement on molecular mobility and drug release properties of CA/Sulindac nanofibers.

III-4. Conclusion

In this study, the confinement effect on the drug release properties of cellulose acetate (CA)/Sulindac nanofibers (CNs) was investigated by observing the molecular mobility and the drug release rate of CNs. It was confirmed that CNs had an amorphous structure. Sulindac molecules were successfully incorporated in the amorphous CA matrix while forming hydrogen bonds with the CA chains. ^1H NMR spin-lattice relaxation time measurements revealed that the CN-850—the CNs with the largest diameter— had E_a of 8.64 eV for main chain motion and E_a of 3.83 eV for side chain motion. However, the E_a for both the main chains and side chains increased with decreasing diameter of CNs from 850 to 530 nm, indicating a decrease in the molecular mobility. Furthermore, CN-350 only showed E_a for the side chain motion and that for main chain motion was not observed. The absence of E_a for main chain motion suggested that main chain motions were severely suppressed because the chains became closely packed when the diameter of CNs is smaller than 350 nm. These features clearly show that the CA chains confined in a thinner fiber tended to be packed more closely. Drug release experiments showed that such confinement-induced chain packing of ultrathin CNs noticeably influenced the drug release properties of CNs; the drug release rate per specific surface area significantly decreased with increasing E_a for both main chain motion and side chain motion. In addition, the diffusion coefficient of

drug was significantly decreased with decreasing diameter of CNs from 620 to 350 nm. Therefore, the correlation between the confinement effect and the drug release properties of polymer nanofibers should be necessarily taken into account for the prevention of the side effect connected to dosing and improvement of drug effectiveness.

References and Notes

1. Francis, M. F.; Cristea, M.; Winnik, F. M., Polymeric micelles for oral drug delivery: why and how. *Pure and Applied Chemistry* **2004**, *76* (7-8), 1321-1335.
2. Mrsny, R. J., Oral drug delivery research in Europe. *J Control Release* **2012**, *161* (2), 247-53.
3. Khan, A. D.; Bajpai, M., Floating drug delivery system: An overview. *International Journal of PharmTech Research* **2010**, *2* (4), 2497-2505.
4. Zhang, Y.; Zhang, H.; Che, E.; Zhang, L.; Han, J.; Yang, Y.; Wang, S.; Zhang, M.; Gao, C., Development of novel mesoporous nanomatrix-supported lipid bilayers for oral sustained delivery of the water-insoluble drug, lovastatin. *Colloids Surf B Biointerfaces* **2015**, *128*, 77-85.
5. Mandal, U. K.; Chatterjee, B.; Senjoti, F. G., Gastro-retentive drug delivery systems and their in vivo success: A recent update. *Asian Journal of Pharmaceutical Sciences* **2016**, *11* (5), 575-584.
6. Jannat, S.; Masum, A.; Sharmin, F.; Islam, A.; Reza, S., Formulation and evaluation of sustained release matrix type transdermal film of ibuprofen. *Bangladesh Pharmaceutical Journal* **2012**, *15* (1), 17-21.

7. Kumar, P. D.; Rathnam, G.; Prakash, C.; Saravanan, G.; Karthick, V.; Selvam, T. P., Formulation and characterization of bilayer floating tablets of ranitidine. *Rasayan J chem* **2010**, *3* (2), 368-74.
8. Tadros, M. I., Controlled-release effervescent floating matrix tablets of ciprofloxacin hydrochloride: development, optimization and in vitro-in vivo evaluation in healthy human volunteers. *Eur J Pharm Biopharm* **2010**, *74* (2), 332-9.
9. Teo, A. L.; Shearwood, C.; Ng, K. C.; Lu, J.; Moochhala, S., Transdermal microneedles for drug delivery applications. *Materials Science and Engineering: B* **2006**, *132* (1-2), 151-154.
10. Wang, Z.; Itoh, Y.; Hosaka, Y.; Kobayashi, I.; Nakano, Y.; Maeda, I.; Umeda, F.; Yamakawa, J.; Kawase, M.; Yag, K., Novel transdermal drug delivery system with polyhydroxyalkanoate and starburst polyamidoamine dendrimer. *Journal of Bioscience and Bioengineering* **2003**, *95* (5), 541-543.
11. Henry, S.; McAllister, D. V.; Allen, M. G.; Prausnitz, M. R. In *Micromachined needles for the transdermal delivery of drugs*, Proceedings MEMS 98. IEEE. Eleventh Annual International Workshop on Micro Electro Mechanical Systems. An Investigation of Micro Structures, Sensors, Actuators, Machines and Systems (Cat. No.98CH36176, 25-29 Jan 1998; 1998; pp 494-498.

12. Ashraf, M. W.; Tayyaba, S.; Afzulpurkar, N.; Nisar, A., Fabrication and Analysis of Tapered Tip Silicon Microneedles for MEMS based Drug Delivery System. *Sensors & Transducers* **2010**, *122* (11), 158-172.
13. Sung, W.-s.; Oh, S.-y., Electroosmotic flow through skin: effect of current duration and poly(ethylene imine). *Journal of Pharmaceutical Investigation* **2017**.
14. Matteucci, M.; Casella, M.; Bedoni, M.; Donetti, E.; Fanetti, M.; De Angelis, F.; Gramatica, F.; Di Fabrizio, E., A compact and disposable transdermal drug delivery system. *Microelectronic Engineering* **2008**, *85* (5-6), 1066-1073.
15. Mouthuy, P. A.; Somogyi Skoc, M.; Cipak Gasparovic, A.; Milkovic, L.; Carr, A. J.; Zarkovic, N., Investigating the use of curcumin-loaded electrospun filaments for soft tissue repair applications. *Int J Nanomedicine* **2017**, *12*, 3977-3991.
16. Charensriwilaiwat, N.; Opanasopit, P.; Rojanarata, T.; Ngawhirunpat, T.; Supaphol, P., Preparation and characterization of chitosan-hydroxybenzotriazole/polyvinyl alcohol blend nanofibers by the electrospinning technique. *Carbohydrate Polymers* **2010**, *81* (3), 675-680.
17. Yao, J.; Bastiaansen, C.; Peijs, T., High Strength and High Modulus Electrospun Nanofibers. *Fibers* **2014**, *2* (4), 158-186.

18. Xu, C., Aligned biodegradable nanofibrous structure: a potential scaffold for blood vessel engineering. *Biomaterials* **2004**, *25* (5), 877-886.
19. Yu, D. G.; Yu, J. H.; Chen, L.; Williams, G. R.; Wang, X., Modified coaxial electrospinning for the preparation of high-quality ketoprofen-loaded cellulose acetate nanofibers. *Carbohydr Polym* **2012**, *90* (2), 1016-23.
20. Sebe, I.; Szabo, P.; Kallai-Szabo, B.; Zelko, R., Incorporating small molecules or biologics into nanofibers for optimized drug release: A review. *Int J Pharm* **2015**, *494* (1), 516-30.
21. Suwantong, O.; Opanasopit, P.; Ruktanonchai, U.; Supaphol, P., Electrospun cellulose acetate fiber mats containing curcumin and release characteristic of the herbal substance. *Polymer* **2007**, *48* (26), 7546-7557.
22. Hu, X.; Liu, S.; Zhou, G.; Huang, Y.; Xie, Z.; Jing, X., Electrospinning of polymeric nanofibers for drug delivery applications. *J Control Release* **2014**, *185*, 12-21.
23. Abrigo, M.; McArthur, S. L.; Kingshott, P., Electrospun nanofibers as dressings for chronic wound care: advances, challenges, and future prospects. *Macromol Biosci* **2014**, *14* (6), 772-92.
24. Kim, M. S.; Shin, Y. M.; Lee, J. H.; Kim, S. I.; Nam, Y. S.; Shin, C. S.; Shin, H., Release kinetics and in vitro bioactivity of basic fibroblast

- growth factor: effect of the thickness of fibrous matrices. *Macromol Biosci* **2011**, *11* (1), 122-30.
25. Wadhwa, S.; Paliwal, R.; Paliwal, S. R.; Vyas, S. P., Nanocarriers in Ocular Drug Delivery: An Update Review. *Current Pharmaceutical Design* **2009**, *15* (23), 2724-2750.
 26. Dash, S.; Murthy, P. N.; Nath, L.; Chowdhury, P., Kinetic modeling on drug release from controlled drug delivery systems. *Acta poloniae pharmaceutica* **2010**, *67* (3), 217-23.
 27. Lee, S. S.; Hughes, P.; Ross, A. D.; Robinson, M. R., Biodegradable implants for sustained drug release in the eye. *Pharm Res* **2010**, *27* (10), 2043-53.
 28. Hrib, J.; Sirc, J.; Hobzova, R.; Hampejsova, Z.; Bosakova, Z.; Munzarova, M.; Michalek, J., Nanofibers for drug delivery - incorporation and release of model molecules, influence of molecular weight and polymer structure. *Beilstein J Nanotechnol* **2015**, *6*, 1939-45.
 29. Thakkar, S.; Misra, M., Electrospun polymeric nanofibers: New horizons in drug delivery. *Eur J Pharm Sci* **2017**, *107*, 148-167.
 30. Chou, S. F.; Woodrow, K. A., Relationships between mechanical properties and drug release from electrospun fibers of PCL and PLGA blends. *J Mech Behav Biomed Mater* **2017**, *65*, 724-733.

31. Chou, S. F.; Carson, D.; Woodrow, K. A., Current strategies for sustaining drug release from electrospun nanofibers. *J Control Release* **2015**, *220* (Pt B), 584-91.
32. Chung, J.; Chung, J. W.; Priestley, R. D.; Kwak, S.-Y., Confinement-Induced Change in Chain Topology of Ultrathin Polymer Fibers. *Macromolecules* **2018**, *51* (11), 4229-4237.
33. Taepaiboon, P.; Rungsardthong, U.; Supaphol, P., Vitamin-loaded electrospun cellulose acetate nanofiber mats as transdermal and dermal therapeutic agents of vitamin A acid and vitamin E. *Eur J Pharm Biopharm* **2007**, *67* (2), 387-97.
34. Tungprapa, S.; Jangchud, I.; Supaphol, P., Release characteristics of four model drugs from drug-loaded electrospun cellulose acetate fiber mats. *Polymer* **2007**, *48* (17), 5030-5041.
35. Gopiraman, M.; Fujimori, K.; Zeeshan, K.; Kim, B. S.; Kim, I. S., Structural and mechanical properties of cellulose acetate/graphene hybrid nanofibers: Spectroscopic investigations. *Express Polymer Letters* **2013**, *7* (6), 554-563.
36. Li, M.; Kim, I.-H.; Jeong, Y. G., Cellulose acetate/multiwalled carbon nanotube nanocomposites with improved mechanical, thermal, and electrical properties. *Journal of Applied Polymer Science* **2010**, n/a-n/a.

37. Rachocki, A.; Tritt-Goc, J.; Pislewski, N., NMR study of molecular dynamics in selected hydrophilic polymers. *Solid State Nucl Magn Reson* **2004**, *25* (1-3), 42-6.
38. Rachocki, A.; Kowalczyk, J.; Tritt-Goc, J., How we can interpret the T1 dispersion of MC, HPMC and HPC polymers above glass temperature? *Solid State Nucl Magn Reson* **2006**, *30* (3-4), 192-7.
39. Ritger, P. L.; Peppas, N. A., A simple equation for description of solute release I. Fickian and non-fickian release from non-swellable devices in the form of slabs, spheres, cylinders or discs. *Journal of Controlled Release* **1987**, *5* (1), 23-36.
40. Peppas, N. A.; Khare, A. R., Preparation, structure and diffusional behavior of hydrogels in controlled release. *Advanced Drug Delivery Reviews* **1993**, *11* (1-2), 1-35.
41. Dash, S.; Murthy, P. N.; Nath, L.; Chowdhury, P., Kinetic modeling on drug release from controlled drug delivery systems. *Acta Poloniae Pharmaceutica - Drug Research* **2010**, *67* (3), 217-223.
42. Socolofsky, S. A.; Jirka, G. H., Environmental Fluid Mechanics Part I: Mass Transfer and Diffusion. *Engineering Lectures* **2002**, *2*.
43. Siepmann, J.; Siepmann, F., Modeling of diffusion controlled drug delivery. *J Control Release* **2012**, *161* (2), 351-62.

44. Petlin, D. G.; Amarah, A. A.; Tverdokhlebov, S. I.; Anissimov, Y. G.,
A fiber distribution model for predicting drug release rates. *J Control
Release* **2017**, *258*, 218-225.

CHAPTER IV

Solvent-Assisted Crystallization of *Meta*-Aramid Nanofibers

IV-1. Introduction

Poly(m-phenyleneterephthalamide), *meta*-aramid, is an aromatic polyamide possessing superior chemical stability, mechanical strength, and thermal resistance because of its rigid backbone structure and a large number of hydrogen bonds.¹⁻³ Therefore, *meta*-aramid fibers are used in various applications such as flame-resistant barriers, protective apparel, electrical insulation, and high-temperature filter materials.⁴⁻⁶ In addition to the bulk *meta*-aramid fibers, the commercial nanofibrous *meta*-aramid is currently used for protective clothing to improve its smoke shielding properties.⁷ The nanofibrous *meta*-aramid has also received much attention recently in relation to environmental issues such as water and air purification due to its high hydrophilicity and excellent adsorption performance. Among the various types of nanofibrous polymer, electrospun polymer nanofibers are well suited for the protective clothing and environmental applications because of their

high porosity, large specific surface area, small pore size, and ease of manufacture.⁸⁻¹³

Several studies have demonstrated that electrospun *meta*-aramid nanofiber (*mANF*) mats are useful as a membrane for water purification, air filtration and flame retardants, *etc.*¹⁴⁻²¹ However, as-spun *mANF* mats typically have low crystallinity, because the rigid chains are difficult to align and form a crystalline structure during electrospinning. Therefore, the as-spun *mANF* mats have shown a low elastic modulus and a poor chemical resistance to polar solvents such as DMF, DMAc and DMSO. Although the low crystallinity of *mANF* is a major constraint to its practical usage, only few studies have discussed methods for the regeneration of the crystal structure of *mANF*. Yao *et al.* reported that crystallization did not occur even after annealing *mANFs* at 150, 200, and 250 °C for 2 days.²² Oh *et al.* exposed an *mANF* mat to microwaves at approximately 80 °C after wetting the mat in water.²³ The mat was successfully crystallized by the microwave treatment, due to which the tensile strength of the mat was 2.8 times higher than that of the original. However, the chemical stability of the *mANF* mat was not confirmed. Furthermore, a large amount of energy was required to apply microwaves continuously over a large area of a nanofiber mat under well-controlled temperatures. It was reported that *mANF* crystallized under heat treatment at 300 °C for 10 min after removing salts in *mANF* by washing with

water.²⁴ The regeneration of the crystal structure resulted in enhanced chemical stability and mechanical strength. However, heat treatment at high temperature is unsuitable for practical applications. High-temperature heat treatment requires high energy consumption, and causes undesirable changes such as decomposition and carbonization of the nanofibers. Furthermore, on the surface of nanofiber mat directly exposed to the heat, the nanofibers deform very rapidly, and this deformation is very difficult to control. Therefore, it is necessary to develop a more efficient and practical method for the crystallization of *m*ANF.

As a facile method for crystallizing the rigid chains in nanofibers, solvent-based treatment has been frequently employed. For instance, electrospun silk and syndiotactic polystyrene nanofibers were successfully crystallized in chambers filled with saturated solvent vapor.²⁵⁻²⁷ Plasticization of the local chains occurs when the solvent vapor molecules permeate into the nanofiber matrix, inducing the crystallization of nanofibers. In addition to vapor treatment, crystallization of nanofibers has also been conducted in a wet condition. Ahn *et al.* reported that glucose polymer chains were crystallized when ionic liquid was extracted from cellulose nanofibers to the coagulant.²⁸ The crystallinity of cellulose nanofibers increased as the extraction of ionic liquid became slower, because the slower extraction, the more time for crystallization. Kim *et al.* also suggested that poly(3,4-

ethylenedioxythiophene) (PEDOT) chains could be stabilized in highly concentrated H₂SO₄ solution, and a crystalline PEDOT nanofibril structure could be formed by rinsing the H₂SO₄ solution in water.²⁹ Although these studies have proved that solvent-based treatment is useful for the crystallization of nanofibers, there have been no studies yet on the crystallization of *m*ANF via solvent-based treatment.

In this study, solvent-assisted heat treatment was used for the crystallization of *m*ANF. N,N-dimethylacetamide was used as a solvent for the as-spun *m*ANF, whereas ethylene glycol and water were used as non-solvents. After wetting the as-spun *m*ANF in the co-solvent, the solvent molecules were extracted by low-temperature heat treatment. To control the solvent extraction rate, the heat treatment temperature was adjusted (90, 120, and 150 °C). It was found that *m*ANF mat treated in the optimized solvent-assisted heat treatment condition exhibits high crystallinity. The high crystallinity resulted in excellent chemical stability. To the best of our knowledge, this is the first report which elucidates the mechanisms for the crystallization of *m*ANF via solvent-assisted heat treatment. The facile and cost-effective crystallization process could significantly contribute to the application of *m*ANF to various industrial fields ranging from water purification technology to high-temperature air filtration systems. After developing the crystallization process, the effect of size on crystallization process was discussed. It was revealed that degree of

crystallization of *m*ANFs gets lower when diameter of *m*ANFs gets smaller.

IV-2. Experimental Section

IV-2-1. Materials

Poly(*meta*-phenylene isophthalamide) (*meta*-aramid, Nomex®) fiber was purchased from DuPont Plant. Ethylene glycol (EG, anhydrous, 99.8%) and lithium chloride (LiCl, ACS reagent, ≥99%) were purchased from Sigma-Aldrich. *N,N*-Dimethylacetamide (DMAc, ≥99.5%) was purchased from Daejung Chemical & Metals Co. All materials were used as received without further purification. The LiCl and *meta*-aramid were dried at 80 °C for 24 h in a vacuum oven to remove the moisture. Highly deionized water (18 MΩ cm⁻¹) was used throughout the experiments.

IV-2-2. Fabrication of *meta*-aramid nanofibers

The electrospinning solution was prepared by dissolving *meta*-aramid fibers and LiCl in DMAc at 50 °C for 24 h in an oven shaker. The concentration of *meta*-aramid was 12, 14, and 16 w/v%. The *meta*-aramid/LiCl ratio was 5:2 by mass. *Meta*-aramid nanofibers were prepared using an electrospinning apparatus (NanoNC, Korea). The device was composed of syringe pumps, a high DC-voltage supply, and a rotating drum-type collector. The *meta*-aramid

solution was placed in a 10-mL syringe equipped with a steel needle with an internal diameter of 0.33 mm. The collector was covered by aluminum foil and placed 15 cm away from the needle tip. A positive voltage of +15 to 20 kV was applied to the tip of the syringe needle and a negative voltage of -10 kV was applied to the collector. The rotating speed of the collector was 100 RPM and the flow rate of the solution was 0.2 mL/h. The temperature and relative humidity in the electrospinning apparatus were maintained in the ranges 20 to 25 °C and 40 to 50%, respectively. Electrospinning was conducted using four syringes for 12 h. The as-spun *meta*-aramid nanofibers were denoted as *mANF*-As.

IV-2-3. Crystallization of *meta*-aramid nanofibers

A co-solvent was prepared by mixing DMAc and EG in deionized water. The volume ratio of water to EG and DMAc was 100:5:x with x varying from 0 to 12. The *mANF* mats were fixed to a square-shaped stainless steel frame and immersed in the co-solvent for 30 min. After the immersion, the *mANF* mats were heat-treated in air for 30 min at 90, 120, and 150 °C, respectively. The *mANF* mats were washed with deionized water and dried in a vacuum oven at 50 °C for 24 h. The *mANF* mats obtained via solvent-assisted heat treatment were denoted as *mANF*-x-y where x indicates the volume percentage of

DMAc versus water and y refers to the heat treatment temperature. A control group was prepared for comparison purposes by applying the high-temperature process reported in the previous study to the $mANF-As$ ²⁴. The $mANF-As$ were washed with deionized water for 30 min and heat-treated at 300 °C in air for 10 min. The $mANF$ subjected to high-temperature treatment is denoted as $mANF-HT$.

IV-2-4. Characterization of *meta*-aramid nanofibers

The microstructure of the $mANFs$ was observed by field emission scanning electron microscopy (FE-SEM, JSM-6700F) at an accelerating voltage of 10 kV. The diameter of $mANFs$ was measured using image analysis software (EyeViewAnalyzer, Digiplus Inc.). The average diameter was determined by measuring the diameter of 100 nanofibers from the FE-SEM images at random. The crystal structure was analyzed using X-ray diffraction methods (XRD, New D8 Advance) over the 2θ range of 10-40° using Cu K_{α} radiation as the X-ray source ($\lambda = 0.154$ nm). Crystallinity of $mANFs$ was obtained using software package (Diffraction.Suite EVA, Bruker). The chemical structure was observed using attenuated total reflection Fourier transform infrared spectroscopy (ATR FT-IR, Nicolet iS5) at room temperature over the range of 4000–650 cm^{-1} . The thermal properties were studied by thermal

gravimetric analysis (TGA, Discovery TGA) and differential scanning calorimetry (DSC, Discovery DSC). The TGA analysis was conducted under a nitrogen condition, and the temperature range for the TGA analysis was 25–700 °C and the heating rate was 10 °C/min. DSC analysis was conducted under a nitrogen condition in the temperature range 25–350 °C. The DSC analysis was carried out in the order of first heating-first cooling-second heating. The heating rate and cooling rate were 10 °C/min. The chemical stability of *m*ANFs was evaluated by soaking the *m*ANF mat in DMAc. The relative weight of the *m*ANF mat was measured by weighing the mat after a specified immersion period (12, 24, 36, and 48 h).

IV-3. Results and Discussion

IV-3-1. Morphology and crystal structure of *meta*-aramid nanofibers

The morphology and diameter of *mANF*-As were observed by FE-SEM. As shown in Fig. IV-1 and table IV-1, three nanofiber mats with fibers of three different average diameters (120, 170, and 270 nm) were successfully fabricated. The nanofibers tended to be aligned in the rotation direction of the collector. In addition, the nanofibers were gathered into larger bundles. The alignment of the nanofibers and formation of bundles might be due to the high LiCl concentration of the polymer solution. The high conductivity of the solution, which is a result of its high salt concentration, causes the spinning solution to move directly to the collector and form bundles, rather than being scattered and forming randomly spread nanofibers. The optimal crystallization conditions were determined by first using *mANF*-As fibers with an average diameter of 170 nm. After optimizing the crystallization conditions, the nanofiber mats with three different diameters were subjected to the optimized conditions.

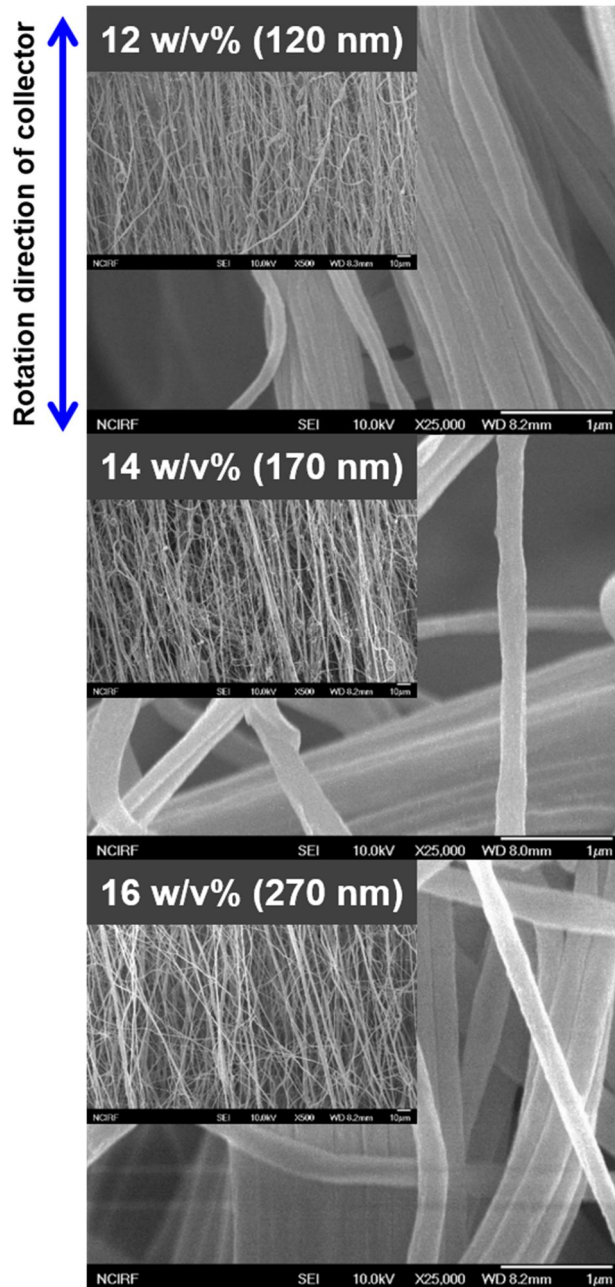


Figure IV-1. FE-SEM images of the as-spun *meta*-aramid nanofibers with different diameters.

Table IV-1. Physical properties of the *meta*-aramid nanofiber solutions and average fiber diameter of the as-spun *meta*-aramid nanofibers.

Meta-aramid concentration (w/v%)	12	14	16
LiCl concentration (w/v%)	4.8	5.6	6.4
Average fiber diameter (μm)	0.12 ± 0.04	0.17 ± 0.03	0.27 ± 0.06

The crystal structure of the *m*ANFs was determined by performing XRD analysis. In general, the XRD pattern of *meta*-aramid exhibits three peaks for the (100), (200), and (211) planes of the crystalline phase, respectively.³⁰⁻³² As shown in Fig. IV-2, the XRD pattern of *m*ANF-As exhibited a broad peak at 24° representing the disordered amorphous structure, without showing the diffraction peaks for the *meta*-aramid crystals. This result indicates that *meta*-aramid chains dissolved in DMAc/LiCl solution were not able to form a crystalline phase during the formation of nanofibers. In contrast, weak diffraction peaks were observed on the XRD pattern for *m*ANF-HT, suggesting the partial formation of a crystal structure as a result of heat treatment at 300 °C. In the case of the *m*ANFs subjected to solvent-assisted heat treatment, the diffraction peaks were not observed when the concentration of DMAc in the co-solvent (DMAc/water, v/v%) was lower than 4%. However, clear XRD peaks attributed to the crystalline phase of *meta*-aramid appeared when the DMAc concentration was 6 and 8%. Particularly, the intensity of the diffraction peaks noticeably increased as the DMAc concentration increased from 4 to 8%. The application of heat treatment ranging from 90 to 150 °C after treatment with the co-solvent caused most of the water molecules in the co-solvent to immediately evaporate; thus, crystallization of the *m*ANFs would mainly be determined by DMAc and EG. The amorphous *meta*-aramid nanofiber mat can be dissolved in DMAc solvent, in other words, DMAc molecules would enable the *meta*-

aramid chains to become mobile, allowing them to easily rearrange. In contrast, the amorphous *meta*-aramid chains are not soluble in EG. Therefore, the presence of EG molecules could prevent the crystallization of the chains when the concentration of DMAc is relatively low. An increasing DMAc concentration leads to an increase in the proportion of DMAc penetrating the *meta*-aramid, which might enhance the crystallinity of the nanofibers. Meanwhile, the *m*ANF mats were torn during the heat treatment when the co-solvents with a high DMAc concentration (10 and 12%) were used (figure not shown). This result suggests that amorphous *meta*-aramid nanofibers are dissociated when a co-solvent with an excessive amount of DMAc is used.

In addition to the DMAc concentration, the heat treatment temperature noticeably affected the crystallization of *m*ANF. As shown in Fig. IV-2, the nanofibers crystallized most efficiently at a temperature of 120 °C, rather than at 90 or 150 °C. Generally, amorphous chains dissolved in a solvent could be rearranged and form crystals during the vaporization of the solvent. Given that the boiling point of DMAc is approximately 165 °C, the DMAc molecules immersed in the nanofiber matrix might have very slowly evaporated during the heat treatment at 90 °C. Therefore, crystallization only partially occurred in those parts of the nanofiber mat from which DMAc evaporated during the heat treatment. In contrast, during heat treatment at 150 °C, most of the DMAc molecules would vaporize in a short time. Although most of the

DMAc molecules had vaporized, the rigid *meta*-aramid chains might not have had sufficient time to crystallize at the fast solvent extraction rate.²⁸ Therefore, it could be inferred from the XRD results that efficient crystallization of the *m*ANFs would occur when most DMAc molecules are allowed to slowly evaporate in a limited heat treatment time. Thus, because the evaporation rate of DMAc was relatively slow and the evaporation of DMAc sufficiently occurred within 30 minutes at 120 °C, the crystallization of *m*ANFs was effective at this temperature. The mechanism underlying the crystallization of *m*ANFs is presented in Fig. IV-3.

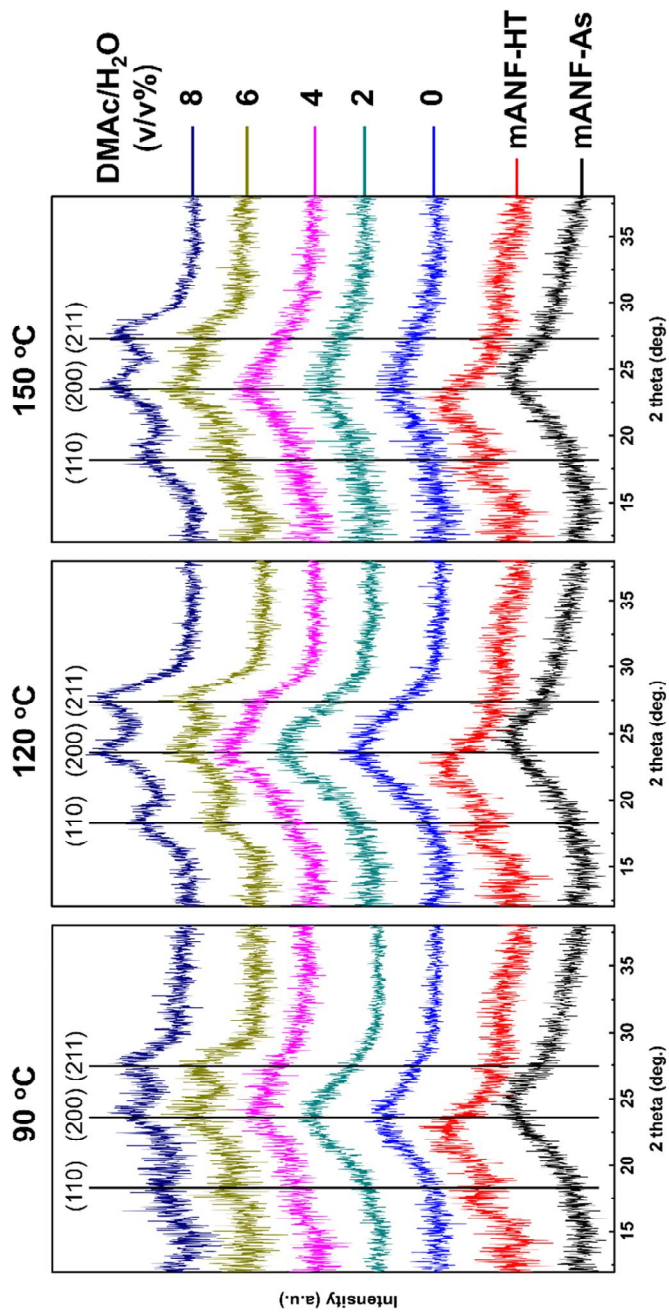


Figure IV-2. WAXRD patterns of *meta*-aramid nanofibers.

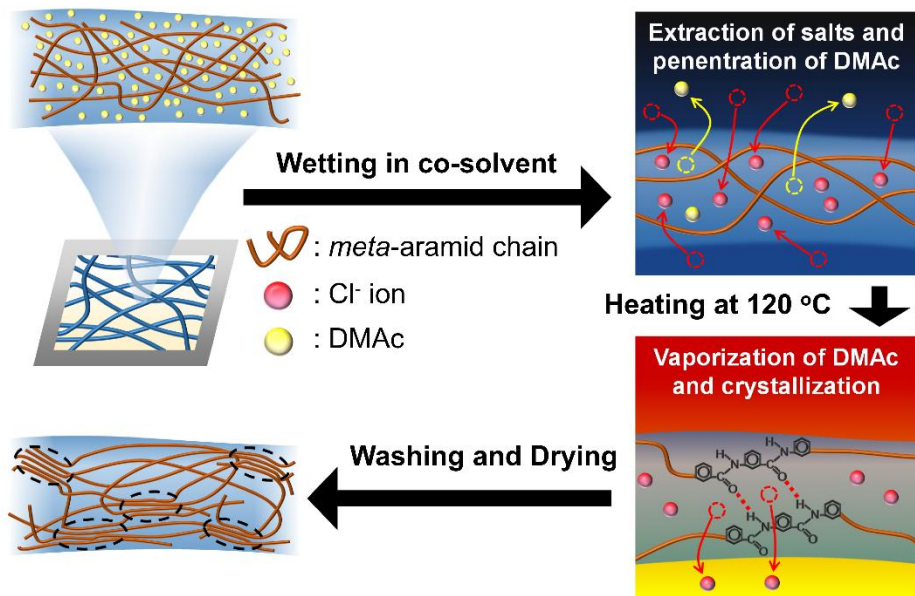


Figure IV-3. Schematic illustration of the crystallization mechanism of *meta*-Aramid nanofibers during the optimized heat-assisted heat treatment.

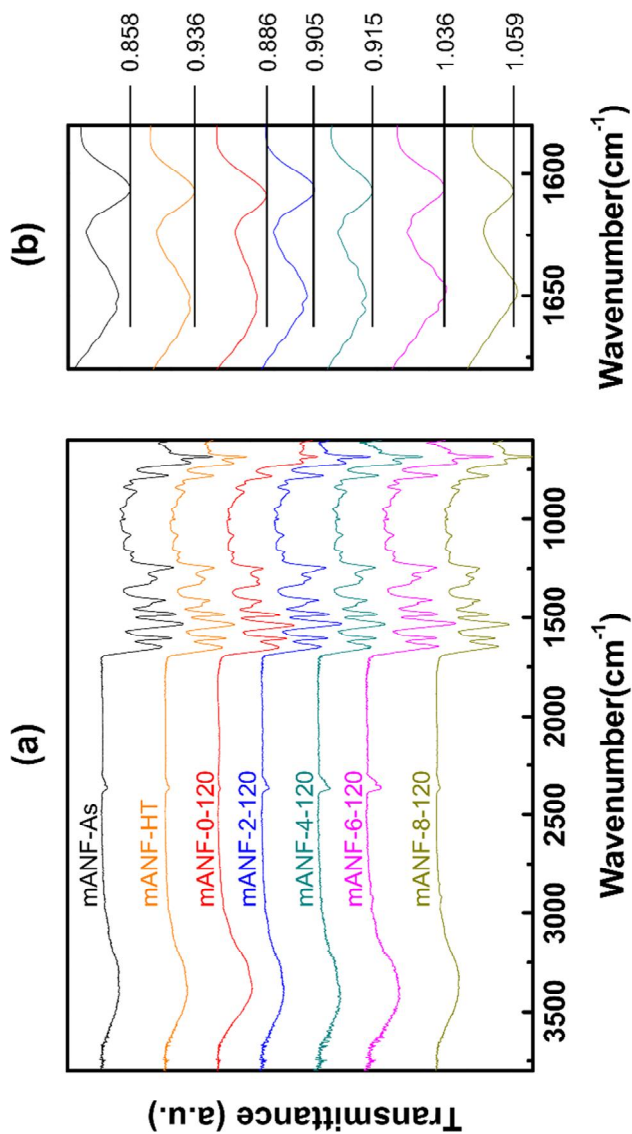


Figure IV-4. ATR FT-IR spectra of *mANF-As*, *mANF-HT*, *mANF-0-120*, *mANF-2-120*, *mANF-4-120*, *mANF-6-120* and *mANF-8-120*. The numbers at (b) are the peak intensity ratio of the C=O...H stretching band (amide I, ~1647 cm⁻¹) and the vibration of the aromatic C-C or C=C bonding (~1604 cm⁻¹)

1).

The crystallization of *m*ANFs was further observed by recording their ATR FT-IR spectra. As shown in Fig. IV-4 (a), all the *m*ANFs exhibited the peaks commonly observed for *meta*-aramid, which are N-H stretching at 3307 cm^{-1} , aromatic C-H stretching at 3068 cm^{-1} , C=O \cdots H stretching at 1647 cm^{-1} , aromatic C-C or C=C vibration at 1604 cm^{-1} , N-H bending at 1528 cm^{-1} , and C-N vibration at 1243 cm^{-1} .³³ Since hydrogen bonds are more densely formed in the crystalline region than in the amorphous region of the *meta*-aramid, the peak intensity at 1647 cm^{-1} for C=O \cdots H stretching tends to increase with an increasing degree of crystallinity. On the other hand, the peak intensity of the aromatic C-C or C=C vibration at 1604 cm^{-1} is almost constant because the aromatic rings are stable and are rarely decomposed during electrospinning and during the application of post-treatment. The peak intensity ratios of the peaks at 1604 and 1647 cm^{-1} of *m*ANFs is shown in Fig. IV-4 (b). The peak intensity ratio of *m*ANF-HT (0.936) is higher than that of *m*ANF-As (0.858), indicating that hydrogen bonding was more pronounced in *m*ANF-HT than in *m*ANF-As, due to the regeneration of the crystal structure during heat treatment at 300 °C. In addition, the peak intensity ratio of *m*ANFs with solvent-assisted heat treatment increased with increasing DMAc concentration. The peak intensity ratio slightly increased with increasing DMAc concentration from 0 to 4%. A further increase in the DMAc concentration

increased the peak intensity ratios of *mANF*-6-120 and *mANF*-8-120 relative to those of *mANF*-HT even further, suggesting that solvent-assisted heat treatment is an effective method for the crystallization of *meta*-aramid chains. The ATR FT-IR results are in good agreement with the XRD results shown in Fig. IV-2.

The changes in the microstructure of the *mANFs* after the solvent-assisted heat treatment were investigated by observing the FE-SEM images. As shown in Fig. IV-5, the shapes of the nanofibers were preserved after the solvent-assisted heat treatment when the DMAc concentration ranged from 0 to 6%. The surface of *mANF*-8-120 was observed to have a rough texture. The chains started loosening when the *mANF* mat was immersed in the co-solvent with high DMAc concentration. *mANFs* composed of loose chains would be difficult to retain their fiber-shaped structure during crystallization.

Although the crystallinity of *mANF*-8-120 was higher than that of *mANF*-6-120, *mANF*-8-120 was too brittle to be handled because of its high crystallinity. From a practical point of view, usefulness of nanofiber mats with excessive brittleness would be limited. Contrary to this, the flexibility of *mANF*-6-120 was sufficient to permit easy handling. In addition, *mANF*-6-120 exhibited high crystallinity comparing to that of *mANF*-HT (see Fig. IV-2 and Fig. IV-4). Therefore, *mANF*-6-120 was selected as the sample with optimal properties.

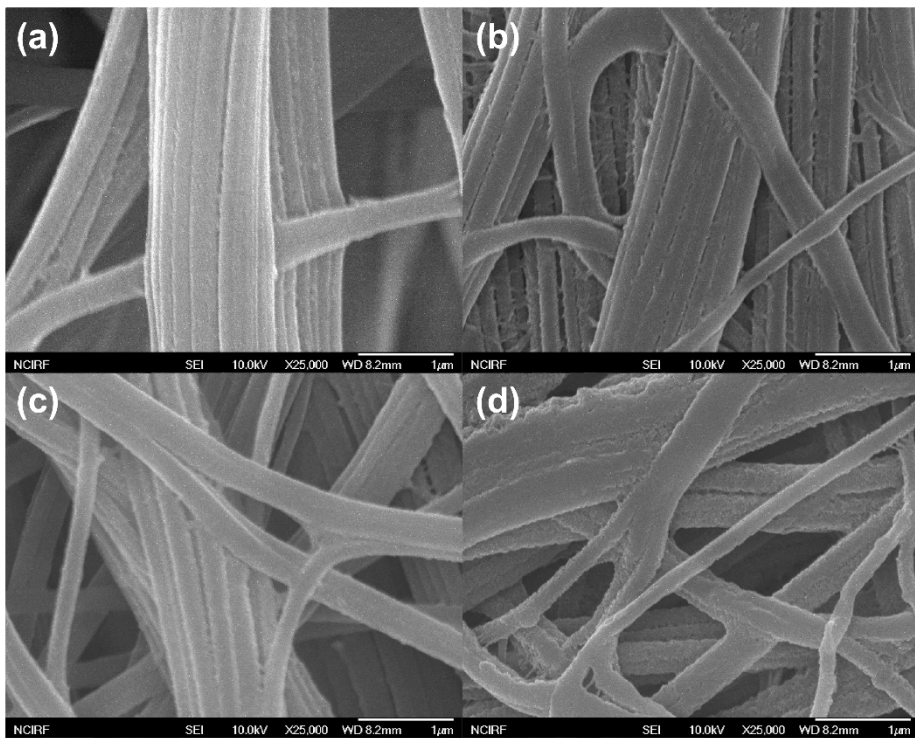


Figure IV-5. FE-SEM images of (a) *mANF-2-120*, (b) *mANF-4-120*, (c) *mANF-6-120* and (d) *mANF-8-120*.

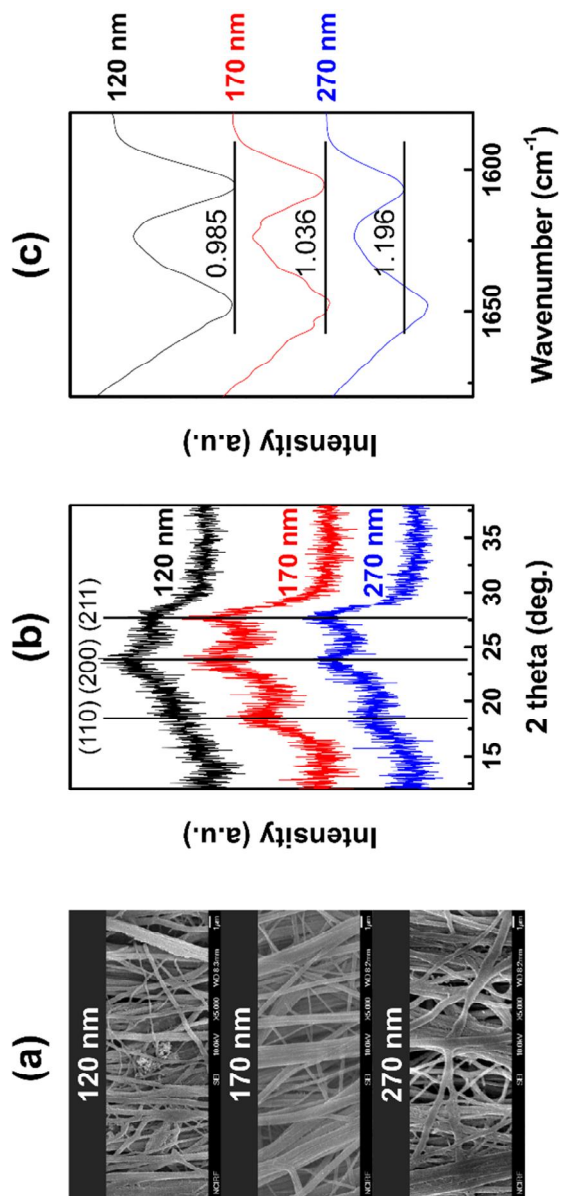


Figure IV-6. (a) FE-SEM image, (b) XRD patterns and (c) FT-IR spectra of *m*ANF-6-120 with average diameters of 120, 170 and 270 nm.

IV-3-2. Effect of size on degree of crystallization of *meta*-aramid nanofibers

Three types of *m*ANF-As with different average fiber diameters (120, 170, and 270 nm) were crystallized using the optimized solvent-assisted heat treatment procedure. The *m*ANF mats maintained their nanofiber structure after the treatment (Fig. IV-6 (a)). The crystal structures of the *m*ANF mats were analyzed using XRD and ATR FT-IR spectra. Considering that the free-surface-to-volume ratio increases with decreasing diameter of the nanofibers, it is presumed that crystallization of the amorphous chains more readily occurs as the diameter of the nanofibers decreases. However, as shown in Fig. IV-6 (b), the XRD peak intensity decreased as the nanofiber diameter decreased. The crystallinities of *m*ANFs with 120, 170 and 270 nm of diameter were 30, 40 and 45%, respectively. Furthermore, the intensity ratio of the peaks at 1604 and 1647 cm^{-1} decreased with decreasing diameter of the nanofibers, indicating that crystallization of thin nanofibers was suppressed. The lower crystallinity of the thinner nanofibers might be due to the suppression of the molecular mobility of the amorphous chains. The rigidly confined amorphous chains in these thin nanofibers could not easily rearrange and crystallize during the solvent-assisted heat treatment. Therefore, in addition to the solvent composition and heat treatment temperature, it is necessary to consider the size effect of nanofibers minutely when applying solvent-assisted treatment to crystallize these nanofibers.

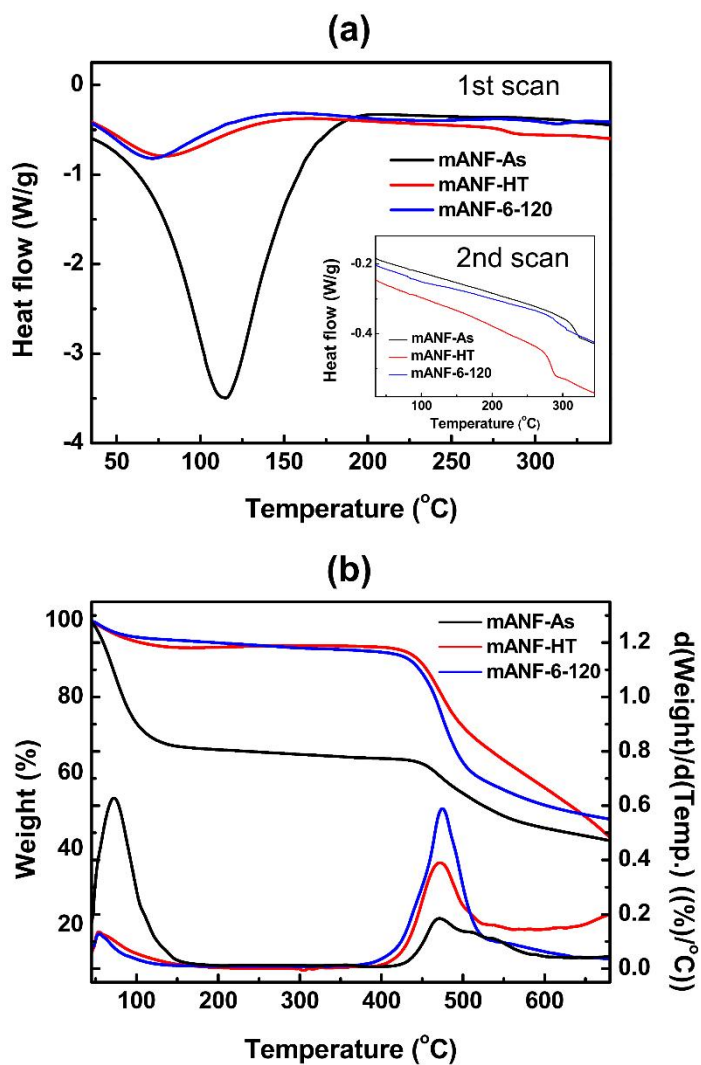


Figure IV-7. (a) DSC curves for the first and second (insert) heating of *mANF-As*, *mANF-HT* and *mANF-6-120* and (b) TGA curves of *mANF-As*, *mANF-HT* and *mANF-6-120*.

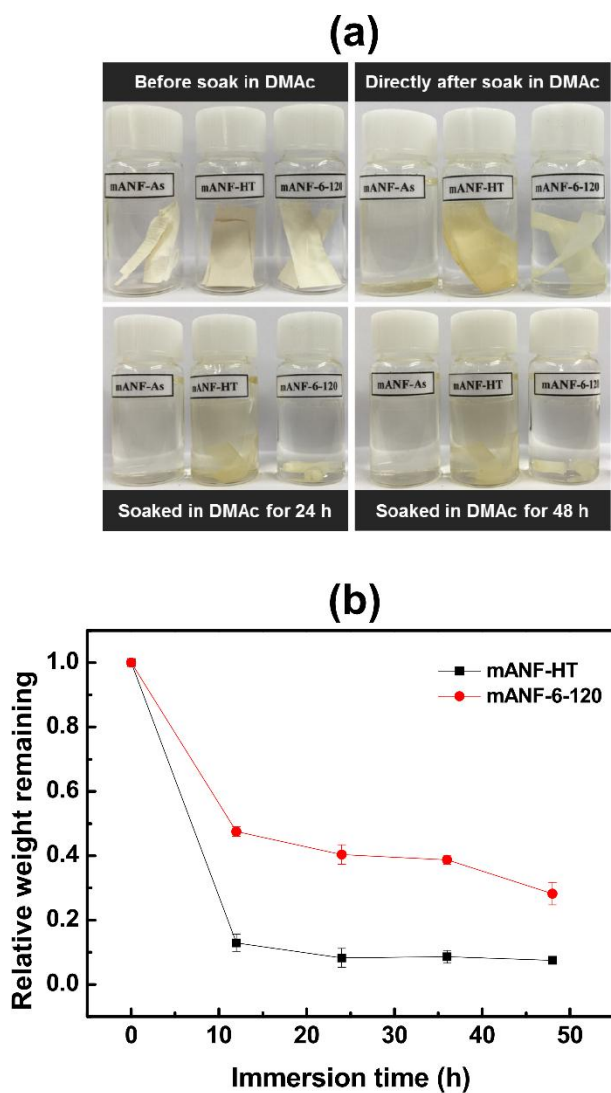


Figure IV-8. Observation of the chemical stability. (a) Macroscopic image of *mANF-As*, *mANF-HT* and *mANF-6-120* soaked in DMAc, and (b) relative weight of *mANF-As*, *mANF-HT* and *mANF-6-120* at a specific immersion time.

IV-3-3. Thermal properties and chemical stability of *meta*-aramid nanofibers

mANF-As, *mANF*-HT and *mANF*-6-120 with average diameter of 170 nm were used to further characterize the various properties of *mANFs*. The thermal properties of *mANFs* were evaluated using DSC and TGA analysis and the results are shown in Fig. 6. The DSC curve of *mANF*-As (Fig. 7 (a)) exhibited a large endothermic peak at approximately 115 °C in the first heating cycle. In contrast, the DSC curves for *mANF*-HT and *mANF*-6-120 exhibited relatively small endothermic peaks at 71 and 80 °C, respectively, in the first heating cycle. The endothermic peak was considered to be caused by the evaporation of moisture adsorbed in the *mANF* mats. In this regard, *mANF*-As might exhibit a large endothermic peak during the first heating cycle because *mANF*-As contains a considerable amount of Cl ions which could strongly interact with water molecules. Because the Cl ions were removed during washing with distilled water or co-solvent, *mANF*-HT and *mANF*-6-120 might exhibit a relatively small endothermic peak compared to that of *mANF*-As. These endothermic peaks were not observed during the second heating cycle of *mANF*-As, *mANF*-HT, and *mANF*-6-120 because the moisture was completely removed during the first heating cycle. The TGA

curves for *mANF-As*, *mANF-HT*, and *mANF-6-120*, shown in Fig. 7 (b), experienced weight loss in two steps at approximately 40–120 °C and 400–600 °C, which is commonly observed in the heating of bulk *meta*-aramid.³⁴⁻³⁵ The weight loss of *mANF-As* in the low-temperature region (below 120 °C) was noticeably high compared to that of *mANF-HT* and *mANF-6-120* due to the large amount of moisture in *mANF-As*. In addition, the weight loss of *mANF-As*, *mANF-HT*, and *mANF-6-120* at high temperature caused by the chain decomposition occurred at similar temperatures. This result suggests that thermal stability was not deteriorated by the heat treatment at 300 °C or the solvent-assisted heat treatment.

The chemical stability of *mANFs* was investigated by evaluating their ability to survive in DMAc. As shown in Fig. 8 (a), *mANF-As* dissolved immediately upon immersion in DMAc, indicating that the amorphous *meta*-aramid chains are easily dissolved in DMAc. In contrast, *mANF-HT* and *mANF-6-120*, both of which possess a crystalline phase, retained their shape immediately after immersion in DMAc. This suggests that crystalline *meta*-aramid chains are highly resistant to DMAc. Directly after being immersed in DMAc, the *mANF-HT* mat appeared opaque and yellowish, after which it gradually became translucent while soaking in DMAc for 48 hours, implying that a considerable number of amorphous chains in *mANF-HT* might be dissolved in

DMAc. Meanwhile, the white-colored *m*ANF-6-120 mat retained its original shape immediately after immersion in DMAc and remained consistently white and opaque after being soaked in DMAc for 48 hours. Additionally, the relative remaining weight of *m*ANF-6-120 after immersion for 48 h in DMAc was 0.28, whereas that of *m*ANF-HT was 0.07 (Fig. 8 (b)). These results indicate that the *m*ANF-6-120 contains a larger amount of crystalline phase than *m*ANF-HT, resulting in enhanced chemical resistance to DMAc compared to *m*ANF-HT. These results indicate that the chemical of the *meta*-aramid nanofiber mat could be efficiently enhanced by low-temperature solvent-assisted heat treatment.

IV-4. Conclusion

This study investigated the use of solvent-assisted heat treatment to regenerate the crystal structure of *meta*-aramid nanofibers (*m*ANFs). The *m*ANFs were fabricated using electrospinning, and the as-spun *m*ANF possessed an amorphous chain structure. The *m*ANFs were subjected to solvent-assisted heat treatment by varying the composition of the co-solvent and the heat treatment temperature. It was found that DMAc molecules in the co-solvent facilitate the disentanglement of the amorphous chains to enable them to easily rearrange to form a crystal structure. The use of a solution with an excessive DMAc concentration above 6 v/v% (DMAc:water) resulted in the *m*ANF mats becoming excessively brittle, which made them difficult to handle; thus, the optimal volume composition of the solution containing the co-solvent was selected as 6:5:100 (DMAc:EG:water). In addition, efficient crystallization required conditions under which the evaporation rate of DMAc was relatively slow, which was achieved by subjecting the *m*ANF mat to heat treatment at the optimal heat treatment temperature of 120 °C. The *m*ANF mat treated under the optimized conditions exhibited superior chemical stability compared to those of the as-spun *m*ANF and *m*ANF mats heat-treated at high temperature (300 °C). The crystallinity of *m*ANFs decreased from 45 to 30% with decreasing diameter from 270 to 120 nm when *m*ANFs-As was crystallized. This low-temperature solvent-assisted heat treatment neither

involves excessive energy consumption nor undesirable damage to the nanofibers. Therefore, this method would be practically useful for the application of *meta*-aramid nanofibers in various industrial fields ranging from wastewater treatment to the removal of hazardous chemical components in air.

References and Notes

1. Kim, E.-M.; Jang, J., Surface modification of meta-aramid films by UV/ozone irradiation. *Fibers and Polymers* **2010**, *11* (5), 677-682.
2. Shealy, O. L., *Tex. Inst. Ind.* **1971**, *9* (1), 10-14.
3. Lu, Z.; Hu, W.; Xie, F.; Hao, Y., Highly improved mechanical strength of aramid paper composite via a bridge of cellulose nanofiber. *Cellulose* **2017**, *24* (7), 2827-2835.
4. Jeon, K. S.; Nirmala, R.; Navamathavan, R.; Kim, K. J.; Chae, S. H.; Kim, T. W.; Kim, H. Y.; Park, S. J., The study of efficiency of Al₂O₃ drop coated electrospun meta-aramid nanofibers as separating membrane in lithium-ion secondary batteries. *Materials Letters* **2014**, *132*, 384-388.
5. Oh, H. J.; Pant, H. R.; Kang, Y. S.; Jeon, K. S.; Pant, B.; Kim, C. S.; Kim, H. Y., Synthesis and characterization of spider-web-like electrospun mats of meta-aramid. *Polymer International* **2012**, *61* (11), 1675-1682.
6. Wu, Y.-J.; Seferis, J. C.; Lorentz, V., Evaluations of an aramid fiber in nonwoven processes for honeycomb applications. *Journal of Applied Polymer Science* **2002**, *86* (5), 1149-1156.
7. Levit, N. V.; Young, R. H., Flame resistant thermal liner, composite fabric, and garment. Google Patents: 2016.

8. Jiang, Z.; Tijing, L. D.; Amarjargal, A.; Park, C. H.; An, K.-J.; Shon, H. K.; Kim, C. S., Removal of oil from water using magnetic bicomponent composite nanofibers fabricated by electrospinning. *Composites Part B: Engineering* **2015**, *77*, 311-318.
9. Tijing, L. D.; Choi, J.-S.; Lee, S.; Kim, S.-H.; Shon, H. K., Recent progress of membrane distillation using electrospun nanofibrous membrane. *Journal of Membrane Science* **2014**, *453*, 435-462.
10. Dzenis, Y., Spinning Continuous Fibers for Nanotechnology. *Science* **2004**, *304* (5679), 1917.
11. Aussawasathien, D.; Teerawattananon, C.; Vongachariya, A., Separation of micron to sub-micron particles from water: Electrospun nylon-6 nanofibrous membranes as pre-filters. *Journal of Membrane Science* **2008**, *315* (1-2), 11-19.
12. Ghasemi-Mobarakeh, L.; Semnani, D.; Morshed, M., A novel method for porosity measurement of various surface layers of nanofibers mat using image analysis for tissue engineering applications. *Journal of Applied Polymer Science* **2007**, *106* (4), 2536-2542.
13. Taha, A. A.; Qiao, J.; Li, F.; Zhang, B., Preparation and application of amino functionalized mesoporous nanofiber membrane via electrospinning for adsorption of Cr³⁺ from aqueous solution. *Journal of Environmental Sciences* **2012**, *24* (4), 610-616.

14. Lee, J. H.; Manuel, J.; Liu, Y.; Park, K. E.; Park, W. H.; Ahn, J.-H., High Temperature Resistant Electrospun Nanofibrous Meta-Aramid Separators for Lithium Ion Batteries. *Journal of Nanoscience and Nanotechnology* **2016**, *16* (10), 10724-10729.
15. Nie, C.; Yang, Y.; Peng, Z.; Cheng, C.; Ma, L.; Zhao, C., Aramid nanofiber as an emerging nanofibrous modifier to enhance ultrafiltration and biological performances of polymeric membranes. *Journal of Membrane Science* **2017**, *528*, 251-263.
16. On, S. Y.; Kim, M. S.; Kim, S. S., Effects of post-treatment of meta-aramid nanofiber mats on the adhesion strength of epoxy adhesive joints. *Composite Structures* **2017**, *159*, 636-645.
17. Ryu, S. Y.; Chung, J. W.; Kwak, S. Y., Tunable multilayer assemblies of nanofibrous composite mats as permeable protective materials against chemical warfare agents. *RSC Advances* **2017**, *7* (16), 9964-9974.
18. Wei, Z.; Zhang, Q.; Wang, L.; Peng, M.; Wang, X.; Long, S.; Yang, J., The preparation and adsorption properties of electrospun aramid nanofibers. *Journal of Polymer Science Part B: Polymer Physics* **2012**, *50* (20), 1414-1420.
19. Yu, J.; Kim, Y.-G.; Kim, D. Y.; Lee, S.; Joh, H.-I.; Jo, S. M., Super high flux microfiltration based on electrospun nanofibrous m-aramid

- membranes for water treatment. *Macromolecular Research* **2015**, *23* (7), 601-606.
20. Yao, L.; Lee, C.; Kim, J., Fabrication of electrospun meta-aramid nanofibers in different solvent systems. *Fibers and Polymers* **2010**, *11* (7), 1032-1040.
 21. Mazzocchetti, L.; Benelli, T.; Maccaferri, E.; Merighi, S.; Belcari, J.; Zucchelli, A.; Giorgini, L., Poly-m-aramid electrospun nanofibrous mats as high-performance flame retardants for carbon fiber reinforced composites. *Composites Part B: Engineering* **2018**, *145*, 252-260.
 22. Yao, L. R.; Kim, J. Y., The Microstructure and Mechanical Property of Meta-Aramid Nanofiber Web for High Temperature Filter Media. *Advanced Materials Research* **2011**, *175-176*, 318-322.
 23. Oh, H. J.; Han, S. H.; Kim, S. S., A novel method for a high-strength electrospun meta-aramid nanofiber by microwave treatment. *Journal of Polymer Science Part B: Polymer Physics* **2014**, *52* (12), 807-814.
 24. Ryu, S.-Y.; Chung, J. W.; Kwak, S.-Y., Amphiphobic meta -aramid nanofiber mat with improved chemical stability and mechanical properties. *European Polymer Journal* **2017**, *91*, 111-120.
 25. Cheng, Y.-W.; Wang, C., Solvent-induced crystallization of electrospun syndiotactic polystyrene nanofibers and its reversible desorption/sorption of volatile organic vapors. *Journal of Polymer Research* **2016**, *23* (11).

26. Jeong, L.; Lee, K. Y.; Liu, J. W.; Park, W. H., Time-resolved structural investigation of regenerated silk fibroin nanofibers treated with solvent vapor. *Int J Biol Macromol* **2006**, *38* (2), 140-4.
27. Cheng, Y.-W.; Lu, H.-A.; Wang, Y.-C.; Thierry, A.; Lotz, B.; Wang, C., Syndiotactic Polystyrene Nanofibers Obtained from High-Temperature Solution Electrospinning Process. *Macromolecules* **2010**, *43* (5), 2371-2376.
28. Ahn, Y.; Hu, D. H.; Hong, J. H.; Lee, S. H.; Kim, H. J.; Kim, H., Effect of co-solvent on the spinnability and properties of electrospun cellulose nanofiber. *Carbohydr Polym* **2012**, *89* (2), 340-5.
29. Kim, N.; Kee, S.; Lee, S. H.; Lee, B. H.; Kahng, Y. H.; Jo, Y. R.; Kim, B. J.; Lee, K., Highly conductive PEDOT:PSS nanofibrils induced by solution-processed crystallization. *Adv Mater* **2014**, *26* (14), 2268-72, 2109.
30. Castro-Muñiz, A.; Martínez-Alonso, A.; Tascón, J. M. D., Modification of the pyrolysis/carbonization of PPTA polymer by intermediate isothermal treatments. *Carbon* **2008**, *46* (7), 985-993.
31. Panar, M.; Avakian, P.; Blume, R. C.; Gardner, K. H.; Gierke, T. D.; Yang, H. H., Morphology of poly(p-phenylene terephthalamide) fibers. *Journal of Polymer Science: Polymer Physics Edition* **1983**, *21* (10), 1955-1969.

32. Wang, W.; Li, R.; Tian, M.; Liu, L.; Zou, H.; Zhao, X.; Zhang, L., Surface silverized meta-aramid fibers prepared by bio-inspired poly(dopamine) functionalization. *ACS Appl Mater Interfaces* **2013**, *5* (6), 2062-9.
33. Davis, R.; Chin, J.; Lin, C.-C.; Petit, S., Accelerated weathering of polyaramid and polybenzimidazole firefighter protective clothing fabrics. *Polymer Degradation and Stability* **2010**, *95* (9), 1642-1654.
34. Brown, J. R.; Power, A. J., Thermal degradation of aramids: Part I—Pyrolysis/gas chromatography/mass spectrometry of poly(1,3-phenylene isophthalamide) and poly(1,4-phenylene terephthalamide). *Polymer Degradation and Stability* **1982**, *4* (5), 379-392.
35. Villar-Rodil, S.; Paredes, J. I.; Martínez-Alonso, A.; Tascón, J. M. D., Atomic Force Microscopy and Infrared Spectroscopy Studies of the Thermal Degradation of Nomex Aramid Fibers. *Chemistry of Materials* **2001**, *13* (11), 4297-4304.

CHAPTER V

Vapor-Assisted Crystallization of *meta*-Aramid

Nanofibers

V-1. Introduction

The crystallization of polymers is commonly conducted by cooling from melt, mechanical stretching or solvent evaporation. However, when nanofibrous polymer materials is needed to be crystallized, most of the conventional crystallization methods could not be applied because the nanostructure is vulnerable to the crystallization process. Therefore, persistent efforts have been made to crystallize the polymer nanofibers without disrupting their nanostructure.

As a facile process for the crystallization of nanofibers, solvent-assisted crystallization have been extensively investigated. When the nanofibrous mat is immersed to the solvent, the solvent impeded into the nanofibers plasticizes the chains, facilitating the amorphous chains to be aligned at lower temperature than the glass transition temperature.¹⁻² Additionally, meta-aramid nanofiber (*m*ANFs) mats were successfully crystallized by solvent-assisted

crystallization in chapter IV. Although the solvent-assisted crystallization is a simple way to crystallize the nanofibers, the use of an excessive amount of solvent could result in environmental pollution. In addition, the crystallization during the vaporization of solvent could not be controlled easily, thus it's hard to uniformly crystallize the nanofibrous mat during heat treatment.³ In contrast, solvent vapor-assisted crystallization requires only a small amount of solvent and the solvent vapor could be more uniformly invaded into the nanofibrous mat. For instance, electrospun nanofibers based on the various polymers such as silk, polylactic acid and syndiotactic polystyrene have been successfully crystallized in the chambers filled with solvent vapor.³⁻¹² However, there was no study on vapor-assisted crystallization of *m*ANFs.

In this study, vapor-assisted crystallization process for *m*ANFs was developed and the effect of size on the degree of crystallization of *m*ANFs was observed. It was shown that the DMAc and aniline mixture could effectively crystallize the *m*ANFs. The effect of composition of DMAc and aniline was investigated. It was found that the crystallization of *m*ANFs was most effectively conducted when the DMAc:aniline volume ratio was 2.6:1. In addition, the degree of crystallization of *m*ANFs was highest at 120 °C. *m*ANFs having different diameter was treated under the optimum vapor-assisted crystallization process. The degree of crystallization decreased with decreasing diameter of *m*ANFs. This indicate that the decreased molecular

mobility could be closely related to the suppression of crystallization. The lower crystallinity resulted in the lower chemical stability of *m*ANFs. Therefore, the changes in chain mobility with decreasing the diameter of polymer nanofibers should be thoroughly considered to crystallize the polymer nanofibers.

V-2. Experimental Section

V-2-1. Materials

Poly(*meta*-phenylene isophthalamide) (*meta*-aramid, Nomex®) fiber was purchased from DuPont Plant. Lithium chloride (LiCl, ACS reagent, $\geq 99\%$) was purchased from Sigma-Aldrich. *N,N*-Dimethylacetamide (DMAc, $\geq 99.5\%$) and aniline ($\geq 99.0\%$) were purchased from Daejung Chemical & Metals Co. All materials were used as received without further purification. The LiCl and *meta*-aramid were dried at 80 °C for 12 h in a vacuum oven to remove the moisture. Highly deionized water (18 M Ω cm) was used throughout the experiments.

V-2-2. Fabrication of *meta*-aramid nanofibers

The electrospinning of *meta*-aramid was conducted under similar condition described in chapter IV.¹³ The electrospinning solution was prepared by dissolving *meta*-aramid fibers and LiCl in DMAc at 60 °C for 24 h in an oven shaker. The concentration of *meta*-aramid was 12, 13, and 14 w/v%. The *meta*-aramid/LiCl ratio was 5:2 by mass. *Meta*-aramid nanofibers were fabricated using an electrospinning apparatus (NanoNC, Korea). The device was composed of a high DC-voltage supply, syringe pumps, and a rotating drum-type collector. The *meta*-aramid solution was placed in a 10-mL syringe

equipped with a steel needle with an internal diameter of 0.33 mm. The collector was covered by aluminum foil and placed 15 cm away from the needle tip. A positive voltage of 20 kV was applied to the tip of the syringe needle and a negative voltage of -5 kV was applied to the collector. The rotating speed of the collector was 200 RPM and the flow rate of the solution was 0.35 mL/h. The temperature and relative humidity in the electrospinning apparatus were maintained in the ranges 20 to 25 °C and 40 to 50%, respectively. Electrospinning was conducted using a syringe for 20 h.

V-2-3. Crystallization of *meta*-aramid nanofibers

The as-spun *m*ANFs were washed in deionized water for 30 mins and dried in a vacuum oven at room temperature for 24 h. solvent/non-solvent mixture was prepared by mixing 2.0 mL of aniline and a different amount of DMAc (2, 2.8, 3.6, 4.4, 5.2 mL) in a vial. The vial containing solvent/non-solvent mixture and the washed samples fixed to stainless steel frame were placed in a 170 mL Teflon-lined stainless steel autoclave. Heat treatment was conducted in an oven at various temperature (80, 100, 120, 140, 160 and 180 °C) for 1 h. After the heat treatment, *m*ANF mat was washed in water and dried in a vacuum oven at room temperature for 24 h.

V-2-4. Characterization of *meta*-aramid nanofibers

The microstructure of the *m*ANFs was observed by field emission scanning electron microscopy (FE-SEM, JSM-6700F) at an accelerating voltage of 10 kV. The average diameter of *m*ANFs was determined by measuring the diameter of 100 nanofibers from the FE-SEM images at random. The diameter of *m*ANFs was measured using image analysis software (EyeViewAnalyzer, Digiplus Inc.). The crystal structure was analyzed using X-ray diffraction method (XRD, New D8 Advance) over the 2θ range of 10-40° using Cu K α radiation as the X-ray source ($\lambda = 0.154$ nm). Crystallinity of *m*ANFs was obtained using software package (Diffraction.Suite EVA, Bruker). The thermal properties were studied by thermal gravimetric analysis (TGA, Discovery TGA). The TGA analysis was conducted under a nitrogen condition, and the temperature range for the TGA analysis was 25–700 °C and the heating rate was 10 °C/min. The chemical stability of *m*ANFs was measured by soaking the *m*ANF mat in DMAc. The relative weight of the *m*ANF mat was measured by weighing the mat after a specified immersion period (12, 24, 36, and 48 h).

V-3. Results and Discussion

V-3-1. Morphology of as-spun *meta*-aramid nanofibers

The microstructure of *m*ANFs were observed by FE-SEM. As shown Fig. V-1, *m*ANFs with uniform and bead-free morphology were successfully fabricated. The diameter of *m*ANFs increased with increasing polymer concentration. The average diameters of *m*ANFs made by polymer solution with concentration of 12, 13 and 14 w/v% were 90, 110 and 160 nm, respectively. In chapter IV, several tens of nanofibers were bundled (See Fig. IV-1). The high conductivity of the solution, which was caused by its high salt concentration, resulted the spinning solution to move directly to the collector. The solution jet was extended continuously and formed bundles, rather than being scattered and forming randomly spread nanofibers. However, The formation of bundles might not be appropriate for the further application of nanofibers. To avoid the bundle formation, rotation speed of the drum collector was increased. In addition, the angle at which the nozzle was pointing was adjusted to the bottom of the drum collector. These changes effectively hindered the continuous extension of the jet. As a result, the individual nanofibers or smaller bundles than the bundle shown in chapter IV were observed.

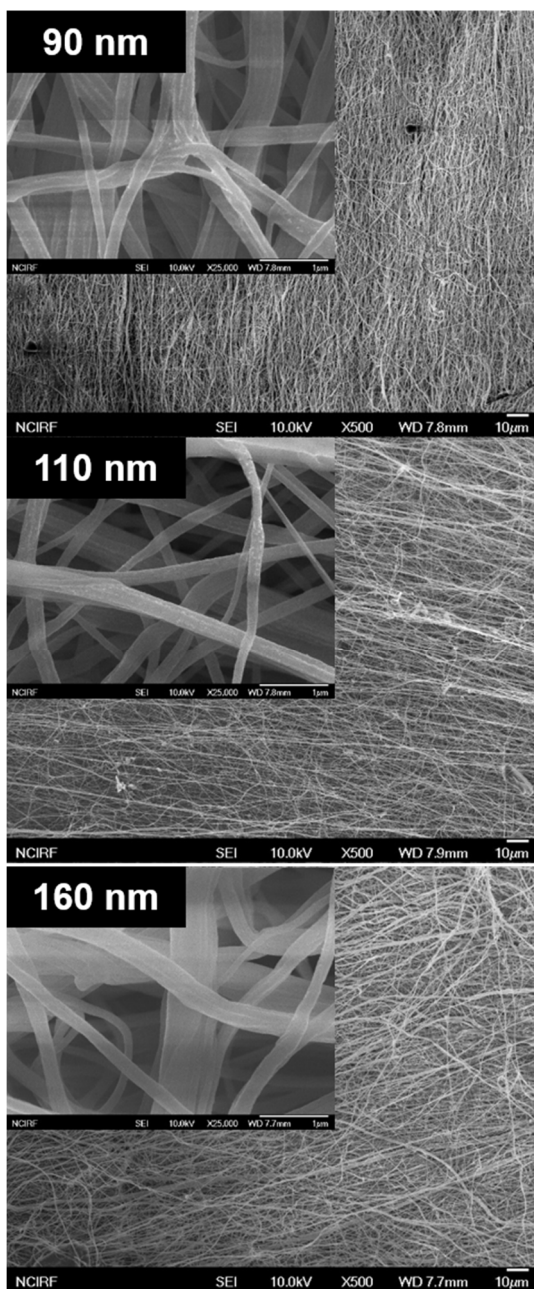


Figure V-1. FE-SEM images of the as-spun *meta*-aramid nanofibers with different diameters.

Table V-1. Physical properties of the *meta*-aramid nanofiber solutions and average fiber diameter of the as-spun *meta*-aramid nanofibers.

<i>Meta</i> -aramid concentration (w/v%)	12	13	14
LiCl concentration (w/v%)	4.8	5.2	5.6
Average fiber diameter (μm)	0.09 ± 0.03	0.11 ± 0.03	0.16 ± 0.04

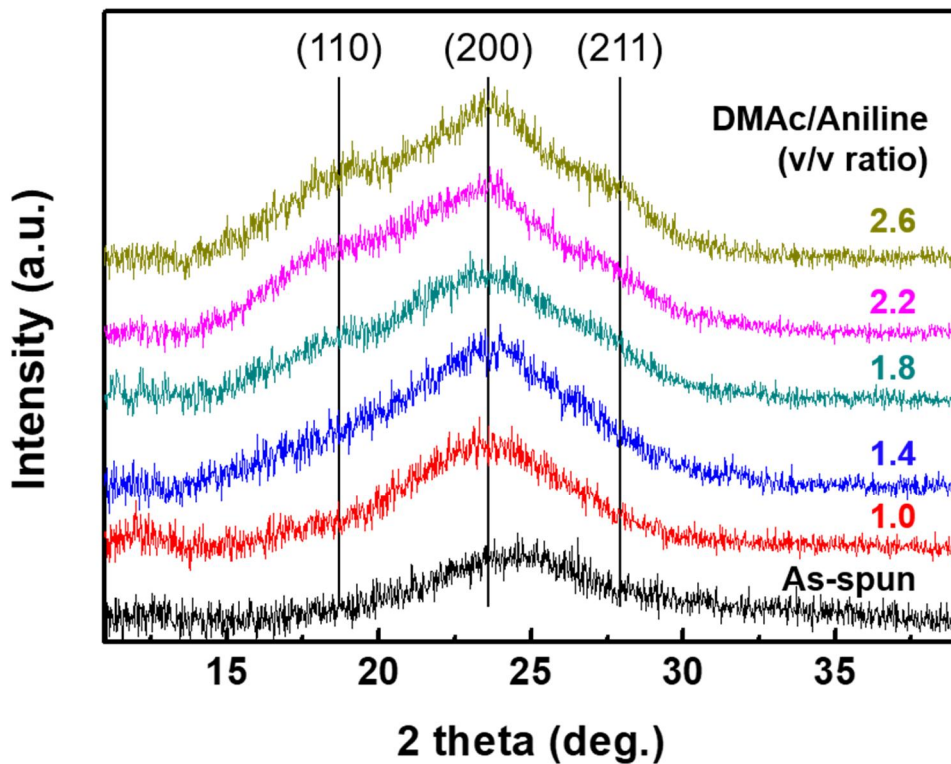


Figure V-2. XRD patterns of *m*ANFs treated with DMAC/aniline mixture at 160 °C. The composition of the mixture is 1.0, 1.4, 1.8, 2.2 and 2.6 of DMAC/aniline volume ratio.

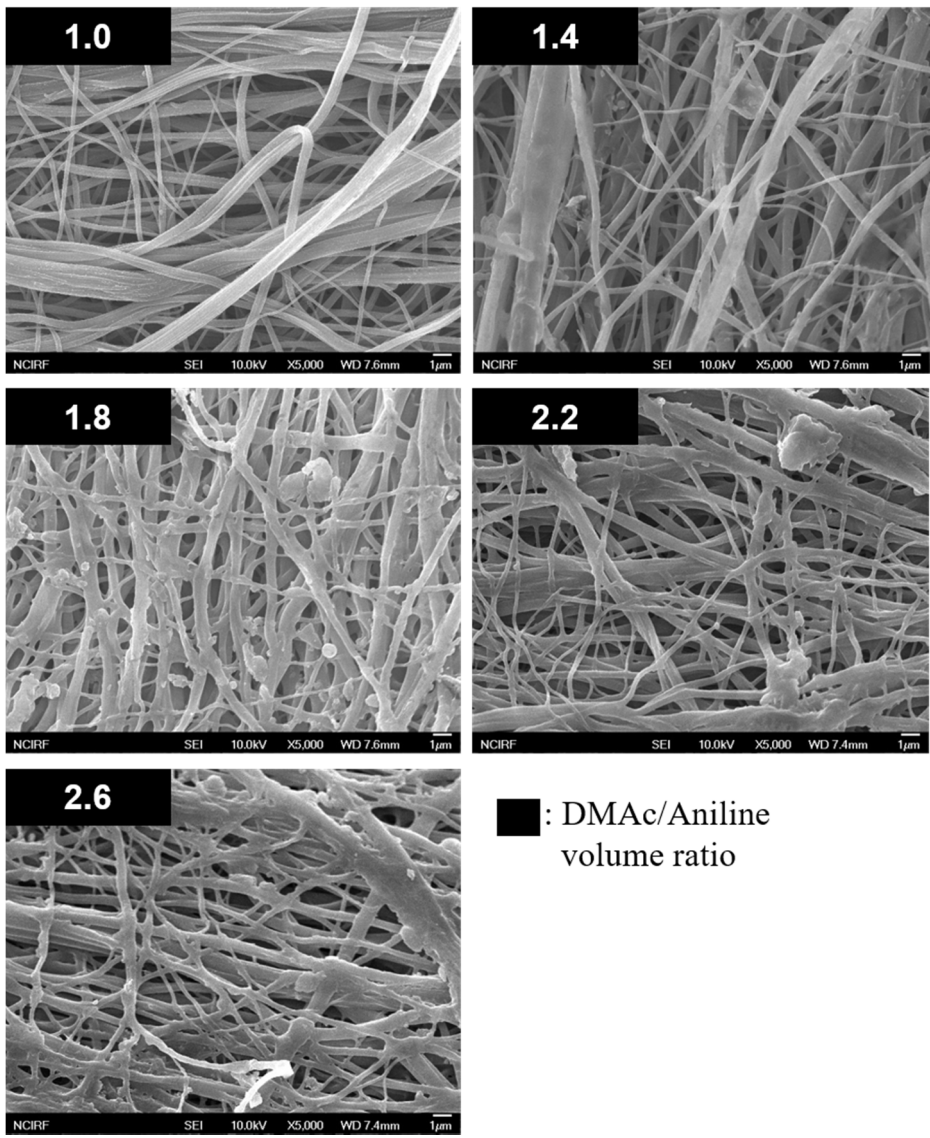


Figure V-3. FE-SEM images of the as-spun *meta*-aramid nanofibers with different diameters.

V-3-2. Effect of solvent composition on crystallization of *m*ANFs

It is commonly believed that the solvent- or solvent vapor-assisted crystallization of polymer chains is promoted by the plasticization of the polymer chain by solvent molecule.¹⁴⁻¹⁵ The activated chain motion results in crystallization, thus the crystallization process is largely affected by the type of solvent. The main factor for the solvent- or solvent vapor-assisted crystallization of chains is solubility of the solvent to chains. With increasing solubility, molecular mobility of chains becomes higher, promoting the crystallization. When the solubility is higher than a certain value, however, chains are gelled and hardly cross-linked. Therefore, crystallization of chains could be rather hindered when the chains are exposed to the solvent vapor with solubility higher than a certain value.

To investigate the effect of solvent property, solvent/non-solvent mixture with various composition was exposed to *m*ANFs. In chapter IV, DMAc and ethylene glycol (EG) were selected as solvent and non-solvent, respectively. However, *m*ANF mats were easily melted when they were exposed to the vaporized DMAc/EG composed of various DMAc/EG composition. Boiling points of DMAc and EG are approximately 165.0 and 197.3 °C, vapor pressure of the DMAc is much higher than that of EG. For instance, the vapor pressure of DMAc at room temperature is almost 30 times higher than that of EG. Therefore, there might be much more DMAc molecules in gas phase than

EG molecules when DMAc/EG solvent was vaporized. Exposure of *m*ANFs to vapor composed mostly of DMAc molecules would melt the *m*ANFs. Aniline acts as non-solvent to meta-aramid, and the boiling temperature of aniline is 184.1 °C, which is lower than that of EG. In addition, aniline is a miscible solvent to DMAc. Therefore, the solvent and non-solvent were selected as DMAc and aniline, respectively.

The XRD patterns for *m*ANFs exposed to vapors for various composition of DMAc/aniline mixture were displayed in Fig. V-2. The temperature during the vapor exposure was 160 °C which is sufficiently high to evaporate DMAc and aniline in a short time. The as-spun *m*ANFs did not show the diffraction peaks and showed wide peak for amorphous disordered peak at 24°. The *m*ANF mats treated with solvent mixture having 1.0 and 1.4 of DMAc/aniline volume ratio only showed broad diffraction peak for (200) plane. When *m*ANF mats were treated with the solvent mixture with 1.8, 2.2 and 2.6 volume ratio, main diffraction peak for (200) plane at 23.5° and shoulder peaks for (110) at 18.5° and (211) at 28.0° were observed.¹⁶⁻¹⁷ The intensity of diffraction peaks for (110), (200) and (211) plane of meta-aramid tended to increase with increasing DMAc/aniline ratio. As solvent to non-solvent ratio increases, the molecular mobility of the polymer chains could be enhanced. Therefore, the increase in DMAc ratio might result in an increased degree of crystallization. The *m*ANFs mat was melted and translucent film was obtained when *m*ANFs

mat was treated with solvent/non-solvent mixture with higher than 2.6 volume ratio (DMAc/aniline). This suggested that the chains were melted and fibrous structure was disrupted. Therefore, the appropriate solvent composition for the crystallization of *mANF* mats was selected as 2.6 of DMAc/aniline volume ratio.

The morphology of *mANFs* mats treated with various solvent composition at 160 was shown in Fig. V-3. It was observed that there was no noticeable changes in microstructure of *mANFs* when DMAc/aniline ratio was less than 1.4. The FE-SEM images of *mANF* treated with the solvent mixture with 1.8, 2.2 and 2.6 volume ratio exhibited a partially melted morphology. This indicated that *mANFs* were partially melted but maintained their porous structure during crystallization.

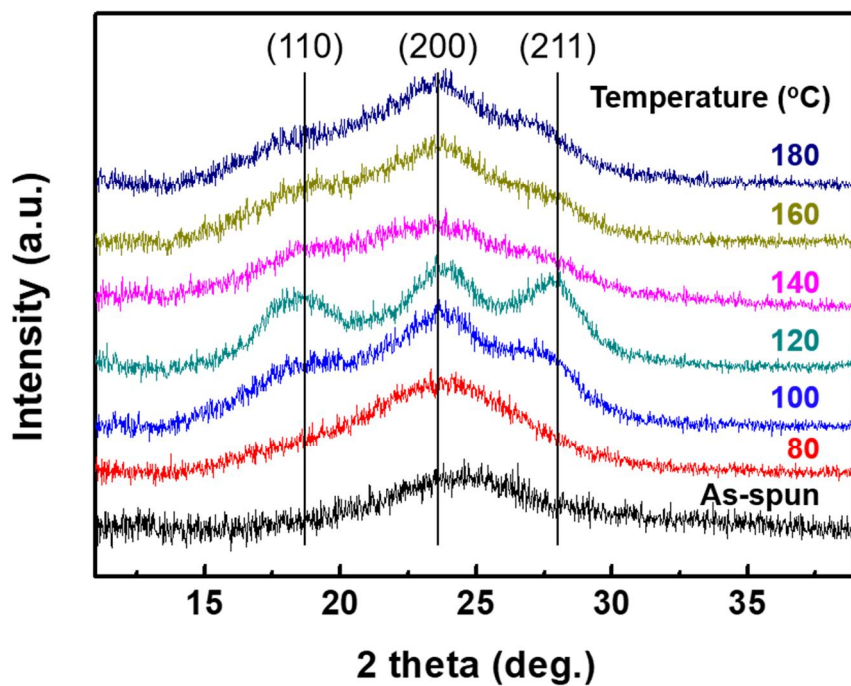


Figure V-4. XRD patterns of mANFs treated with DMAC/aniline mixture at 160 °C. The composition of the mixture is 1.0, 1.4, 1.8, 2.2 and 2.6 of DMAC/aniline volume ratio.

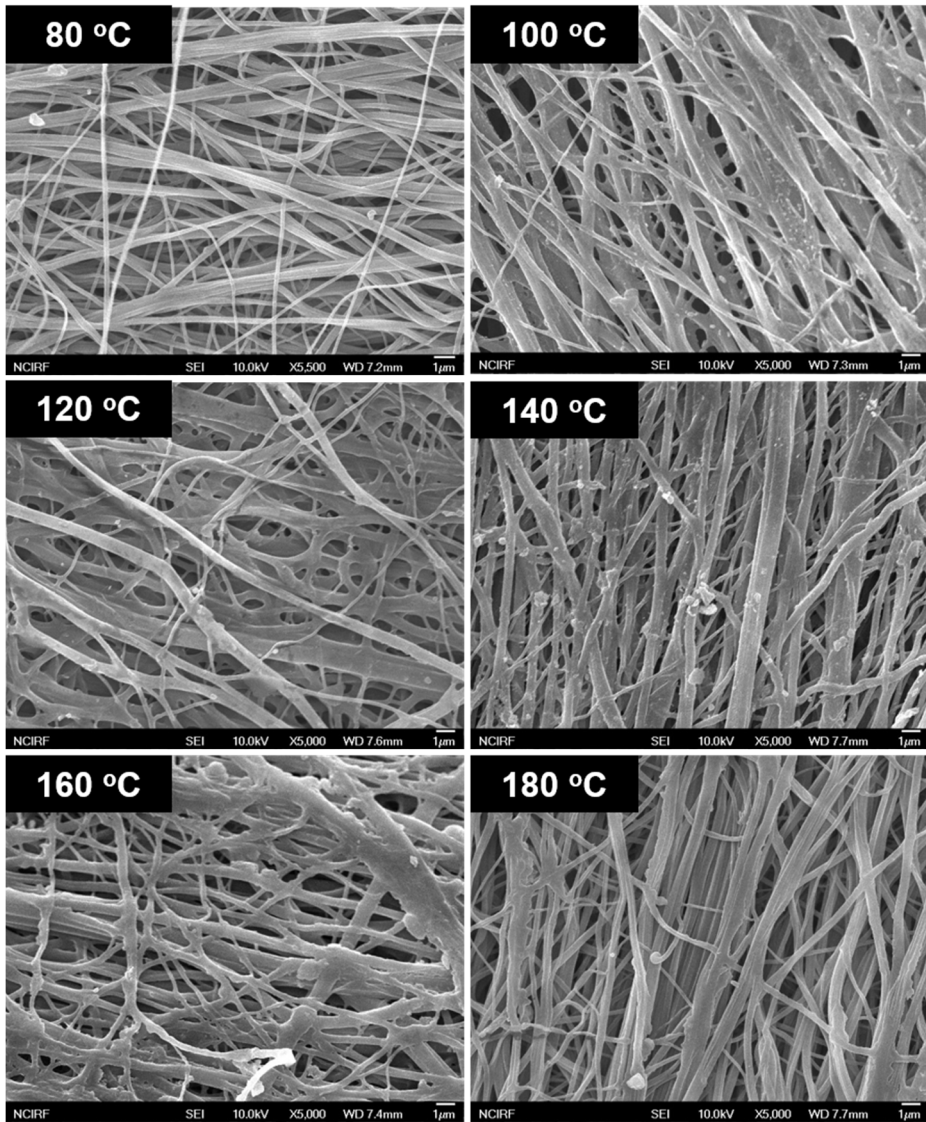


Figure V-5. FE-SEM images of the as-spun *meta*-aramid nanofibers with different diameters.

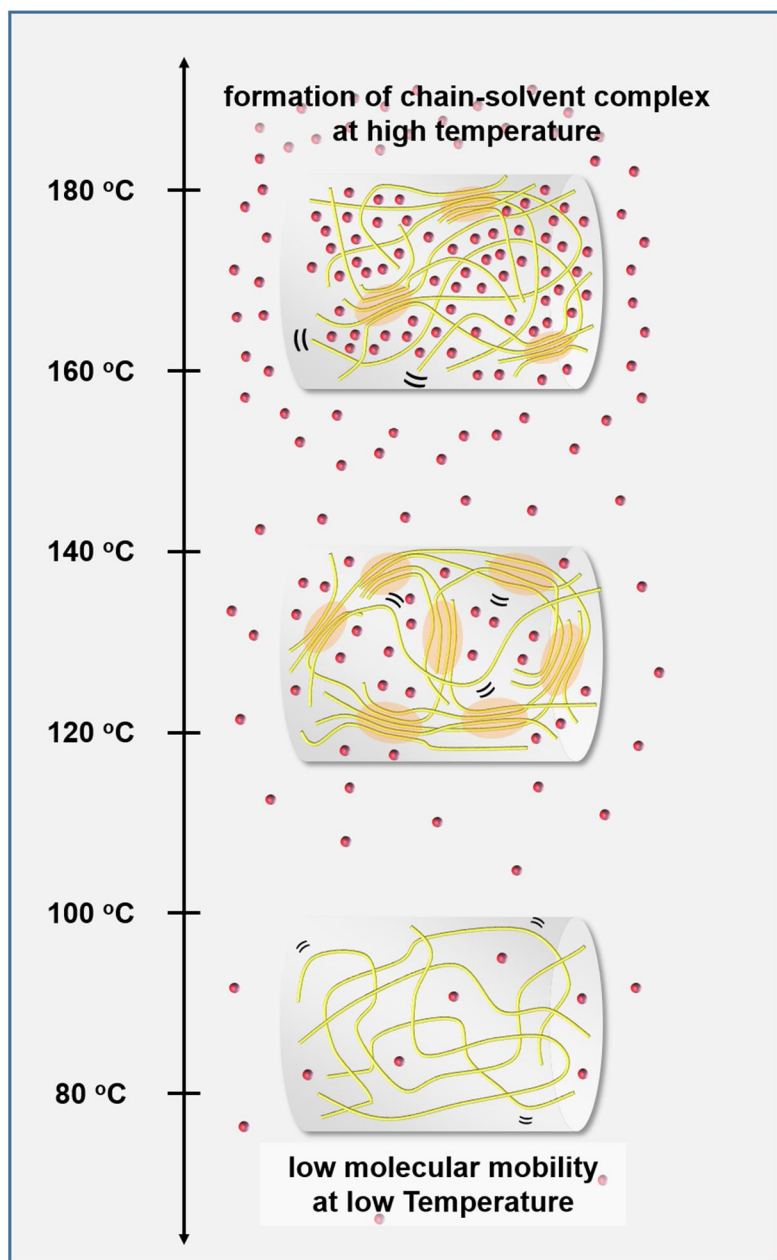


Figure V-6. Schematic illustration of the effect of temperature on vapor-assisted crystallization of *m*ANFs.

V-3-3. Effect of temperature on crystallization of *meta*-aramid nanofibers

The as-spun *m*ANF mats were heat-treated with solvent/non-solvent mixture (DMAc/Aniline = 2.6 v/v) at various temperature. As shown in Fig. V-4, the diffraction peak intensity for (110), (200) and (211) planes noticeably increased with increasing temperature from 80 to 120 °C. This result indicated that *m*ANFs mat was successfully crystallized at 120 °C. However, the diffraction peak intensity for *m*ANFs heat-treated at 140, 160 and 180 °C was lower than the *m*ANFs heat-treated at 120 °C. It is likely that increase in temperature causes the increase of molecular mobility and vapor pressure of DMAc. In general, the increased molecular mobility results in the increase of degree of crystallization. However, the increase in the interaction of polymer chains and solvent molecules does not always cause the increase in the degree of crystallization.¹⁴ As the solvent vapor interacts with chains, crystallization and gelation could be competitively happen. Although the chains have sufficient active energy to generate the crystalline nuclei, interaction with chains and solvent molecules could be preferred compared to the formation of chain-chain alignment at high temperature. When the chains prefer to interact with solvent molecules rather than crosslink with other chains, chains could be highly crystallized. Therefore, the increase in the crystallinity of *m*ANFs with increasing temperature from 80 to 120 °C might originate from the result from the increased molecular mobility and increased vapor pressure of DMAc.

On the other hand, the decreased crystallinity with increasing temperature from 120 to 180 °C might be a result from the increased tendency for the increase of formation of chain-solvent interaction.

The microstructure of the *m*ANFs treated at various temperature was observed by FE-SEM and shown in Fig. V-5. It was observed that the *m*ANFs treated at 80 °C did not show a noticeable change in nanofiber morphology, indicating that morphology of *m*ANFs were not affected by the solvent vapor due to the low molecular mobility and low vapor pressure. In contrast, the *m*ANFs treated at 100 to 180 °C exhibited a partially melted surfaces. This indicated that the *m*ANFs went through the partial melting and crystallization of chains simultaneously. The crystallization of *meta*-aramid chains might be most preferred at 120 °C while the partial melting of the chains by the formation of chain-solvent complex might be more preferred than the crystallization of chains at 100 °C and at 140 to 180 °C. The effect of temperature of crystallization of *m*ANFs is described in Fig. V-6. *m*ANFs treated at 100 to 180 °C still have a porous structure, thus it is likely to consider that *m*ANFs treated by the vapor-assisted crystallization methods could be applied to various applications such as filtration technology and protective clothes.

V-3-4. Effect of size on degree of crystallization of *meta*-aramid nanofibers

mANF-As with different average fiber diameters (90, 110, and 160 nm) were crystallized by the optimized vapor-assisted heat treatment procedure. The XRD patterns of the *mANF* mats were shown in Fig. V-7. Interestingly, the XRD peak intensity for *mANFs* noticeably decreased with decreasing the diameter, suggesting that crystallinity of *mANFs* decreased with decreasing diameter. The crystallinities of *mANFs* with 90, 110 and 160 nm of diameter were 24, 32 and 45%, respectively. These results corresponded to the results obtained at chapter IV. However, the decrease in crystallinity with decreasing diameter of *mANFs* were somewhat severe in vapor-assisted crystallization compared to the results in chapter IV. These results suggested that the size-dependent changes in molecular mobility and chain topology could strongly affect the vapor-induced crystallization.

The FE-SEM images of *mANFs* treated under optimum condition was shown in Fig. V-8. It was observed that the surface of *mANFs* was partially melted while maintain their porous structure. In general, electrospun polymer nanofibers with the smaller average diameter could possess higher porosity and surface area. Therefore, there could be trade-off relationship between porosity and degree of crystallization of *mANFs*. The results for the degree of the crystallization of *mANF* suggested that appropriate target diameter of the

nanofibers should be considered when crystallization process for nanofibers is investigated.

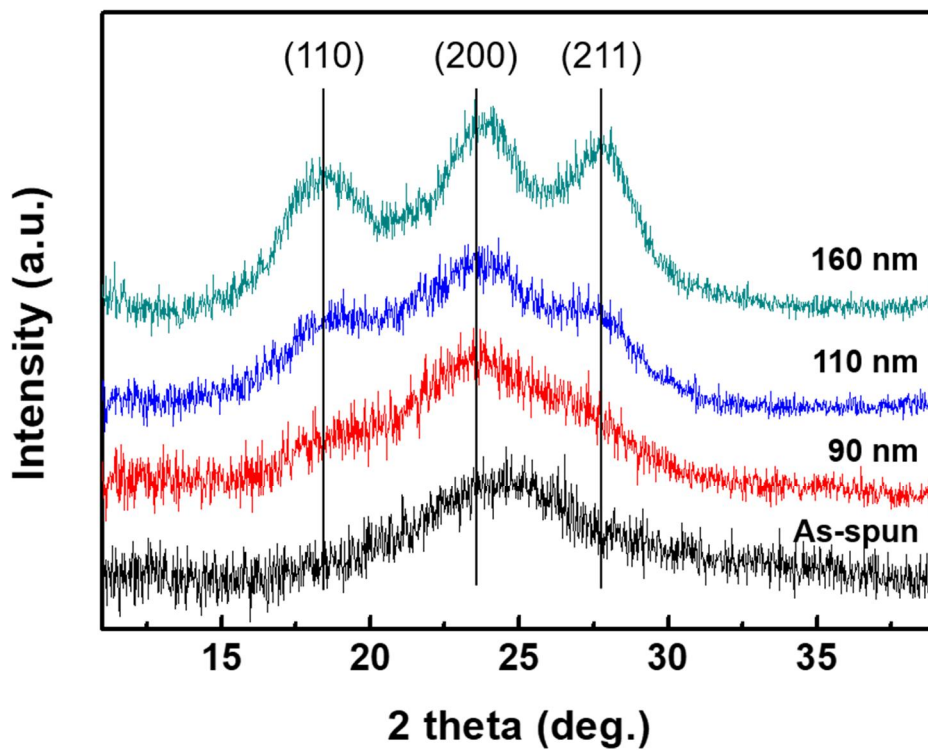


Figure V-7. XRD patterns of *m*ANFs with different diameters (90, 100 and 160 nm). *m*ANFs were treated with DMAc/aniline (2.6:1 volume ratio) at 120 °C.

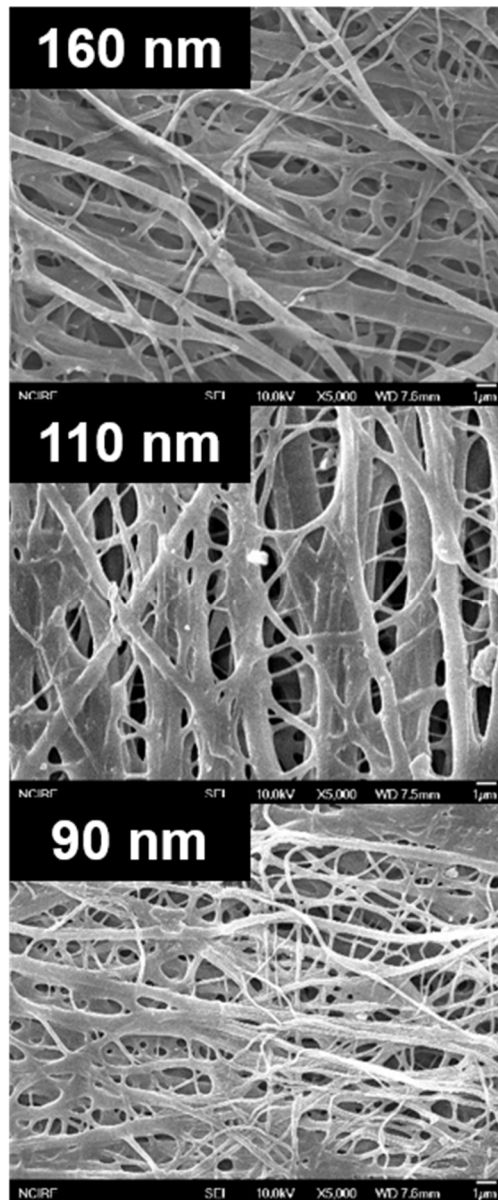


Figure V-8. FE-SEM images of *mANFs* having different diameters (90, 110 and 160 nm) after the optimized vapor-assisted crystallization process.

The thermal stability of the *m*ANFs was studied by TGA analysis and shown in Fig. V-9. The TGA curves for *m*ANFs experienced weight loss in two steps at low temperature region (40-120 °C) and high temperature region (400-600). The weight loss at low temperature region attributed to the vaporization of water molecules. Therefore, the TGA results indicated that *m*ANFs were thermally stable at above 350 °C, suggesting that they have high thermal stability. These results corresponded to the results shown in chapter IV.

The chemical stability of *m*ANFs was evaluated by observing their ability to survive in DMAc. The as-spun *m*ANF mat was directly dissolved in DMAc just after the immersion, indicating that the amorphous meta-aramid chains are easily dissolved in DMAc (figure not shown). In contrast, as shown in Fig. V-10, *m*ANFs treated under optimized condition retained their shape immediately after immersion in DMAc. This indicated that crystalline meta-aramid chains are highly resistant to DMAc, as mentioned in chapter IV. The relative weight of *m*ANF mats decreased to a certain values at 24 h of the immersion time, and then maintained their weight. The relative weight of the *m*ANF mat with 160 nm of average diameter was approximately 0.8, which is much higher value than that of *m*ANFs developed in chapter IV. The higher relative weight might be due to the higher crystallinity. In addition, the relative weights of *m*ANFs with average diameter of 110 and 90 nm were approximately 0.6 and 0.3, respectively. Although the same process was

applied to the *m*ANFs based on the same polymer, a quite differences in the crystallinity and chemical stability of the *m*ANF mats were observed. Therefore, the size-dependent behaviors of the polymer nanofibers should be thoroughly considered when design and apply the polymer nanofibers to various industrial fields.

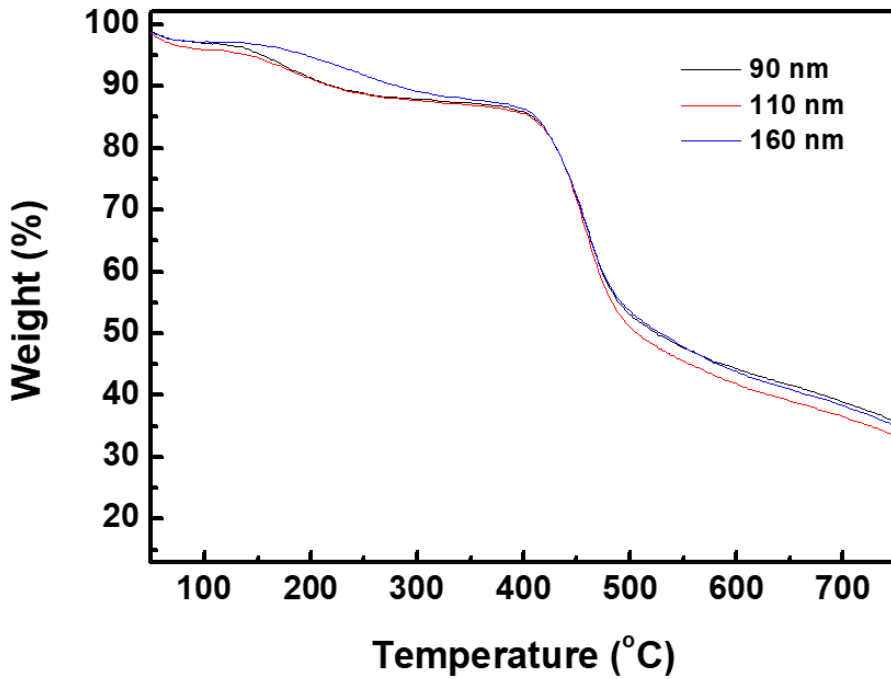


Figure V-9. TGA curves of as-spun *mANFs* with 160 nm of average diameter and *mANFs* with 90, 110 and 160 nm of average diameter treated under optimized vapor-assisted crystallization process.

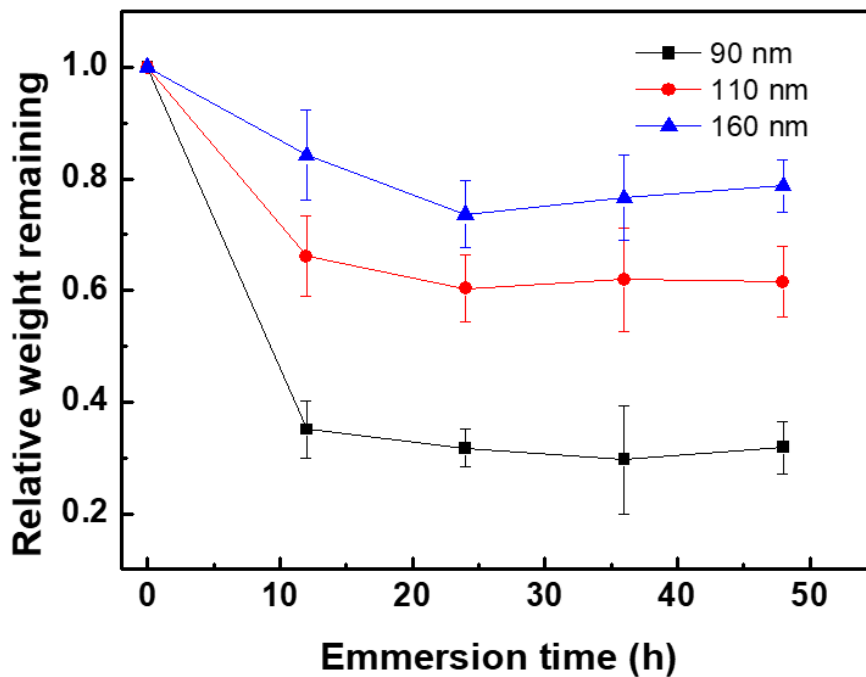


Figure V-10. Observation of the chemical stability: relative weight at a specific immersion time of *mANFs* with 90, 110 and 160 nm of average diameter treated under optimized vapor-assisted crystallization process.

V-4. Conclusion

The vapor-assisted crystallization of meta-aramid nanofibers (*m*ANFs) was developed and the effect of size on the crystallization of *m*ANFs was investigated. The *m*ANFs with 90, 110 and 160 nm of average diameter were successfully fabricated. The as-spun *m*ANFs exhibited an amorphous chain structure. The as-spun *m*ANFs having 160 nm of average diameter were subjected to vapor-assisted heat treatment under various solvent composition and the heat treatment temperature. The increase in DMAc ratio resulted in the increase of degree of crystallization of *m*ANFs. This indicated that DMAc molecules enabled the chains to crystallize by facilitating the rearrangement of chains. In addition, the degree of crystallization of *m*ANFs increased with increasing heat treatment temperature from 80 to 120 °C. However, the crystallization degree of *m*ANFs decreased with a further increase in heat treatment temperature from 120 to 180 °C. These results indicated that *m*ANFs competitively went through the crystallization of chains and formation of chain-solvent. Therefore, the optimum solvent volume composition of DMAc and aniline was determined to be 1:2.6 and the optimum temperature was selected as 120 °C. The *m*ANFs with different diameters were treated under optimized crystallization condition. It was shown that the *m*ANFs having smaller diameter exhibited lower crystallinity. The lower crystallinity of *m*ANFs with smaller diameter indicated that the

suppression of the molecular motion by the nanoscale confinement could be closely related to the crystallization process of polymer nanofibers. The results for the degree of the crystallization of *mANF* suggested that appropriate target diameter of the nanofibers should be considered when crystallization process for nanofibers is investigated.

References and Notes

1. Kim, N.; Kee, S.; Lee, S. H.; Lee, B. H.; Kahng, Y. H.; Jo, Y. R.; Kim, B. J.; Lee, K., Highly conductive PEDOT:PSS nanofibrils induced by solution-processed crystallization. *Adv Mater* **2014**, *26* (14), 2268-72, 2109.
2. Ahn, Y.; Hu, D. H.; Hong, J. H.; Lee, S. H.; Kim, H. J.; Kim, H., Effect of co-solvent on the spinnability and properties of electrospun cellulose nanofiber. *Carbohydr Polym* **2012**, *89* (2), 340-5.
3. Naga, N.; Yoshida, Y.; Noguchi, K.; Murase, S., Crystallization of Amorphous Poly(Lactic Acid) Induced by Vapor of Acetone to Form High Crystallinity and Transparency Specimen. *Open Journal of Polymer Chemistry* **2013**, *03* (02), 29-33.
4. Jeong, L.; Lee, K. Y.; Liu, J. W.; Park, W. H., Time-resolved structural investigation of regenerated silk fibroin nanofibers treated with solvent vapor. *Int J Biol Macromol* **2006**, *38* (2), 140-4.
5. Cheng, Y.-W.; Lu, H.-A.; Wang, Y.-C.; Thierry, A.; Lotz, B.; Wang, C., Syndiotactic Polystyrene Nanofibers Obtained from High-Temperature Solution Electrospinning Process. *Macromolecules* **2010**, *43* (5), 2371-2376.
6. Cheng, Y.-W.; Wang, C., Solvent-induced crystallization of electrospun syndiotactic polystyrene nanofibers and its reversible

- desorption/sorption of volatile organic vapors. *Journal of Polymer Research* **2016**, *23* (11).
7. Schulz, G. L.; Ludwigs, S., Controlled Crystallization of Conjugated Polymer Films from Solution and Solvent Vapor for Polymer Electronics. *Advanced Functional Materials* **2017**, *27* (1), 1603083.
 8. Thomann, R.; Thomann, Y.; Sernetz, F. G.; Mülhaupt, R.; Kressler, J., Vapor induced crystallization of syndiotactic random copolymers of styrene with p-n-butylstyrene. *Polymer Bulletin* **1998**, *40* (2), 313-319.
 9. Daniewska, I.; Dobkowski, Z.; Członkowska-Kohutnicka, Z., Solvent-vapor-induced crystallization of branched polydisperse polycarbonate. *Journal of Applied Polymer Science* **1986**, *31* (8), 2401-2405.
 10. Berger, L. L., Solvent-induced embrittlement in a crystallizable polyarylate. *Journal of Polymer Science Part B: Polymer Physics* **1989**, *27* (8), 1629-1647.
 11. Chiou, J. S.; Barlow, J. W.; Paul, D. R., Polymer crystallization induced by sorption of CO₂ gas. *Journal of Applied Polymer Science* **1985**, *30* (9), 3911-3924.
 12. Koziol, K. K. K.; Dolgner, K.; Tsuboi, N.; Kruse, J.; Zaporojtchenko, V.; Deki, S.; Faupel, F., Dispersion of Gold in Polycarbonate by Vapor-Induced Crystallization. *Macromolecules* **2004**, *37* (6), 2182-2185.

13. Chung, J.; Kwak, S.-Y., Solvent-assisted heat treatment for enhanced chemical stability and mechanical strength of meta-aramid nanofibers. *European Polymer Journal* **2018**, *107*, 46-53.
14. Tashiro, K.; Ueno, Y.; Yoshioka, A.; Kobayashi, M., Molecular Mechanism of Solvent-Induced Crystallization of Syndiotactic Polystyrene Glass. 1. Time-Resolved Measurements of Infrared/Raman Spectra and X-ray Diffraction. *Macromolecules* **2001**, *34* (2), 310-315.
15. Tashiro, K.; Sasaki, S.; Ueno, Y.; Yoshioka, A.; Kobayashi, M., Crystallization Behavior of Polymers as Viewed from the Molecular Level. *Korea Polymer Journal* **2000**, *8* (3), 103-115.
16. Wang, W.; Li, R.; Tian, M.; Liu, L.; Zou, H.; Zhao, X.; Zhang, L., Surface silverized meta-aramid fibers prepared by bio-inspired poly(dopamine) functionalization. *ACS Appl Mater Interfaces* **2013**, *5* (6), 2062-9.
17. Castro-Muñiz, A.; Martínez-Alonso, A.; Tascón, J. M. D., Modification of the pyrolysis/carbonization of PPTA polymer by intermediate isothermal treatments. *Carbon* **2008**, *46* (7), 985-993.

KOREAN ABSTRACT

고분자 나노소재는 일반적인 고분자 소재에서는 관찰되지 않는 특유의 물리·화학적 특성들을 보여왔다. 본 연구에서는 고분자 나노섬유의 사슬 분자운동성에 대해 연구하고, 더 나아가 분자운동성이 고분자 나노섬유의 분자 확산 특성 및 결정화 거동에 어떤 영향을 주는지에 대해 논의한다.

우선 서로 다른 직경을 갖는 나일론 6 나노섬유의 결정구조와 분자운동성에 대해 분석한다. 370 나노미터의 크기를 갖는 나노섬유의 사슬들은 상대적으로 덜 밀집된 형태인 감마상 결정구조를 보인다. 그러나 나노섬유의 직경이 120 나노미터 이하인 경우 사슬들은 매우 밀집된 구조인 알파상을 형성하고 있다. 나노섬유의 직경이 감소함에 따라 결정구조의 밀집화가 심화되면서 결정상의 녹는점이 점차 증가한다. 비정질 사슬의 분자운동을 유발하기 위해 필요한 활성화에너지는 직경이 370 나노미터에서 70 나노미터로 감소함에 따라 6.6 eV에서 12.6 eV까지 점차 증가하는 경향을 보인다. 이 결과는 직경 감소에 따라 비정질 사슬들이 밀집되어있는 구조를 형성해 움직임이 제한된다는 것을 의미한다. 비정질 사슬들이 밀집된 구조를 형성함에 따라서 rhodamine B의

방출이 억제되는 현상이 관찰된다. 이어서, cellulose acetate/sulindac 나노섬유(CNs)의 분자운동성 변화에 따른 약물방출특성의 변화를 관찰한다. 분석결과, sulindac은 따로 결정상을 형성하거나 균집체를 형성하지 않고 cellulose acetate 내에 잘 분산되어 있다. CNs는 비정질 사슬 구조를 가진다. CNs의 직경 감소에 따라 cellulose acetate 사슬의 주쇄 및 측쇄의 움직임에 필요한 활성화에너지가 증가하는 경향을 보인다. 이러한 활성화에너지의 증가는 CNs의 직경이 감소함에 따라 고분자 사슬들의 밀집도가 증가하여 분자운동성이 저하된다는 것을 의미한다. 이러한 활성화에너지의 증가에 따라, 단위면적당 약물의 방출 속도가 0.30에서 $0.08 \text{ g}\cdot\text{min}^{-0.5}/\text{m}^2$ 로 줄어든다. 그리고 CNs의 직경이 620 nm에서 350 nm로 감소에 따라 약물의 확산 계수가 85.3에서 $20.4 \text{ nm}^2/\text{min}$ 으로 크게 줄어든다. 이러한 관찰을 통해 나노섬유의 분자운동성의 저하가 약물방출 특성에 큰 영향을 준다는 것을 알 수 있다.

나노섬유의 분자운동성 변화가 사슬의 결정화 과정에 미치는 영향에 대해 고찰한다. 메타-아라미드는 매우 우수한 내화학성 및 물리적 강도를 가지고 있으나, 나노섬유로 제조시 결정구조가 파괴되어 물성 및 내화학성이 저하된다는 단점을 가지고 있다. 따라서 메타-아라미드 나노섬유(*mANFs*)를 결정화시키는 공정을

개발하고, *m*ANFs의 분자운동성 변화가 이 공정에 미치는 영향에 대해 논의한다. 공정 최적화를 위해 연구를 수행한 결과, *m*ANFs를 결정화 시키기에 최적화된 용매의 조성 부피비는 6:5:100 (DMAc:ethylene glycol:water)이며 120도의 온도에서 가장 효과적으로 결정화가 이루어진다. 최적화된 공정에서 결정화가 이루어진 샘플(*m*ANF-6-120)은 300도에서 단순 열처리를 통해 부분적으로 결정화시킨 샘플(*m*ANF-HT)에 비해 높은 결정화도를 보인다. 따라서 *m*ANF-6-120은 *m*ANF-HT에 비해 우수한 내화학을 보인다. DMAc에 48시간동안 침침을 시킨 경우 *m*ANF-6-120은 원래 질량의 28%의 질량을 유지한 반면 *m*ANF-HT는 원래 질량의 8%로 줄어든다. *m*ANF-6-120의 탄성계수는 *m*ANF-HT에 비해 약 1.7배 더 높다. 최적화된 조건에서 각기 다른 직경을 가진 *m*ANFs에 대한 결정화를 진행한 결과, 직경이 감소함에 따라 결정화도가 감소하는 현상을 보인다. 이를 통해 직경 감소에 따라 분자 운동성이 감소될 경우 결정화 현상이 억제될 수 있다는 것을 알 수 있다. 다음으로, 기체를 이용해 *m*ANFs를 결정화하는 공정을 개발하고 섬유 직경 변화에 따른 결정화도의 변화에 대해 연구한다. 용매의 조성 및 결정화 온도의 최적화를 진행한 결과, 최적의 aniline과 DMAc의 부피비는 1:2.6이었으며, 결정화는 120도에서 가장 잘 일어난다.

앞선 용매 기반 결정화공정과 마찬가지로, 나노섬유의 직경이 작을수록 *m*ANFs에 대한 기체를 이용한 결정화 공정의 효과는 급격히 감소한다. 이로 인해, 평균직경이 160, 110, 90 nm인 *m*ANFs를 최적의 조건에서 결정화시킨 후 DMAc의 48시간동안 함침시키면 기존 대비 각각 79, 62, 32%의 질량을 가지게 된다. 이러한 연구결과들을 통해 나노섬유의 분자운동성에 따라 다양한 특성들이 변화될 수 있으며, 나노섬유를 첨단 산업에 적용하기 위해서는 이러한 특성 변화에 대한 규명 및 고찰이 필수적으로 선행되어야 한다는 것을 알 수 있다.

주요어: 결정화, 결정구조, 나노섬유, 나일론 6, 메타-아라미드, 분자운동성, 분자 확산, 사슬 밀집, 셀룰로오스 아세테이트, 약물 방출, 크기 효과

학번: 2012-30219

LIST OF PAPERS, PATENTS AND SYMPOSIUMS

PAPERS

1. **J. Chung**, J. W. Chung, S.-Y. Kwak, "Adsorption-Assisted Photocatalytic Activity of Nitrogen and Sulfur Codoped TiO₂ under Visible Light Irradiation", *Phys. Chem. Chem. Phys.* **2015**, 17, 17279.
2. **J. Chung**, J. W. Chung, S.-Y. Kwak, "Confinement-Induced Change in Chain Topology of Ultrathin Polymer Fibers", *Macromolecules* **2018**, 51, 4229.
3. **J. Chung**, S.-Y. Kwak, "Solvent-Assisted Heat Treatment for Enhanced Chemical Stability and Mechanical Strength of Meta-Aramid Nanofibers", *Eur. Polym. J.* **2018**, 107, 46.
4. **J. Chung**, S.-Y. Kwak, "Effect of Nanoscale Confinement on Molecular Mobility and Drug Release Properties of Cellulose Acetate/Sulindac Nanofibers", *J. Appl. Polym. Sci.* **2019**, 136, 47863.

PATENTS

1. 곽승엽, 박현배, 류수열, 정준호, “나노섬유웹 기반 화학작용제 방호복 소재 및 그 제조방법과 이를 구비하는 보호장구”, 대한민국 특허출원 10-2017-0053520 (2017. 4. 26)
2. 곽승엽, 박현배, 류수열, 정준호, “내화학성과 기계적 물성이 증대된 정렬형 메타-아라미드 나노섬유 및 그 제조방법”, 대한민국 특허등록 10-1893291 (2018. 8. 23)

SYMPOSIUMS

1. 추계 한국재료학회 (2013), “Effect of the thermal treatment on the photocatalytic activity of the N, S codoped TiO₂”
2. Hong Kong International Conference on Engineering and Applied Science (2013), “Synthesis of visible light active nitrogen and sulfur codoped TiO₂ by solvothermal treatment”
3. MRS Fall Meeting & Exhibit (2014), “Synthesis of N,S codoped TiO₂ with high adsorptivity and visible light photocatalytic activity”

4. **추계 고분자학회** (2015), “Investigation of size effect on molecular mobility of PS nanofibers by ^1H solid-state NMR analysis”
5. **Materials Fair** (2015), “Identification of size effect on molecular mobility of polystyrene nanofibers by ^1H solid-state NMR analysis”
6. **MRS Fall Meeting & Exhibit** (2016), “Investigation of size-dependent behaviors of Nylon 6 nanofibers”
7. **2nd International Conference on Nanotechnology and Environmental Issues** (2017), “Polyamid nanofiber composites for organic pollutant removal and chemical warfare protection”
8. **추계 고분자학회** (2017), “Size effect of Nylon 6 nanofibers on the crystal structure”

감사의 글

많은 분들께서 주신 가르침과 도움 덕분에 박사학위과정을 무사히 마치게 되었습니다. 이 면을 빌어 감사하는 마음을 전합니다.

먼저 부족한 저를 늘 걱정해주시고 성장할 수 있도록 많은 가르침 주신 곽승엽 교수님께 깊은 감사를 드립니다. 그리고 귀중한 시간 내어 학위논문을 심사해주신 안철희 교수님, 유웅열 교수님, 김형섭 교수님, 김주용 교수님께 감사 드립니다. 연구주제에 대해 많은 조언을 해주신 정재우 교수님께도 감사의 말씀 드립니다.

성격도 급하고 실수도 많이 하던 저를 늘 이해해주시고 아껴주신 연구실 선배님들께 깊은 감사 드립니다. 연구에 대한 도움과 더불어 연구실 생활적인 면에서도 많은 가르침을 받았습니다. 또한 부족한 저를 믿고 따라와준 연구실 후배 분들에게도 감사 드립니다. 열심히 연구에 매진하는 후배들을 보며 저도 함께 힘을 낼 수 있었습니다.

늘 한결같이 저를 믿어주시고 응원해주신 우리 가족 여러분들께 깊은 감사를 드립니다. 부모님 가르침대로 올바르게 겸손한 사회인으로 거듭날 수 있도록 노력하겠습니다. 힘들 때마다 버팀목이 되어주고, 좋은 일이 생기면 함께 기뻐해주며 저에게 큰 힘이 되어준 서화에게도 감사의 말씀 드립니다.

지금까지 제가 많은 분들께 도움과 가르침을 받았듯이, 앞으로는 공학도로서 저도 세상에 보탬이 될 수 있도록 노력하겠습니다. 감사합니다.

2019년 8월 정준호 올림